MELT INFILTRATION SQUEEZE CASTING OF SIC REINFORCED FUNCTIONALLY GRADED METAL MATRIX COMPOSITE PROCESSING AND CHARACTERIZATION

A THESIS SUBMITTED TO
THE GRADUATE SCHOOL OF NATURAL AND APPLIED SCIENCES
OF
MIDDLE EAST TECHNICAL UNIVERSITY

BY

ERALP TATLIŞEN

IN PARTIAL FULFILLMENT OF THE REQUIREMENTS
FOR
THE DEGREE OF MASTER OF SCIENCE
IN
METALLURGICAL AND MATERIALS ENGINEERING

JANUARY 2024

Approval of the thesis:

MELT INFILTRATION SQUEEZE CASTING OF SIC REINFORCED FUNCTIONALLY GRADED METAL MATRIX COMPOSITE PROCESSING AND CHARACTERIZATION

submitted by **ERALP TATLIŞEN** in partial fulfillment of the requirements for the degree of **Master of Science** in **Metallurgical and Materials Engineering, Middle East Technical University** by,

Prof. Dr. Halil Kalıpçılar
Dean, **Graduate School of Natural and Applied Sciences**

Prof. Dr. Ali Kalkanlı
Head of the Department, **Metallurgical & Materials Engineering**

Prof. Dr. Ali Kalkanlı
Supervisor, **Metallurgical & Materials Engineering**

Examining Committee Members:

Prof. Dr. Abdullah Öztürk
Metallurgical and Materials Engineering, METU

Prof. Dr. Ali Kalkanlı
Metallurgical and Materials Engineering, METU

Prof. Dr. Kadir Kocatepe
Metallurgical and Materials Engineering, Gazi Uni.

Assist. Prof. Dr. Yusuf Keleştemur
Metallurgical and Materials Engineering, METU

Assist. Prof. Dr. Çiğdem Toparlı
Metallurgical and Materials Engineering, METU

Date: 26.01.2024

I hereby declare that all information in this document has been obtained and presented in accordance with academic rules and ethical conduct. I also declare that, as required by these rules and conduct, I have fully cited and referenced all material and results that are not original to this work.

Name Last name : Eralp Tatlışen

Signature :

ABSTRACT

MELT INFILTRATION SQUEEZE CASTING OF SIC REINFORCED FUNCTIONALLY GRADED METAL MATRIX COMPOSITE PROCESSING AND CHARACTERIZATION

Tatlışen, Eralp
Master of Science, Metallurgical and Materials Engineering
Supervisor: Prof. Dr. Ali Kalkanlı

January 2024, 98 pages

Today, silicon carbide(SiC) ceramics reinforced with aluminum(Al) are used in variety of applications such as ballistics, structural applications, automotive industry and electrical systems. The aim of this study is to produce ceramic-metal composites with squeeze cast infiltration to investigate the difference in mechanical behaviors such as wear resistance, hardness and its relation with the processing of the composite and the SiC content of the composite.

The hot preform squeeze casting is applied to the compacts which are made of 50 g powder containing 20 g SiC powder and 30 g Al powder, and the compact which contains 50 g SiC powder. Cold preform squeeze casting applied to the compact which contains 20 g SiC powder and 30 g Al powder.

In the hot preform squeeze casting process, the ceramic preform was heated to 1000 °C and placed into the mold cavity, then the 2 wt% Mg was added in liquid Al6061 then alloy was poured on top of hot preform in the mold and then pressurized with 100 MPa to complete hot preform squeeze casting.

Also, hot preform squeeze casting was performed with the ceramic-metal preform, and it was heated to 800 °C, then the infiltration occurred with 100 MPa to complete hot preform squeeze casting. In the cold preform squeeze casting process, the ceramic-metal preform was used and the infiltration was realized without the heating of the preform, then it was vacuum sintered around 600 °C for 1.5 h to obtain final consolidation similar to strain-induced melt activation and solid phase sintering.

Squeeze-cast infiltrated specimens were characterized by XRD, SEM, EDS, image analysis, particle size analysis, wear test, and hardness tests. In terms of the mechanical characterization, experimental results revealed that the highest performance was obtained by the hot preform squeeze casting technique with %100 SiC porous compact. The average hardness value of the specimen was measured as 224 HBW (2.5/62.5). In addition, wear test results indicate that the specific wear rate of this specimen revealed the lowest specific wear rates which are 0.008, 0.007, and 0.006 mm^3/Nm under the 10, 15, and 20 N applied loads.

Keywords: Squeeze casting, Hot preform, Cold preform, Infiltration, Metal matrix composite

ÖZ

SIC TAKVİYELİ FONKSİYONEL KADEMELİ METAL MATRİS KOMPOZİTİN ERİYİK SIZMA SIKIŞTIRMA DÖKÜMÜ İLE PROSES VE KARAKTERİZASYONU

Tatlışen, Eralp
Yüksek Lisans, Metalurji ve Malzeme Mühendisliği
Tez Yöneticisi: Prof. Dr. Abdullah Öztürk

Ocak 2024, 98 Sayfa

Metal-Seramik kompozitler farklı endüstrilerde yaygın olarak kullanılmaktadır. Günümüzde alüminyum ile güçlendirilmiş silisyum karbür seramikler balistik, yapısal uygulamalar, otomotiv endüstrisi ve elektrik sistemleri gibi çeşitli uygulamalarda kullanılmaktadır. Bu çalışmanın amacı, eriyik sızma sıkıştırma dökümü ile seramik-metal kompozitler üreterek aşınma direnci, sertlik gibi mekanik davranışlardaki farklılığı proses ve kompozitin silisyum karbür içeriği ile ilişkilendirmektir.

50 g SiC tozdan yapılan ve 20 g SiC tozu + 30 g Al tozu içeren kompaktlara sıcak preform sıkıştırma döküm uygulandı. 20 g SiC tozu ve 30 g Al tozu içeren diğer kompakta ise soğuk preform sıkıştırma döküm uygulandı. Otomatik Hidrolik Pres kullanılarak infiltrasyon ve ön ısıtma öncesi yapılar elde edildi.

Sıcak preform sıkıştırma döküm prosesinde, seramik preform 1000 °C'ye ısıtılarak kalıp boşluğuna yerleştirildi, daha sonra %2 Mg katkılı sıvı Al6061 alaşımı kalıptaki sıcak preformun üzerine dökülerek 100 Mpa ile basınçlandırıldı. Sıcak preform sıkıştırmalı dökümü tamamlandı.

Ayrıca seramik-metal preform üzerine sıcak preform sıkıştırma dökümü gerçekleştirildi ve 800 °C'ye ısıtıldı, daha sonra sıcak preform sıkıştırma dökümünü tamamlamak için 100 Mpa ile infiltrasyon gerçekleştirildi. Soğuk ön kalıp sıkıştırma döküm prosesinde, seramik-metal ön kalıp kullanılıp ve ön kalıp ısıtılmadan infiltrasyon gerçekleştirildi, daha sonra gerinim tetiklemeli ergiyik aktivasyonuna ve katı faza benzer nihai konsolidasyonu elde etmek için numune yaklaşık 600 °C'de bir buçuk saat boyunca vakumla sinterlenmiştir.

Numuneler XRD, SEM, EDS, görüntü analizi, parçacık boyutu analizi, aşınma testi ve sertlik yöntemleri ile karakterize edilmiştir. Mekanik karakterizasyon açısından, %100 SiC tozu içeren kompakt ile yapılan, sıcak preform sıkıştırma döküm tekniğiyle üretilen numune ile en yüksek performans elde edilmiştir. Numunenin ortalama sertlik değeri 224 HBW (2,5/62,5) olarak ölçülmüştür. Ayrıca aşınma testi sonuçları, bu numunenin spesifik aşınma oranının, uygulanan 10, 15 ve 20 N yükler altında 0,008, 0,007 ve 0,006 mm^3/Nm ile en düşük spesifik aşınma oranını verdiğini göstermektedir.

Anahtar Kelimeler: Sıkıştırılmış döküm, sıcak ön kalıp, soğuk ön kalıp,
infiltrasyon, metal matrisli kompozit

To my family and friends

ACKNOWLEDGEMENTS

The author wishes to express his deepest gratitude to his supervisor Prof. Dr. Ali Kalkanlı for his guidance, advice, criticism, encouragement, and insight throughout the research.

Thanks should also go to ASELSAN, who allowed me to complete my unfinished research.

Thanks should go to NUROL TECHNOLOGY, who provided allowance to use their technical devices for my research.

Thanks should go to Olgun Tanberk who is the manager of the SİNTERMETAL INDUSTRY company for the contribution by doing vacuum sintering work.

Thanks should go to the Doc. Dr. Safa Polat and Dr. Ogr. Uyesi. Alper Incesu for testing the samples with a tribometer to characterize the friction coefficient and volume loss of the samples under certain loads.

I also could not have undertaken this journey without the support of my office mates from ASELSAN, their editing help, and moral support.

Lastly, and most importantly, I would like to thank my family. Also, I would like to thank my closest friends who are Ahmet Serdar Göbel, Berkay Özgür, Zeynep Uluca, Selin Güntop and Coşku Vardallı. Their belief in me kept my spirits and motivation high during this period and I always felt their support by my side.

TABLE OF CONTENTS

LIST OF TABLES

TABLES

LIST OF FIGURES

FIGURES

CHAPTER 1

INTRODUCTION

Nowadays, significant improvements have been made in the light metal matrix composites development, particularly using lightweight aluminum (Al) alloys as the matrix material. These advancements lead to significant applications, primarily within the automotive industry [1].

Metal-ceramic composites containing a high volume of reinforcement have extensive use in tribology and high-temperature resistant components such as pistons, engine blocks, brake pads, and heat shields. Most of these components can be made by the infiltration process of liquid metal to the porous ceramic preforms. Ceramic particle/fiber-reinforced metals are attractive due to their improved elastic modulus, high strength, and low thermal expansion characteristics [2].

Also, ballistic armor was used in the defensive industry for many years. It is used in aircraft, warships, vehicles, and personal armor. The light armor materials systems development by using metal-ceramic composite structures, which makes better penetration resistance, impact energy dissipation, and damage containment, is crucial in the development of shielding armor against projectile threats in structures [3].

Compared to steel or metal armor, ceramic armor which can be composed of carbides, nitrides, and borides, leads to weight savings of about 65% over conventional rolled homogenous armor [4]. However, the fracture properties of the ceramics are poor due to their ionic and covalent bonding nature which prevents the activation of the deformation mechanisms and absorption of the fracture energy. This restricts the armor applications for multi-hit capacity [5]. If the ceramic is reinforced with a metal matrix, the fracture properties will be sufficiently enhanced by ductile and tough matrix [6].

Although the maximum single hit capacity of the armor decreased, the structure would have excellent ballistic protection if the structure was appropriately designed. Making ceramic-metal composite may provide better ballistic efficiency, so producing porous ceramic compact and applying melt infiltration process with ductile metal could be beneficial for multi-hit impacts [7].

Numerous fabrication techniques have been investigated for Al-based metal matrix composites (MMCs). These techniques are vapor state methods, liquid phase methods like preform infiltration, melt stirring, squeeze casting, and solid-state methods such as powder forming and diffusion bonding. Among these, squeeze infiltration is one of the most cost-effective and efficient methods for producing metal matrix composites with a high volume of reinforcement. Squeeze infiltration has several advantages over traditional MMC fabrication methods. For example, these composites exhibit very little shrinkage and gas porosity due to solidification occurring under pressure, resulting in enhanced properties [8].

The purpose of this research is to produce SiC-based Al-reinforced composite with melt infiltration and sintering methods to enhance the mechanical features of Al such as wear resistance and areal hardness. The main motivation is to provide a prototype composite material combining the wear-resistant properties of ceramic reinforcement and the shock-absorbing ability of the Al alloy matrix. In other words, high wear resistance provided by SiC, and high fracture properties provided by Al. In this study, the wear resistance and hardness of the specimens were compared and the effects of the two production techniques and the SiC content of the compacts were investigated. The specimens were characterized by phase analysis, particle size and distribution analysis, X-ray diffraction (XRD) analysis, light microscope, scanning electron microscope (SEM), energy dispersive spectroscopy (EDS), hardness and wear tests.

CHAPTER 2

LITERATURE REVIEW

2.1 Metal Matrix Composites

Composite materials contain two or more separate substances with clearly different chemical, physical, and mechanical characteristics. Composite materials generally perform better when compared to the properties of a single component. There are different categories for composite materials. The most common classification is related to the fundament of the matrix, where there are three types of composites: (a) metal matrix composites (MMCs), (b) polymer matrix composites (PMCs), and (c) ceramic matrix composites [9].

For many specialized applications in the aerospace, sports, marine, and automotive industries, MMCs are encouraging materials. MMCs can expose exceptional mechanical and tribological characteristics. It is required for MMCs to withstand substantial loads without undergoing distortion, deformation, or fracture during operation. Furthermore, they should maintain this tribological performance over extended periods, preventing severe surface damage. The global demand and interest in MMCs have increased due to their outstanding mechanical and tribological properties.

Three major factors determine the performance of MMCs: (1) the composition and microstructure of MMCs; (2) the size, volume fraction, and distribution of reinforcements within metal matrices; and (3) the features of the interface between the metal matrices and the reinforcements. Tribological features of composite materials such as friction and wear can be impacted by some imperfections. Voids and pores formed throughout the production of MMCs can be given as examples of these imperfections. Studies have demonstrated that an increase in porosity content within composite material deteriorates the mechanical and tribological features of MMCs. The wear and friction properties of MMCs are also affected by tribological test parameters such as sliding speed, applied load, sliding time, and surface roughness [10].

The amount, size, shape, and distribution of fibers or hard/soft particles embedded into the matrix influence the wear and friction performance of the composites. Moreover, the interfacial bonding between the reinforcement and matrix is a critical factor affecting the tribological and mechanical features of metal matrix composites (MMCs). Generally, incorporating hard particles as reinforcement materials in the matrix enhances the strength and wear resistance of MMCs. Nevertheless, it tends to reduce the ductile property of composites. Conversely, soft particles are often used as solid lubricants which lowers the friction coefficient of MMCs. The solid and reinforcement lubricants may have adverse impacts on the composites, leading to unpredicted features for the MMCs [11].

The typical type, aspect ratio, diameter, and examples of the reinforcements for the metal matrix composites are shown in Table 1.

Table 1. Typical Reinforcements in metal matrix composites [12].

Type	**Aspect Ratio**	**Diameter, µm**	**Examples**
Particle	1-4	0.05-25	SiC, Al_2O_3, BN, TiC, B_4C, WC
Discontinuous fiber: Whisker, Short fiber	10-10000	0.05-5	Al_2O_3, SiC, TiB_2, Vapor grown carbon fibers, Al_2O_3+SiO_2, Carbon nanotubes
Continuous fiber	>1000	3-150	SiC, Al_2O_3, C, B, W, Nb-Ti, Nb_3Sn, TiC, B_4C, WC

2.2 SiC-Al Composites

Table 2. Some examples of application of Al metal matrix composites [12].

MMC Type	**Reinforcement**	**Application**	**Potential Benefits**	**Processing Method**
Al MMCs	SiC particles and fibers	Piston	High specific stiffness	Powder metallurgy
		Connecting rod	Good fatigue properties	Vacuum hot pressing
		Brake drum and rotor	Relatively low cost	Hot isostatic pressing
		Bicycle frame	High thermal conductivity	Casting (stir, squeeze, and composting)
		Space applications (Joint and attachment fittings)	Tailorable CTE	
		Electronic packaging, Thermal management	Low density	
			Conventional processing	

When it comes to metal matrix composites (MMCs), Al is the most used matrix material. Low density, high strength, strong mechanical properties, low electrical resistance, high corrosion resistance, and high machinability are the main reasons for the frequent use of Al [13].

Conversely, the wear resistance of the Al alloys is relatively poor, and it has restricted their usage in some tribological applications. In recent years, lots of research has been done on the Al MMCs and the tribological characteristics of fiber and particle-reinforced Al alloy composites have significantly improved recently in terms of sliding wear, abrasive wear, friction, and seizure resistance [14].

For the Al MMCs, some examples of reinforcement materials, applications, potential benefits, and processing methods are shown in Table 2. As can be seen, there are multiple production methods and lots of application areas. By using the Al MMCs, there are lots of possible gains for the physical and mechanical properties rather than using the monolithic constituent in the composite [13].

Particulate-reinforced composites are more economical compared to fiber-reinforced composites due to the low-priced particles and production processes. Since they are mostly isotropic, they may be easily produced through the usual methods practiced for metals.

As a result, SiC-reinforced composites progressively became an alternative material for various components in the automotive industry, including cylinder heads, liners, pistons, brake rotors, and calipers [15].

Ceramics are outstanding materials for ballistic armor applications due to their favorable mechanical properties and low density. This provides a superior mechanical strength/density ratio when compared to other materials used for similar purposes. Silicon carbide (SiC), a well-known non-oxide ceramic, is extensively used as an abrasive due to its remarkable hardness. Its hardness is only lower than the diamond, cubic boron nitride (BN), and boron carbide(B_4C). SiC is a promising ceramic material with superb thermomechanical characteristics such as high thermal conductivity, exceptional mechanical properties, and high resistance to wear and oxidation [16].

Table 3. Properties of abrasive ceramics [17].

Ceramic	**Density (g/cm³)**	**Elastic Modulus/ GPa**	**Flexural Strength/ Mpa**	**Vickers Hardness/ GPa**	**Fracture Toughness/ MPa√m**	**Price/ (RMB/kg)**
Al_2O_3	3,80	340	400	14-18	2.8-4.5	80 - 100
B_4C	2,50	400-450	400-500	28-32	2.5-3.0	600 - 1200
SiC	3,20	350-470	350-700	22-26	2.8-4.3	200 - 400

In Table 3, the physical and mechanical properties of the SiC-Al_2O_3-B_4C ceramics are mentioned. Among those ceramics, alumina (Al_2O_3) seems to be the cheapest advanced ceramic, but its density is higher than the other ones and the hardness values are relatively lower than the B_4C and SiC. Also, B_4C has the lowest density and the highest hardness values, but it is much more expensive than Al_2O_3 and SiC. When the properties of the silicon carbide are examined, the density, the hardness, and the price values are in between the other ones.

From the emergence of metal matrix composites (MMC) to now, SiC is one of the most attractive options for particle-reinforced metals and fiber-reinforced metals due to its high hardness and low price [18].

Abrasion is the removal of material from a relatively soft surface by the ploughing or cutting action of hard grit particles. The abrasion resistance of Al alloys can be increased by reinforcing them with short fibers, whiskers and hard ceramic particles.

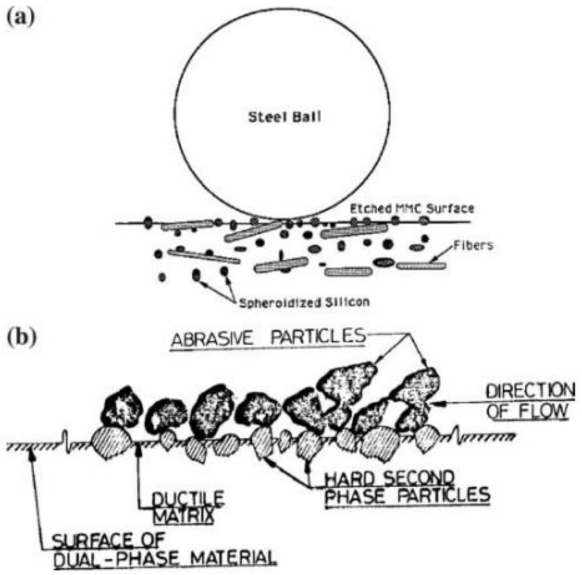

Figure 1. Diagram of (a) a steel ball sliding on an etched surface of an Al–Si alloy fiber composite. In this situation, protrusion of silicon particles and ceramic fibers preserving the contact between steel and Al in the composite, and (b) hard second-phase particles preserving the ductile matrix from grinding [19].

Firstly, the ductile Al matrix composite is generally worn away by the cutting or ploughing of the abrasive, and then, bulges of the hard second-phase particles or short fiber reinforcements appear. When the certain critical volume fraction of the second phase and the interparticle spacing of the abrasive particles are reached, the hard-phase protrusions will completely protect the matrix from further abrasion, as shown schematically in Figure 1 [19].

Generally, the hard phase is brittle and will be eroded after certain continuing events of abrasive forces. When the softer Al matrix emerges, the compact starts to wear. However, the importance of the Al matrix should not be underestimated. It supports hard-phase reinforcement materials and gives ductility to the metal matrix composite. If the metal matrix is not strong enough to support the reinforcement materials, the hard phase materials are prone to fragmentation or pull-out of the surface [19].

For the brake rotors, Weiss confirms that using the Al composites could lead to 60%. weight reduction when compared to cast iron. When the reinforcement content of the composite increases, Al matrix composites exhibit a lower wear rate under sliding and abrasion wear. Based on the amount of particle content, abrasive wear rates are decreased by 55–90% when checked against the wear rate of unreinforced Al. While the wear rate decreased with the increase of low-volume SiC particles in Al-Si alloys (up to 8%), the wear resistance increased with increasing reinforcement percentage. At approximately 20 vol%. SiC in the Al matrix, composite brake rotors have a lower wear rate than cast iron [20].

2.3 Melt Infiltration

There are different methods to produce the Al/SiC composites such as stir casting, powder metallurgy, and melt infiltration which includes the penetration of Al melt into the pores of SiC compacts to make MMCs by using the liquid state routes [21].

Melt infiltration is regarded as an important approach for manufacturing different composites by utilizing ceramic preforms. In this method, a molten alloy is injected into a porous ceramic preform. Compared to the other techniques, this process offers several benefits. Firstly, the volume fraction of the reinforcement is controllable. Also, the dispersion of reinforcement is quite uniform. In addition, the residual porosities can be eliminated if the wetting problem is overcome and the absence of interfacial reactions between the reinforcement and matrix can be guaranteed in the final product. Moreover, the composite's resulting properties can be adjusted to fulfill specified qualifications through the incorporation of suitable alloying elements.

For the infiltration methods, the most important point to overcome is the wetting behavior of the system. The affinity of the reinforcement and the matrix material is the decisive factor in terms of wettability. Most of the time, this affinity is poor, and it becomes much weaker by the appearance of the oxide skins on the metal surfaces.

In short, the main problem for achieving melt infiltration is the wetting of the ceramics by liquid metal [22].

Wettability is defined as the ability of a liquid to spread on a solid surface which indicates the degree of proximity between a liquid and a solid. The reduction in the free energy of the system is the driving force for wetting. To complete the infiltration process, it is essential to succeed in wetting the ceramic phase by the metal matrix since there can be no interfacial reaction if the wetting is not achieved. By providing suitable temperature and atmospheric conditions, wettability between the ceramic and metal phases is established, allowing the liquid metal to be injected into the porous ceramic preform through capillarity based on thermodynamic criteria [7].

For the SiC-Al MMCs, the main hindrance is the non-wetting nature of the SiC substrate by the Al melt which leads to weak ceramic–metal interfaces and incomplete infiltration.

To improve the infiltration process, an external pressure or vacuum must be applied to surpass the threshold pressure(P_0) which is the pressure needed to get over the capillary back pressure [21].

2.4 Pressureless Infiltration

Pressureless infiltration is a process where the pores of the preform are filled by liquid metal without applying any external pressure. However, several problems impede the recognition of this method as a viable composite manufacturing technique.

The major problem is the limited wetting of the SiC substrate by molten Al which is coming from the formation of an oxide layer on the surface of the Al melt.

Another difficulty involves unwanted reactions at the Al/SiC interface, which change the chemical composition of the molten Al and give rise to the formation of undesired phases at the interface, such as Al_4C_3 and Al_3SiC_4 [21].

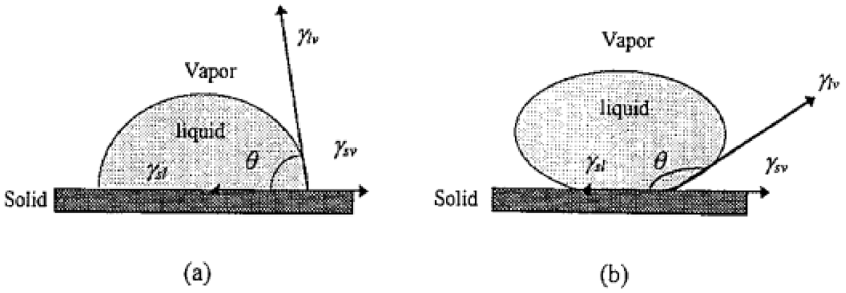

(a) (b)

Figure 2. Schematic diagram showing a sessile drop during (a) wetting and (b) nonwetting [23].

The experimental evaluation of wetting is usually conducted by using the configuration of a steady-state drop of liquid on a flat solid surface, commonly known as a sessile drop. In cases where the liquid drop is sufficiently small and the gravitational force is negligible in comparison to its surface tension, the drop will endeavor to follow a spherical shape, as it represents the configuration with the smallest surface area and, consequently, the lowest surface free energy. Schematic cross-sections of a sessile drop are illustrated in Figure 2. The contact angle which is indicated as Θ, developed between the interface and a tangent to the drop's surface at the point where it intersects with the substrate's surface. The symbols γ_{lv}, γ_{sv}, and γ_{sl} correspond to the surface tension of the liquid–vapor, solid–vapor, and solid–liquid interfaces, respectively. If the interaction lowers the free energy of the solid when it is in contact with the liquid, then the solid is prone to be covered by the liquid, exhibiting wetting behavior. Conversely, if the surface tension of the solid increases when it is in contact with the liquid, the solid is prone to minimize the area covered by the liquid and thus does not exhibit wetting by the liquid.

The shape of the sessile drop is related to the characteristics of the solid substrate. When the existence of the liquid phase results in a reduction of γ_{sv}, a driving force that is equivalent to γ_{sv}-γ_{sl} will be formed on the borders of the drop, causing an extension of the liquid–substrate interface. This scenario is illustrated in Figure 2a and occurs when $\gamma_{sv} > \gamma_{lv}$, and $\gamma_{sv} > \gamma_{sl} > \gamma_{lv}$, with a contact angle Θ which is measured lower than 90°. A decrease in the contact angle leads to an expansion of the drop's surface area, resulting in a decrease in the liquid's surface free energy associated with a decrease in the solid's surface free energy.

The chemical reactions that are thermally activated at the solid-liquid interface can improve the wetting in the infiltration, but meanwhile, there should be minimum generation of the unwanted reaction products. An example of a helpful interface reaction is the dissolution of a component of the liquid into the substrate. In such reactions, the free energy of the reaction at the border of the liquid drop increases the driving force for wetting. As the drop enlarges, the advancing liquid retains the contact with unreacted solid, allowing the free energy of the reaction to proceed contributing to the driving force for wetting. Eventually, numerous researches have focused on designing alloys that are suitable for metal matrix composites to incorporate elements capable of dissolving into the reinforcing ceramic at the process temperature.

Alloying elements also perform other functions. For example, magnesium (Mg), which is one of the most commonly used alloying elements in Al- SiC metal matrix composite alloys, acts as a powerful surfactant that scavenges oxygen. Mg forms $MgAl_2O_4$ spinel at the Al–SiC interface. In addition to increasing the driving force for wetting, this reaction consumes the oxygen that exists on the surface of the reinforcement, thins the oxide layer, and thus further enhances wetting. Another commonly used alloying element in Al–SiC metal matrix composite alloys is silicon. It has been shown that an excess of silicon in the Al alloy is favorable in retarding the dissolution of SiC by Al, according to the reaction.

In addition, alloying elements are also used for other purposes. For instance, Mg, which is a frequently used alloying element in Al-SiC MMC alloys, performs as an effective surfactant that removes oxygen. The added Mg reacts and forms the compound $MgAl_2O_4$ spinel at the Al–SiC interface which increases the driving force for the wetting. Also, this reaction uses the surface oxygen from the reinforcement, reduces the oxide layer, and further improves wetting.

Another frequently used alloying element in these alloys is Si. Research indicates that an abundance of silicon in the Al alloy helps to slow down the dissolution of SiC by Al, as described by the reaction.

$4Al + 3SiC = Al_3C_3 + 3Si$

Therefore, silicon's major contribution is not to wetting, but rather to preventing the formation of Al_4C_3 [23].

Incorporating Si into the Al alloy is essential for enabling Al to infiltrate SiC. Si acts as a surfactant within the Al alloy. The addition of ten percent Si to the Al alloy can reduce the surface tension of the molten Al's from 0.76 N/m to 0.66 N/m. Additionally, Mg acts as a catalyst in the infiltration process, playing a crucial role alongside Si in facilitating the infiltration of molten Al into SiC [24].

Pech-Canul et al. consider that optimum conditions are necessary to be provided to get a complete infiltration without relying on external pressure. They suggest the following optimum conditions which are:

- incorporating more than 3% Mg into the Al melt.
- utilizing SiC particles coated with a thin silicon layer.
- maintaining an internal furnace pressure of 1.2 atm.
- adjusting the furnace atmosphere to 100% nitrogen.

Table 4. Chemical composition of Al6061 alloy.

Element	**Si**	**Mg**	**Cu**	**Cr**	**Fe**
Wt%	0,4-0,8	0,8-1,2	0,15-0,40	0,04-0,35	0,70Max
Element	**Ti**	**Zn**	**Mn**	**Al**	**Others**
Wt%	0,15Max	0,25Max	0,15	Rest	0,15Max

Al 6061 is highly used in numerous engineering applications including transport and construction where superior mechanical properties such as tensile strength and hardness. Its superior corrosion resistance due to the content of alloying elements makes an appropriate candidate material to resist marine conditions. A typical chemical composition of Al 6061 is presented in Table 4 [25]**.** The demand for lighter weight, cost effective and high-performance materials for use in a spectrum of structural and non-structural applications has resulted in the need for fabrication of metal matrix composites (MMCs) of various types [26]. Considering the benefits of the Si and Mg to the wetting of Al on SiC, and since the Al6061 alloy involves good amount of Mg and Si alloying elements, it is suitable for the infiltration applications.

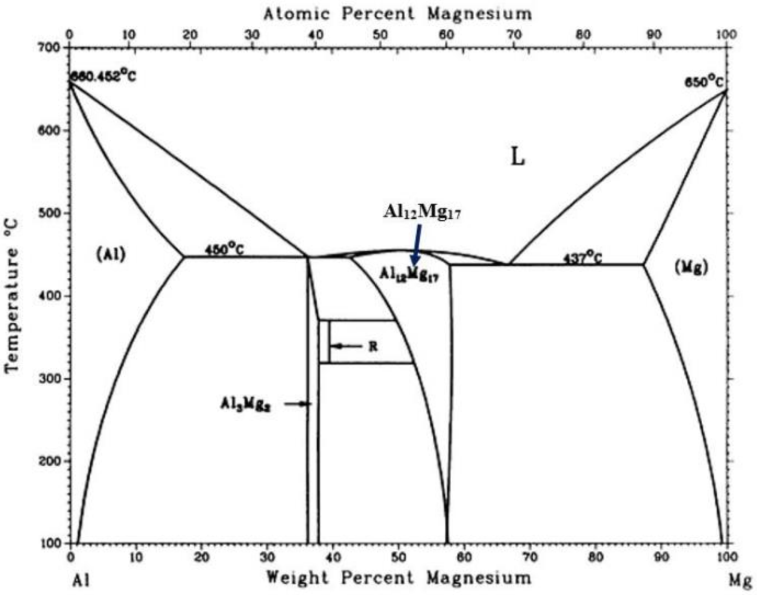

Figure 3. Al-Mg phase diagram.

Also, addition of the extra Mg alloying element will lead to the lower liquidus temperature as it can be seen in Figure 3. This means that the temperature at which the alloy transitions from liquid to solid phase is decreased with the addition of magnesium and the alloy solidifies more quickly once it reaches this lower temperature. This results in rapid solidification which can promote the formation of finer grains by reducing the time available for grain growth. The presence of magnesium enhances this effect by promoting the formation of numerous nucleation sites, resulting in a finer and more uniform grain structure.

Infiltration of a porous body by a liquid is most effectively modeled by representing the porous body as numerous cylindrical capillaries, through which the liquid ascends, as illustrated in Figure 4.

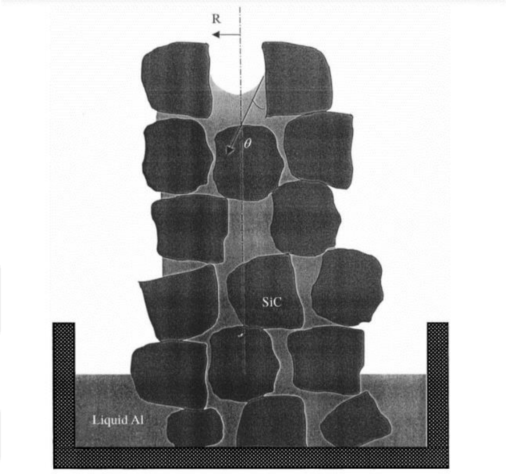

Figure 4. Schematic representation showing the rise of a liquid in a capillary channel that is formed between particles in a porous body.

In Figure 4, R is the capillary radius and Θ the contact angle between the solid particles and the liquid.

In Figure 5, the surface tension magnitude (γ_{lv}) and the void fraction within the powder compact measured 375 mN/m and 0.5, respectively. As shown in Figure 5, contact angles $\Theta > 90$ show the negative capillary pressure suggesting that external pressure is required for infiltration. Conversely, contact angles $\Theta < 90$ end up in positive pressure, indicating the viability of pressureless infiltration under such circumstances.

Various processing factors influence the surface tension and contact angle between Al and SiC particles. As a result, the threshold capillary pressure is required for infiltration. These factors involve alloying additions to Al, the processing atmosphere, and the infiltration temperature and duration. Specifically, Mg and silicon emerge as critical alloying elements in Al alloys tailored for infiltrating SiC beds and preforms. Both elements lower the melting point and enhance the flowability of molten Al. Moreover, silicon has a critical role in mitigating the formation of Al_4C_3 and Al_4SiC_4 during the production of Al/SiC composites. These carbides are known to compromise mechanical properties [24].

Nitrogen gas in the furnace atmosphere is required to improve the wetting of SiC by molten Al. In a recent publication, the authors reported a mechanism that explains the interaction between Mg and N that leads to better wetting of SiC by Al [24].

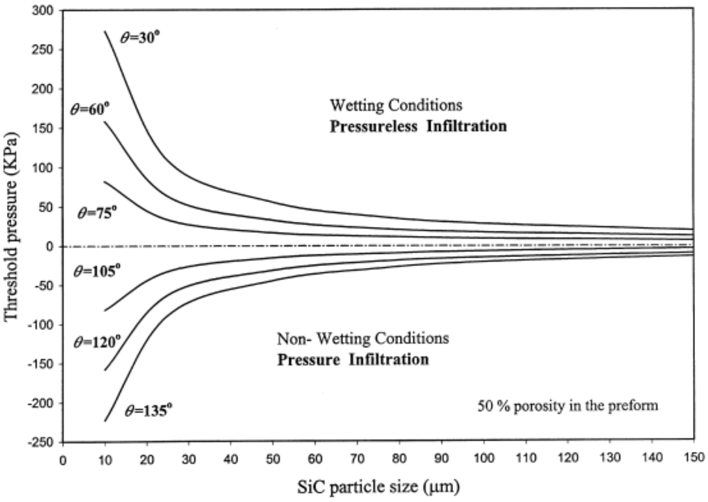

Figure 5. Threshold pressure vs. reinforcement particle size for various contact angles [24].

2.5 Effect of pressure on solidification of metallic materials

In casting technology, the use of pressure enables modulating the solidification process to create new structures and materials and aids efficient melt transfer. The casting solidification and structure formation are influenced by the pressure in two different ways which are mechanical impacts associated with the physical phenomena at the macro degree (elastic and/or plastic deformation, strengthening of heat transfer between casting and mold, cooling rate differences, mold filling control, etc.) and thermodynamic and transport phenomena at the micro degree (phase diagrams changes, physical properties, Gibbs free energy, chemical potentials, specific heat, surface tension, diffusion coefficients, etc). Some essential thermodynamic and kinetic parameters of systems vary by the physical phenomena at both macro- and micro-levels. Therefore, these phenomena affect the phase transformations in the system. The pressure magnitude, the way of its application to solidify melt, the pressure effect durability, and the physical state of melt before pressure application are essential parameters in the application of pressure.

The pressure would be used at various stages, such as during the melting and alloying phase, the transfer of molten material into the mold, at the beginning of casting solidification, shortly before the end of solidification, or after the entire casting has solidified but before it has fully cooled (i.e. when the casting temperature is slightly below the solidus temperature). Additionally, the molten material can be excessively heated or cooled below the liquidus point to create a semi-solid slurry before the application of pressure [27].

2.5.1 P-V-T Equilibrium phase diagrams

Take into consideration two phases with different specific volumes, v_1 and v_2, and in equilibrium. At equilibrium temperature, the specific Gibbs free energies g_1 and g_2 for each phase can be demonstrated as a function of pressure.

$$g_1(P + \Delta P) \approx g_1(P) + \left[\frac{\partial g_1(P)}{\partial P}\right]_T \Delta P = g_1(P) + v_1 \Delta P \qquad (1)$$

and

$$g_2(P + \Delta P) \approx g_2(P) + \left[\frac{\partial g_2(P)}{\partial P}\right]_T \Delta P = g_2(P) + v_2 \Delta P \qquad (2)$$

ΔP is the pressure change. These formulas come from the Taylor series shortened after the first derivative. By subtracting equation (1) from equation (2) and since at the equilibrium temperature $g_1(P)=g_2(P)$, we can express

$$g_2(P+\Delta P)-g_1(P+\Delta P)\approx(v_2-v_1)\Delta P \qquad (3)$$

$$i.e.\ g_2>g_1\ if\ v_2>v_1$$

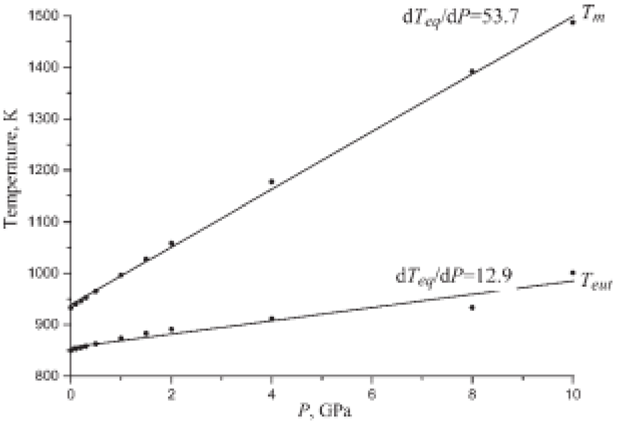

Figure 6. Melting point of aluminum Tm and eutectic temperature of Al-Si system T_{eut} as a function of pressure [27].

This equation indicates that, at a constant temperature, a rise in pressure will cause the equilibrium to transition towards the phase with a smaller specific volume [27].

2.5.2 Pressure effects on equilibrium temperature and pressure induced transformations

The Clausius– Clapeyron equation can be used to express first-order transitions.

$$\frac{dT}{dP}=\frac{v_2-v_1}{s_2-s_1}=\frac{T\Delta v}{I_{1\to 2}} \qquad (4)$$

The equation is associated with the slope of the temperature–pressure boundary for coexisting phases at some point (T, P) to the specific enthalpy of phase transformation $l_{1\text{-}2}$ and the specific volume change Δv. Equation (4) enables to acquire quantitative predictions from thermodynamic parameters for phase transformation and is quite beneficial. The Clausius–Clapeyron equation is also expressed in the equivalence form.

$$\frac{dP}{dT} = \frac{s_2 - s_1}{v_2 - v_1} = \frac{l_{1\to 2}}{T\Delta v} \tag{5}$$

In equation (5), dT/dP>0 and the pressure rise cause an increase in the melting temperature of Tm because most metals and alloys expand within melting. Bi, Sb, Si, and hypereutectic cast iron (Fe+C_{gr}) are among the exceptions. All of these expand during solidification (i.e. the specific volume of the solid is larger than the specific volume of the liquid) so that dT/dP<0 and the increase of pressure diminishes at the melting point. The change of phase transformation temperature according to pressure would be calculated with the formula using the Clausius–Clapeyron equation.

$$T_{eq}(P_0 + \Delta P) = T_{eq}(P_0) + \Delta P \frac{dT_{eq}}{dP} = T_{eq,0} + \Delta P \frac{T_{eq,0}\Delta v}{l_{1\to 2}} \tag{6}$$

The relation between melting point and pressure for Al and eutectic temperature and pressure for the Al–Si system is demonstrated in Figure 1. ThermoCalc software was used to derive these correlations, and the coefficients (dTeq/dP) in equation (6) were found out from the slope. In both scenarios, the temperatures at which phase transformations happen rise with an increase in pressure [27].

2.5.3 Practical aspects of high-pressure liquid phase processing

Squeeze casting employs mechanical methods to apply greater pressures, utilizing specially designed pistons to achieve high pressure during the solidification process. The technique enhances structural quality, reduces the cycle of production, and is practicable to both cast and wrought metals and alloys, as well as their composites. In metal matrix composites produced through squeeze casting, elevated pressures eliminate porosity, and enable capillary penetration of fiber preforms, while also enhancing wetting and bonding between fibers and matrix, consequently improving the load-carrying capacity of the composite. The benefits of squeeze-cast parts include enhanced mechanical properties and resistance to thermal fatigue and corrosion. Pressure improves the bonding of chemical phases present in a substance. For this reason, it also impacts the electrical and magnetic properties of the material. The reasons for the desirability of squeeze casting products are their microstructural refinement, integrity, and improved physical and mechanical properties, making them acceptable for a variety of crucial applications.

Elevating the pressure during the solidification of casting enhances thermal contact between the casting and the mold. This is attributed to the plasticity of the metal slurry and the close solidification temperature of the solid phase. Enhanced thermal contact leads to higher heat removal from the casting resulting in an augmented cooling rate and temperature gradient within both the casting and the molten material, leading to an increase in melt undercooling (ΔT). The critical radius for nucleation in the solid phase decreases in direct proportion to ΔT, while the free energy for nucleation decreases by $1/(\Delta T)^2$. The nucleation rate experiences a more rapid increment because the free energy term is within the exponent. This indicates that the solidification of the casting will be expedited due to abundant nucleation, leading to the formation of a cast structure with finer grains. It is crucial to keep in mind that pressure also influences the temperature at which equilibrium phase transformations occur and the surface tension. The real values of ΔT, Tm, and $\sigma_{\alpha\beta}$ would be used in each specific case for exaction. The reduction in grain size leads to an enhancement in the microhardness, mechanical strength, and corrosion resistance of the cast material [27].

It was explained that, for most metals and alloys, the application of high pressure contributes to structural refinement due to the following considerations:

1. Decrement in critical radius for new phase nucleation

2. Raise in rate of new phase nucleation

3. Reduction in interfacial free energy [27]

2.6 Squeeze Cast Infiltration

Squeeze casting appears as an attractive manufacturing technique for Al MMCs, offering improved mechanical properties attributed to reduced common defects like porosity and shrinkage voids, as well as the elimination of segregation of the reinforcement [26] [28].

The primary benefits of squeeze casting are:

- Components produced are free from gas porosity or shrinkage porosity.
- Feeders or risers are not required and therefore no metal wastage occurs.
- Alloy fluidity (castability) is not a limiting factor in squeeze casting as both common casting alloys and wrought alloys can be squeeze cast to a finished shape with the support of pressure.
- squeeze castings can exhibit mechanical properties as good as wrought products of the same composition.

Residual porosity is related to the insufficient wetting of SiC by molten Al and undesirable reactions or phases that form due to the dissolution of the SiC reinforcement in the liquid Al.

At temperatures that are higher than the melting point of Al, and under standard atmospheric pressure, SiC becomes thermodynamically unstable. This can lead to interfacial reactions that produce compounds like Al_4C_3 and Al_4SiC_4.

$4Al + 3SiC = Al_4C_3 + 3Si$

Because of the cooling impact of both the preform and the mold, the interaction time between the reinforced particles and the molten Al was reduced, decreasing the chance of interfacial reactions. In a different approach, when the SiC preform was heated to 600 °C, it led to the development of SiO_2 oxidation layers on the SiC particles. These SiO_2 layers act as a shield, preventing direct contact between the SiC and the molten Al, thereby preventing the presence of the Al_4C_3 [29].

The C atoms that dissolve in the solution are prone to quickly combine with Al, resulting in the formation of Al_4C_3, either as a continuous layer or as separate deposits surrounding the SiC particles. Not only does this reaction led to the breakdown of the SiC reinforcing particles and weaken the composite, but also both Al_4C_3 and Al_4SiC_4 are also thermodynamically unstable. They slowly react with atmospheric moisture to produce Al-hydroxide, which promotes crack growth in the composite due to the moisture-driven corrosion of the Al_4C_3 phase [30].

There are two different variations for the squeeze casting which are the direct and the indirect techniques. The pressure is applied to the whole surface of the liquid metal in the direct squeeze casting which leads to fully dense casting. This method promotes the fasted heat transfer which leads to the finest grain structure. As a result, it is frequently employed for crafting high-integrity castings and components for metal matrix composites [31].

In the squeeze infiltration, a movable mold part (ram) is used for applying pressure on the molten metal and forcing it to penetrate a performed dispersed phase, placed into the lower fixed mold part and infiltration occurs [32].

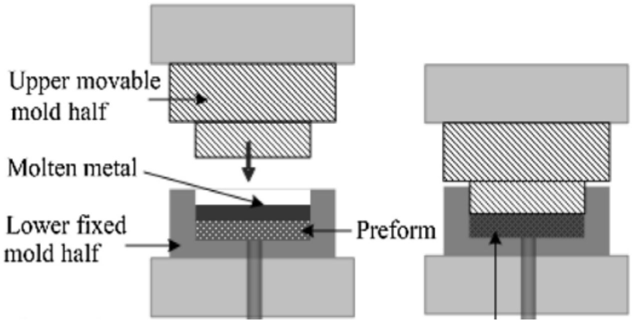

Figure 7. Squeeze infiltration schematic [32].

In squeeze casting, the applied pressure enhances the wetting ability and bond strength between the Al alloy and SiC. This pressure has an undercooling effect, combined with heat dissipation through the dies, and promotes rapid solidification. Additionally, the elevated pressure suppresses the formation of gas bubbles [29].

The high pressure also decreases the size of the gas bubbles but may be absorbed into the solution and disappear in a bubble-free casting. Applied pressure on the primary α phase can decrease the grain size and secondary dendrite arm spacing. The pressure is applied to obtain the largest melt undercooling. By doing that, the nucleation rate can be increased exponentially when the melt temperature in the die is lower than the liquidus temperature. When the higher cooling rate and large undercooling effect are applied to melt, there would be an expected refinement change in the structure of the squeeze cast samples [29]. However, some studies proved that SiC is more compatible with Al alloys and imparts better tensile and wear features as compared to other reinforcements [33].

In addition, this high pressure not only diminishes the size of the gas bubbles but may lead to a bubble-free casting by absorbing the bubbles into the solution. When pressure is applied to the primary α phase, it can lead to a reduction in grain size and secondary dendrite arm spacing. This applied pressure aims to obtain the largest melt undercooling which leads to exponentially boosted nucleation rate while the melt temperature in the die was lower than the liquidus temperature. With increased cooling rates and large undercooling effects on the melt, structural refinement is expected in squeeze cast samples [29]. Research indicates that SiC exhibits more compatibility with Al alloys, offering enhanced tensile and wear properties compared to other reinforcements [33].

In Figure 8, various temperature profiles of the preform are analyzed during the infiltration process. At a preheated preform temperature of 550 °C, the Al melt successfully penetrates the porous SiC particulate compact. The temperature changes of both the Al melt and the SiC preform throughout the pressure infiltration casting procedure were monitored using two thermocouples, as shown in Figure 8 [34].

One thermocouple was immersed in the Al melt, while the other was put into the SiC compact. The temperature is monitored and after pouring, it shows a rapid decrease.

A steady isothermal temperature was observed at the solidification point of 660 °C. Subsequently, a slow cooling occurred, and solidification was completed. Thermal equilibrium between the SiC preform and the Al melt was observed after 20-70 seconds(sec) passed from the pouring of the Al melt to the SiC preform which is preheated to 550 °C [34].

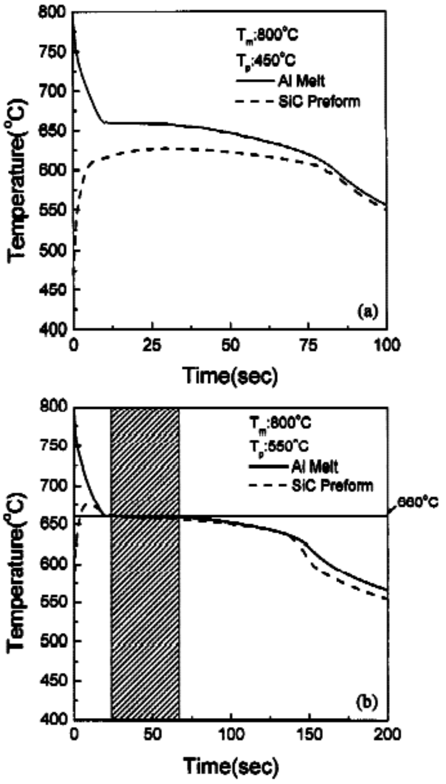

Figure 8. Temperature profiles of Al melt and SiC preform during pressure infiltration casting process at Al melt temperature 800 °C, infiltration pressure 50 MPa, and two different SiC preform preheat temperatures [34].

Conversely, when the SiC compact is preheated to 450 °C, its temperature becomes lower than the Al melt during the solidification phase after pouring. This reduced preheat temperature of 450 °C accelerates the solidification of the Al melt on the preform's surface, creating a barrier that hinders complete infiltration near the surface and the infiltration could not be completed everywhere inside the compact. It appears that an optimal infiltration duration lies between 20 to 70 seconds after the pouring, given a melt temperature of 800 °C and a SiC compact preheat temperature of 550 °C.

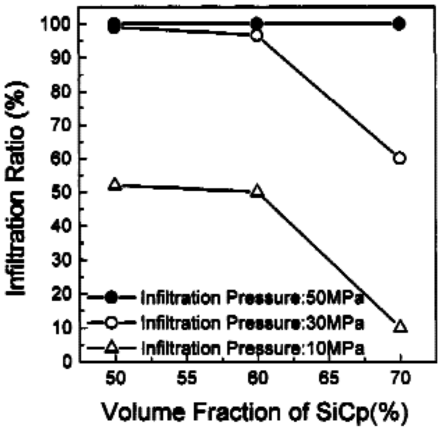

Figure 9. Effect of volume fraction of SiC on infiltration ratio [34].

Figure 9 illustrates the influence of infiltration pressure on the infiltration ratio of the Al melts for SiC compacts ranging from 50 to 70 vol%. The tests were conducted for the Al melt whose temperature is around 800 °C and the preheat temperature of the compact was 550 °C. As the volume fraction of the preform increases, the voids between the SiC particles decrease. For 70 vol% SiC preform with bimodal SiC particles, the necessary infiltration pressure was 50 MPa, exceeding the required pressure for the 50-60 vol% SiC preforms with unimodal SiC particles. This result occurs because the interparticle spacing in the 70 vol% SiC preform (2.3 mm) with bimodal particles is narrower than the 50-60 vol% SiC preform (ranging from 5.0 to 5.7 mm) with unimodal particles. Based on these results, for the compacts comprising 50 vol% SiC or more, an infiltration pressure of at least 50 MPa must be applied to obtain the complete infiltration [34].

2.7 Sintering of the Al-SiC for Al Particles

Al is a good choice for many applications due to its features such as lightness, high strength, and corrosion resistance. There are methods for making Al powder in suitable sizes in powder metallurgical forming processes. Al powder made by these methods can be pure Al or an Al alloy.

The reaction between Al and oxygen is very fast and strong. As a result of this reaction, Al_2O_3 is formed. The reaction rate causes an Al_2O_3 film to be formed immediately when even small amounts of atmospheric oxygen or water vapor (H_2O) come into contact with an Al surface. The thickness of the resulting Al_2O_3 film is in the range of approximately 30 to 90 nm. Al_2O_3 film almost does not allow the transition of both Al and oxygen. Few elements can react with oxygen more easily than Al. For this reason, once the Al_2O_3 film is generated, it exhibits high stability and resilience against chemical corrosion.

Thus, a protective Al_2O_3 film is present on the surface of each particle of Al powder made. There are some problems caused by Al_2O_3 film in the process of making metallurgical parts from Al powder. Since it shows high chemical stability, it reduces the sinterability of the Al particles for the same temperature range. To create a functional product by connecting individual Al powder particles, it is crucial for the metal atoms in one particle to directly interface with the metal atoms of neighboring particles. This process establishes metallurgical bonds, enabling atomic migration between particles and the rearrangement of atoms along the interparticle boundary. Nevertheless, the Al_2O_3 films on the powder surfaces prevent the interparticle atom migration.

The process for sintering Al powder provides easier methods than prior methods. This technique includes heating Al powder within a nitrogen (N) atmosphere with a partial pressure of H_2O ranging from approximately 0.001 KPa to about 0.02 KPa. This process leads to the sintering of Al powder, achieving a transverse rupture strength of at least around 13.8 MPa. Additionally, this is carried out without the use of a sintering aid or the application of mechanical force to break the Al_2O_3 film before or during the powder's heating [35].

In this method, which takes place in an N atmosphere, H_2O with a partial pressure in the range of 0.001-0.02 KPa plays a role in the sintering of Al powder. This role is the releasing of atomic hydrogens into the oxygen vacancies on the Al_2O_3 surface. The Al_2O_3 film moves away from the Al powder particles with the help of the diffusion of hydrogen into the alumina film. Removal of the Al_2O_3 film allows metal-to-metal contact of adjacent Al powder particles. This phenomenon results in mass transport, which is necessary to initiate and sustain the sintering process, which results in the Al powder particles condensing and metallurgically bonding together.

The resulting Al powder could contain one or more ceramic powders. Al_2O_3, silica, SiC, BN, and refractory metal carbides, such as tungsten carbide, are examples of such powders. The quantity and dimensions of the ceramic powder are controlled to assist the obtainment of the necessary level of sintering for the Al powder.

Any furnace capable of maintaining a controlled composition atmosphere is sufficient to complete the process of heating Al powder in the shaped or unshaped state. The heat capacity of the furnace should reach the sintering temperature of Al powder. Sintering can occur in three different ways which are liquid phase sintering with a sintering aid, Super solidus liquid phase sintering, or solid-state sintering.

Temperature between 550 °C and 650 °C is a general sintering temperature. Using a temperature outside this range is related to the composition & particle size distribution of the Al powder and the desired degree of sintering. The exposure time of Al powder to the sintering temperature also depends on the same factors [35].

Increasing the density created by the sintering method is the most efficient way to enhance the performance of the resulting materials. Optimum sintering parameters make it possible to reach 99% of the theoretical density of the reference material. In Avcı and Gulec’s research, how the microstructural and mechanical properties of pure Al samples are affected by the sintering process was examined. Sintering processes last 45, 60, and 75 min and are applied at temperatures of 500 °C, 550 °C, and 600 °C, respectively. Avcı and Gulec reported that the experiments at different sintering temperatures for different durations demonstrated the lowest structural gap was observed following a sintering process at 600 °C for 45 minutes. the most optimal microhardness value was calculated as 58 HV following a sintering process at 600 °C for 45 min [36].

2.8 Stress-Induced and Melt-Activated Process

The Stress-Induced and Melt-Activated (SIMA) process ranges among the most efficient solid-state methods achievable in the trading area. According to the procedure of this method, the deformed material is reheated to a semi-solid state.

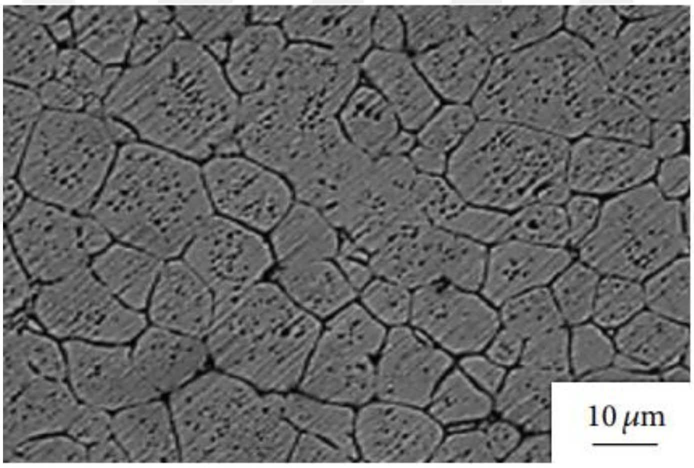

Figure 10. Microstructure of deformed Al 7075 alloy obtained by the SIMA process in the case of being isothermally held for 5 min at 620 ° C.

The primary deformation occurs when the recrystallization temperature is exceeded (hot working). The following process is cold working at room temperature. This step has an important role in storing the energy flow resulting from partial remelting. In this way, the material becomes semi-solid, resulting in the formation of coherent, non-dendritic, spherical solid particles suspended in a liquid matrix.

Partial re-melting applied to the deformed material results in the formation of non-dendritic microstructures. With re-melting, recrystallization becomes easier, and fine, non-dendritic microstructures are formed as the liquid penetrates high-angle grain boundaries. Liquid metal leaks through high-angle grain boundaries, resulting in the formation of spherical solid particles in the liquid matrix once recrystallization is complete.

Heating rate and cold work degree directly affect the size of spherical solid particles. The size of the particles formed can be as small as 30 μm. This method is good enough to be considered a potential competitor to the MHD process. Figure 10 shows the microstructure of Al7075 Al formed because of the SIMA process [37].

2.9 Wear Test of the Al6061-SiC MMC

The resistance an object encounters while moving on another object is called friction. The friction coefficient, denoted by the symbol μ, is a dimensionless quantity that imposes the relationship between the frictional force (F) acting between two surfaces and the perpendicular force (P) pushing them against each other. Mathematically, it can be defined as:

$$\mu = F/P$$

Engineers and scientists are investigating methods to enhance tribological behaviors of metallic materials. One approach to reduce the friction coefficient involves the application of coatings. DLC, for instance, when applied to metals like Al, can decrease the friction coefficient to less than 0.1. Another strategy to enhance the wear performance of metals is the incorporation of appropriate reinforcements into metal matrices to create composites. Different types of reinforcements, such as Al2O3, SiC, and B4C, are usually integrated into metal matrices. These reinforcements not only enhance the mechanical features of the composites but also improve their frictional behavior and wear resistance. Furthermore, the friction coefficient of Al-based MMCs is typically lower than that of unreinforced Al alloys [38].

Wear is the gradual material loss when there is a relative movement between two surfaces. Numerous studies have dug into the tribological characteristics of MMCs, and the results indicate that the wear strength of the MMCs is higher than that of unreinforced matrices as is shown in Figure 11. For instance, the pure Al6061 alloy has a much higher wear rate than the Al6061 MMCs which are reinforced with different amounts of SiC particles as shown in Figure 11. Conversely, just in specific conditions where the wear resistance of the MMCs may be lower or comparable to those of unreinforced matrices [38].

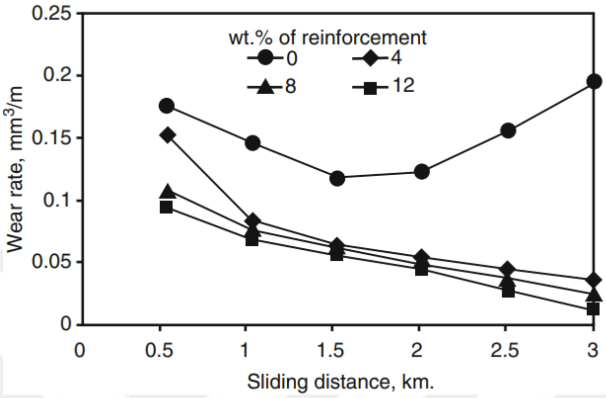

Figure 11. Variations of wear rate with sliding distance for Al6061-based MMC at an applied load of 10 N and sliding velocity of 1.85 m/s [38].

Different wear mechanisms can occur on the object's surface during the sliding movement against each other. These mechanisms are adhesive wear, abrasive wear, delamination wear, erosive wear, fretting wear, fatigue wear, and corrosive/oxidative wear. Adhesive wear, abrasive wear, fatigue wear, and corrosive/oxidative wear are frequently used wear mechanisms of MMC. Occasionally, abrasive wear takes place when hard particles entrapped at the interface cause abrasive action against the surfaces in contact. While both metallic and nonmetallic particles may contribute to abrasive wear, most of the time nonmetallic particles predominantly lead to abrasion in MMCs [38].

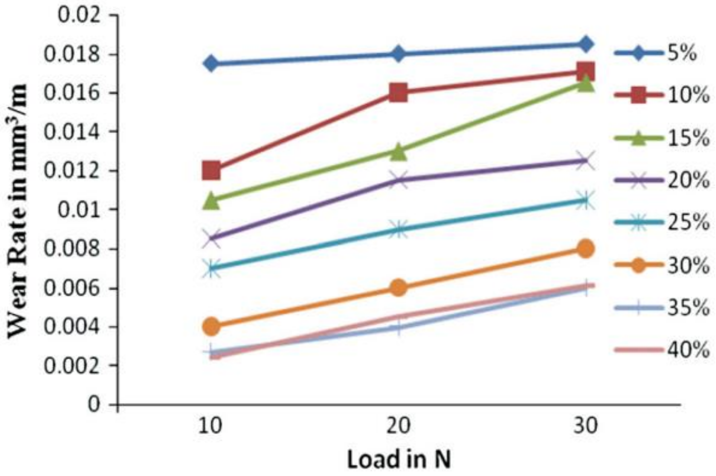

Figure 12. Wear rate versus load for 150 mesh size of SiC reinforced MMCs [39].

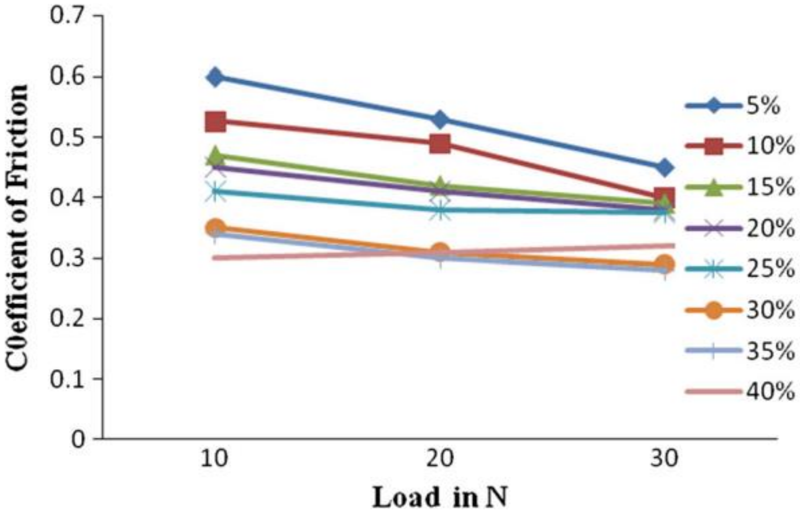

Figure 13. Coefficient of friction versus load for 150 mesh size of SiC reinforced MMCs [39].

In this study, the relationship between the wear resistance and friction coefficients of Al-6061-based composites reinforced with SiC particles and the applied load was investigated. The production method of the composites used is squeeze casting and the mesh size of the SiC used is 150. The weight fraction of SiC varies between 5, 10, 15, 20, 25, 30, 35 and 40%.

In the studies, dry sliding wear properties of the composites were observed using a Pin-on-disk testing machine. The experiments were completed with a sliding distance of 2000 m and a sliding speed of 2 m/s, using various loads of 10, 20, and 30 N. As an outcome of the studies, it was determined that the wear level of the metal matrix decreased up to 35% SiC weight ratio as it can be seen in Figure 12. This trend is due to the clustering of SiC particles and then due to an increase in weight settling down at the bottom and non-uniform mixing in the Al matrix. The reason is that the SiC particles gather. The almost identical outcomes up to 25 % reinforced Al/SiC MMCs expressed by Singla et al. and Umanath et al. The results also indicate that increasing load and sliding distance cause wear of the test specimens. The coefficient of friction decreases with increasing reinforcement material weight fraction as it can be seen in Figure 13 [39].

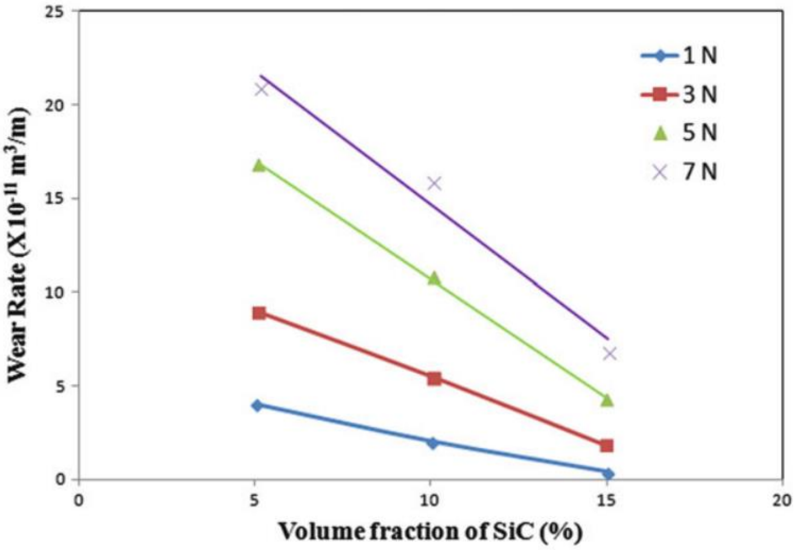

Figure 14. Effect of volume fraction of SiC on the wear rate of Al metal matrix composite [36].

Figure 14 illustrates the wear rate of the Al MMC, which is strengthened with micron-sized SiC particles, based on the volume fraction of SiC particles under varying loads. As the volume fraction of SiC particles rises, there's a linear decrease in the composite's wear rate. This indicates that the wear resistance of the composite is proportional to the volume fraction of the reinforcement [38].

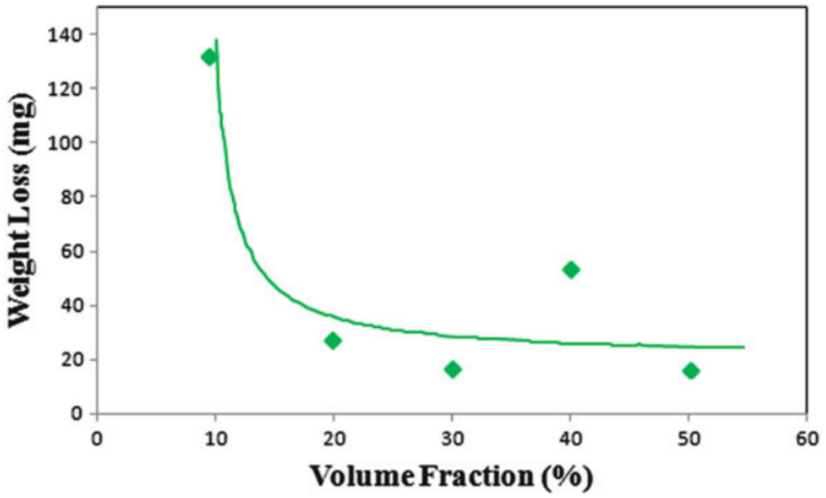

Figure 15. Weight losses of the Al composite with vol% of SiC as reinforcement [38].

Surprisingly, the advancement in the wear rate of the composite decreases significantly with increasing the volume fraction of micron-sized reinforcements above 20 vol%. As shown in Figure 15, the weight loss of 10–50 volume fraction SiC-reinforced Al alloy (Al-1080) with particle size 20 µm declines as the volume fraction of SiC particles increases. Weight loss reduces importantly to up to 20% of the reinforcement volume. Besides, over 20 vol%, weight loss reduces by an insignificant amount with increasing volume fraction of particles. Other researchers have also demonstrated this trend. Additionally, if the composite is advised for structural applications, it is suggested that the ceramic ratio for MMCs reinforced with ceramic particles be no more than 30% by volume [38] Interestingly, it is observed that the impact of the volume fraction of micron-sized reinforcements on the wear strength beyond 20 vol% significantly diminished. For the Al alloy (Al-1080) reinforced with SiC particles ranging from 10% to 50% in volume fraction with a particle size of 20 µm, there is a significant reduction in the weight loss up to a 20 vol% reinforcement as shown in Figure 15. However, beyond this point, the decrease in weight loss with increasing reinforcement volume fraction becomes negligible. Additionally, it's a prevalent recommendation that if

MMCs are strengthened with ceramic particles and intended to be used for structural purposes, the ceramic volume fraction should not surpass 30 vol% [38].

CHAPTER 3

EXPERIMENTAL PROCEDURE

3.1 Powder Preparation

Firstly, the powder mixtures were prepared with the traditional powder preparation methods. Since the raw powder is not appropriate for the pressing to obtain a defect-free green body, the raw powder was combined with the binders. The ingredients used in the powder preparation are shown in Table 5.

Table 5. Ingredients of ready-to-press (RTP) powder.

Ingredients	**Amount**
SiC	200 g
Fructose	4 g
Peg6000	8 g
Distilled Water	200 ml

The distilled water was heated, and binders were put inside of it and mixed by magnetic stirring. After all the binders were dissolved, the solution was put inside the raw SiC powder and mixed. After that, the mixture was put in the furnace and the water slowly evaporated. Finally, the resultant compact was crushed and ground to the sieves, and RTP powder was obtained.

Figure 16. The RTP SiC powder.

The resultant powder was divided into three categories. For specimen 1, %100 SiC powder was used and for specimen 2 and 3, the powder was mixed with the pure Al powder.

Table 6. The powder ingredients for hot and cold preform preparation.

Specimen No	**Total weight (g)**	**SiC (g)**	**Pure Al (g)**
1	50	50	0
2	50	20	30
3	50	20	30

3.2 Ceramic Preform Production

The Die assembly of the machine was specially designed for three-point flexural test specimens. It was made of H-13 hot work tool steel.

The specimen is 120 mm in length, 40 mm in width, and approximately 10 mm in thickness. The thickness of the specimen can be changed thanks to an adjustable lower punch level in the z-direction.

For specimen 1 which is shown in Table 6, it is directly placed into the hydraulic pressing mold. To obtain the green body, hydraulic pressing was used and 100 MPa pressure was applied to the 50 g powder for a 10 s. After that, the specimen is debonded around 500 °C for 2 h, then sintered for 2,5 h around 1400 °C. This is lower than the sintering temperature of the SiC which is above 2000 °C and the reason is to obtain a porous ceramic compact.

For specimens 2 and 3, the powders were moisturized with a mixture which consists of fructose and distilled water. After that, they were ground again. Specimen 2 was put into a mold and applied 100 MPa for 10 s. Specimen 3 was put into a mold and applied 80 MPa for 10 s. The pressure applied to specimen 3 was lower than specimen 2 due to the higher porosity requirement for better infiltration during cold preform squeeze casting. As a result, green bodies were obtained. After that, the green bodies were debonded around 300 °C for 2 h. The debinding and sintering temperature profiles are shown in Figure 17.

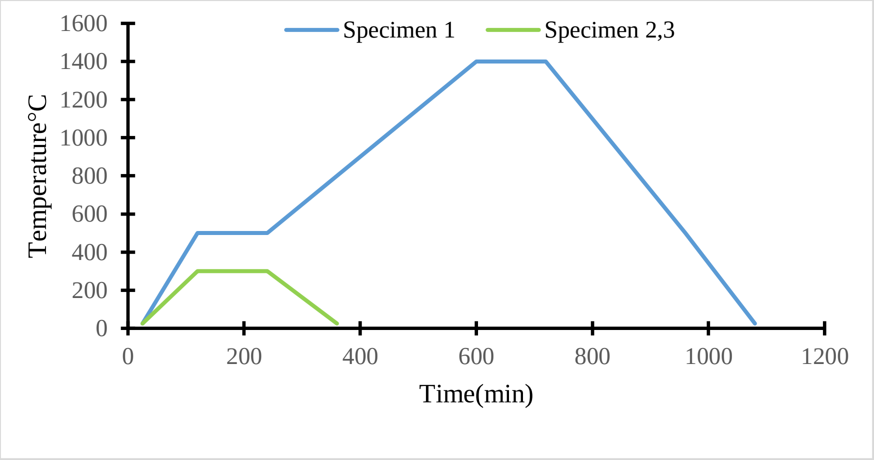

Figure 17.Temperature profiles of the specimen 1, 2, and 3 for the debinding and sintering processes.

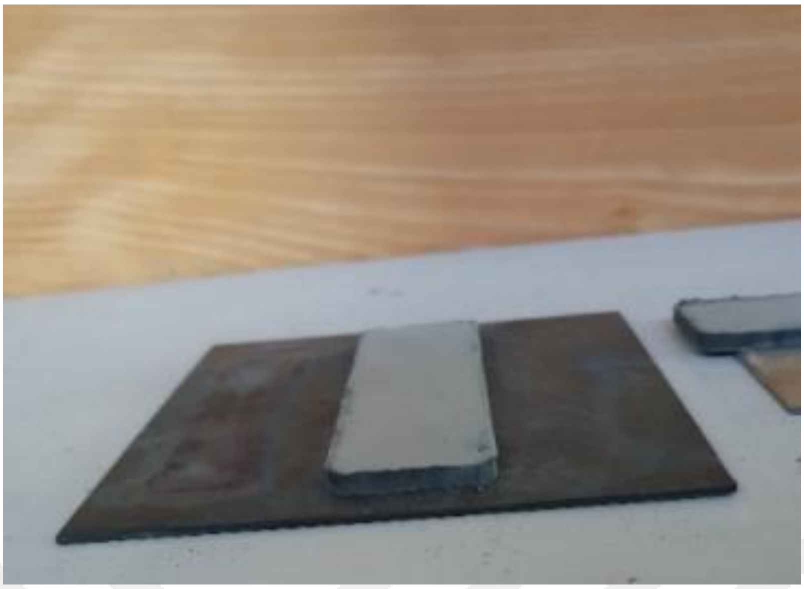

Figure 18. Green body after consolidation.

3.3 Squeeze Cast Infiltration

Two different types of routes have been chosen for the squeeze cast infiltration which are hot preform melt infiltration for specimens 1 and 2, and cold preform melt infiltration for specimen 3.

For specimen 1, 2 wt% Mg added Al6061 alloy melted around 750 °C, and the ceramic compact was preheated to 1000 °C. The mold of the hydraulic press was preheated to 300 °C. When the setup was ready, the ceramic preform was placed inside the mold and molten Al was poured on top of it and 100 MPa of pressure was applied immediately. The finalized specimen was obtained. A similar procedure was applied to specimen 2, but the only difference is the compact preheated to 800 °C since it involves Al powder. If it was heated to 1000 °C, the Al particles would be completely semi-solid, and the compact could not be placed into the mold.

For specimen 3, the Al6061 alloy again melted around 750 °C, but the ceramic compact was not heated. The mold of the hydraulic press was heated to 300 °C. When the setup was ready, the ceramic compact was put inside the mold and melted Al was poured on it and 100 MPa was applied. After that, the finalized specimens were sintered in a vacuum sinter furnace at 600 °C around 1.5 h under 10^{-4} bar. The reason is that since the compacts were cold during infiltration, all the pores inside the body could not be filled with liquid Al. As a result, the sintering process is applied to the specimens if there are remaining pores from the squeeze cast process.

Figure 19. Experimental setup of squeeze casting and stages of MMC’s processing and SiC infiltrated alloy composite.

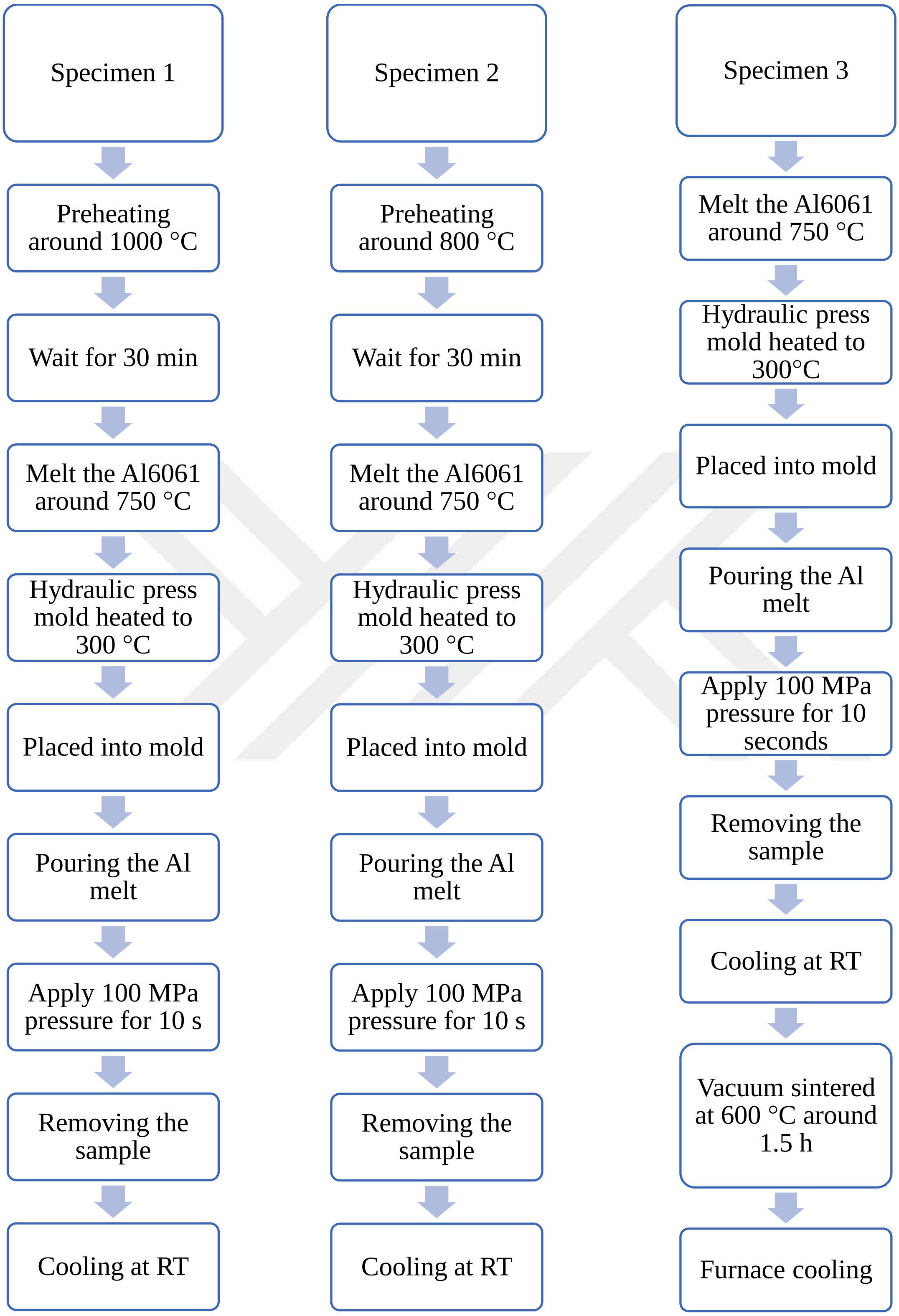

Figure 20. Flowsheet showing the steps for squeeze cast applications for specimens 1,2 and 3.

3.4 Characterisation of the samples

3.4.1 X-Ray Diffraction (XRD) Analysis

An X-ray diffraction analyzer (XRD, BRUKER, D8 ADVANCE) was used to determine the crystal structure and the phases of the squeeze cast infiltrated Al-SiC composites and the crystal structure of SiC particulates. X-ray analyses were done using Cu-Kα radiation ($\lambda = 1.5418$ Å) between 2θ of 10° and 90° at a voltage of 40 kV at a scan rate of 2 °/min. XRD patterns were investigated by DIFFRAC. EVA V3.1 integrated X-ray powder diffraction software.

3.4.2 Scanning Electron Microscopy (SEM) and Energy Dispersive Spectroscopy (EDS) Analysis

Microstructural analysis of starting powders and squeeze cast infiltrated composite structures was studied with a scanning electron microscope (SEM, JEOL, JSM-6400). Before the SEM examinations, samples were hot-mounted with bakelite, and metallographic sample preparation methods were applied to the surface. During the examination, the operational voltage varied from 5 to 20 kV.

3.4.3 Particle Size Analysis

Particle size analysis of starting powders was done by Malvern Instruments Mastersizer 2000 particle size analyzer. The measurable particle size range was 0.020 to 2000 µm. For the starting raw SiC powder and RTP SiC powder, the measurements were done. Size measurement data was established by taking the mean average of the measurements.

3.4.4 Optical Microscopy

Al6061 reinforced composite materials were characterized under optical microscopy examination. Nikon Eclipse LV150 which is an inverted materials microscope was used in optical microscopy observations. X50, X100, X200 and X500 magnifications were used to examine details in microstructures. It was aimed to find out the distribution of reinforcement material in metal matrix. Both hot preform and cold preform squeeze cast infiltrated specimens were examined.

3.4.5 Image Analyzer

Dewinter Materials Plus Image analyzer software was used and approximately the area % of the matrix and the reinforcement were determined quantitatively. The magnification used in the examination is X100. Microstructures of as-cast and heat-treated Al composite samples were analyzed metallographically. The photographs of samples were taken. An image analyzer study was conducted to determine the volume percentage of SiC-reinforced Al6061 alloy composites. The software was used to compute the area percentages of SiC and the Al matrix. These computed areas offer an approximate indication of the volume percentages of the reinforcement and matrix.

3.4.6 Hardness test

The hardness testing machine of Struers Duramin-500 made by EMCOTEST was used in hardness tests. The hardness tests were carried out by using HBW 2.5/62.5 according to the ASTM-E10. The tungsten ball diameter used in the test is 2.5mm and 62.5 kgf was applied to the squeeze cast infiltrated specimens. Then, the average of the results was calculated.

3.4.7 Wear test

UTS Tribometer T10 testing machine, which is in the Karabuk University, Steel Research Institute, Tribology laboratory used for the calculations of the wear rate and the coefficient of friction. The tests were conducted according to the ASTM G133. The tests were carried out under the normal loads of 10, 15, and 20 N, a sliding distance of 100 m, and a stroke distance of 5 mm.

CHAPTER 4

RESULTS AND DISCUSSION

4.1 Characterization of Starting and RTP Powder

In this chapter, the results of the experimental study examined the raw and RTP SiC powder by scanning electron microscope, energy dispersive spectroscopy, and particle size analysis.

The particle size histogram of the raw SiC powder is shown in Figure 21. Although there is a small peak at ~6 µm size, the volume percentage of the particles that pile up around this particle size is quite small. Consequently, it is assumed that the powder has unimodal particle size distribution. The average size of the particles ranges from 21.4 to 53.5 µm. Particle size distribution of SiC raw powder is shown in Table 7. which involves Dx (10), Dx (50), and Dx (90) values.

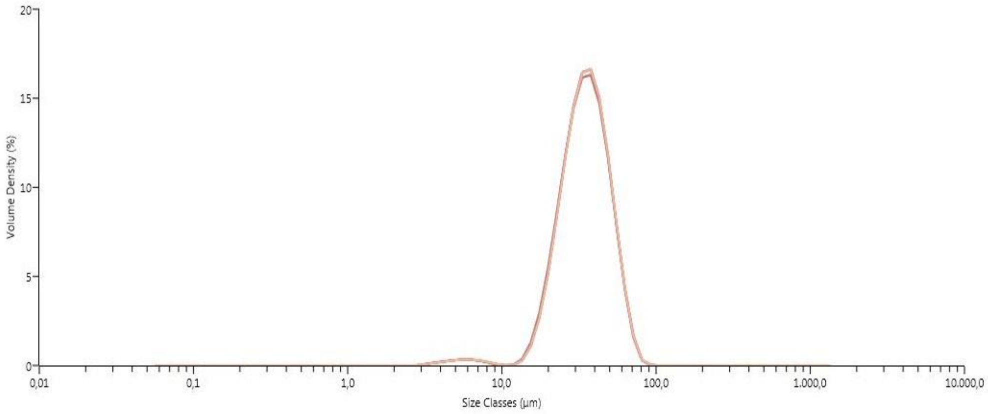

Figure 21. Particle size distribution of SiC plain raw powder.

Table 7. Particle size distribution of plain raw SiC powder.

Number/Distribution	**Dx (10) (µm)**	**Dx (50) (µm)**	**Dx (90) (µm)**
1	21.2	34.5	53.4
2	21.3	34.6	53.5
3	21.3	34.6	53.6
4	21.5	34.7	53.3
5	21.5	34.8	53.4
6	21.5	34.8	53.4
7	21.6	34.8	53.6
Mean	21.4	34.7	53.5

The particle size histogram of the RTP SiC powder is shown in Figure 22. Although there is a small peak at ~6-7 µm size, the volume percentage of the particles that pile up around this particle size is again quite small. Consequently, it is assumed that the powder has bimodal particle size distribution as expected because powder preparation techniques were used with binders to obtain sufficient pressing and defect-free green body. The average size of the particles ranges from 25.6 to 327 µm. Particle size distribution of RTP SiC powder is shown in Table 8. which involves Dx (10), Dx (50), and Dx (90) values.

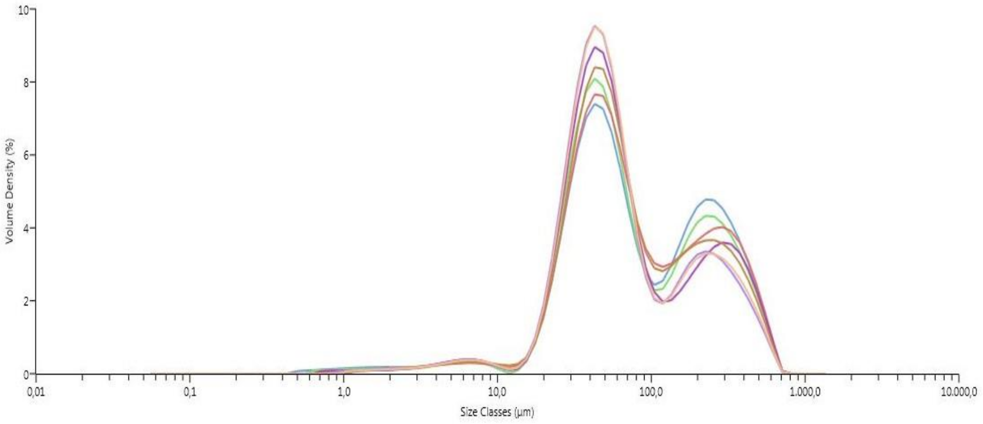

Figure 22. Particle size distribution of RTP SiC powder after mixing with binders then, screening for classification.

Table 8. Particle size distribution of RTP SiC powder after mixing with binders then, screening for classification.

Number/Distribution	Dx (10)(μm)	Dx (50)(μm)	Dx (90) (μm)
1	25.5	68.1	347
2	25.7	62	336
3	26.2	66.1	349
4	25.4	56.8	338
5	26.2	61.4	323
6	25	53.5	292
7	25.3	54.3	301
Mean	25.6	60.3	327

A representative SEM image of raw SiC powder is shown in Figure 23. SEM shows that the powder consists of particles that are closer and slightly bigger than 50 μm, and smaller than 50 μm. This particle size examination from SEM supports the data from the particle size measurement data collected which are shown in Table 7. and in Figure 21. In addition, the particles have sharp-edged particle structures.

Figure 23. SEM image of raw SiC powder used for reinforcement.

Also, the EDS analysis was applied to the raw SiC powder particles which is shown in Figure 21. The analysis in Figure 25 reveals that the ceramic powder consists of only Si and C. There is no contamination in the SiC powder which would affect the final microstructure and squeeze casting procedure.

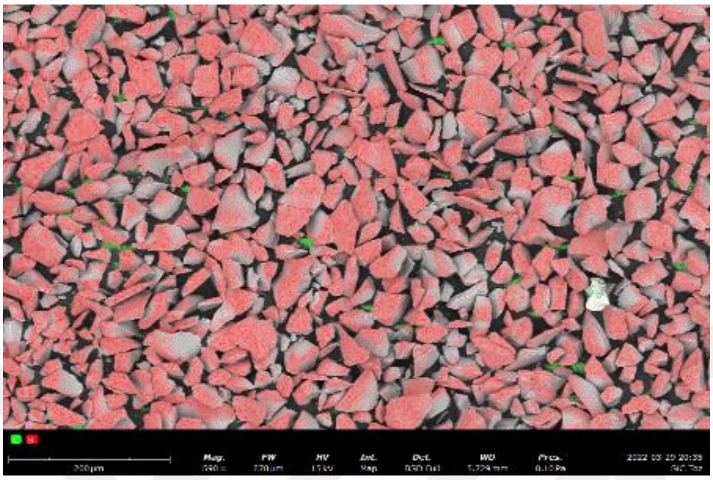

Figure 24. Map analysis of raw SiC powder. The red color shows the Si area, and the green color shows the carbon area

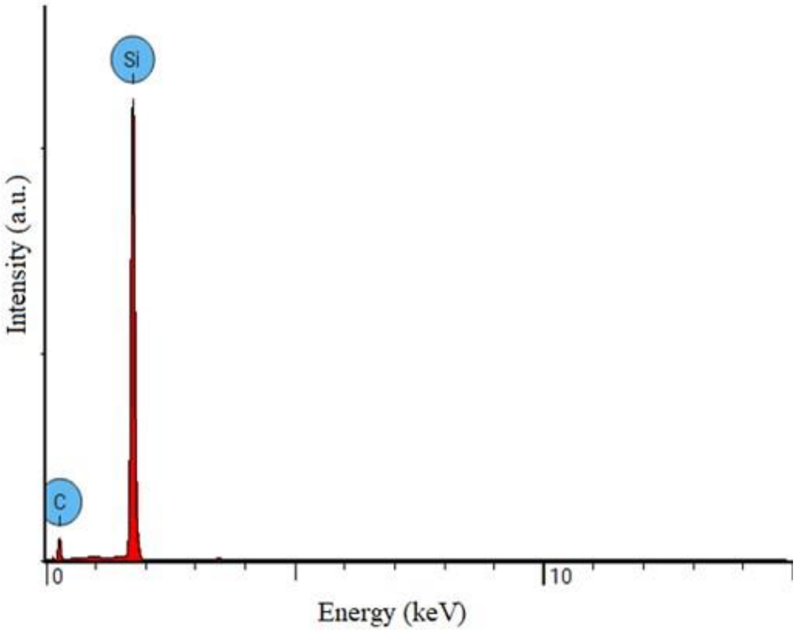

Figure 25. EDS Analysis of raw SiC powder.

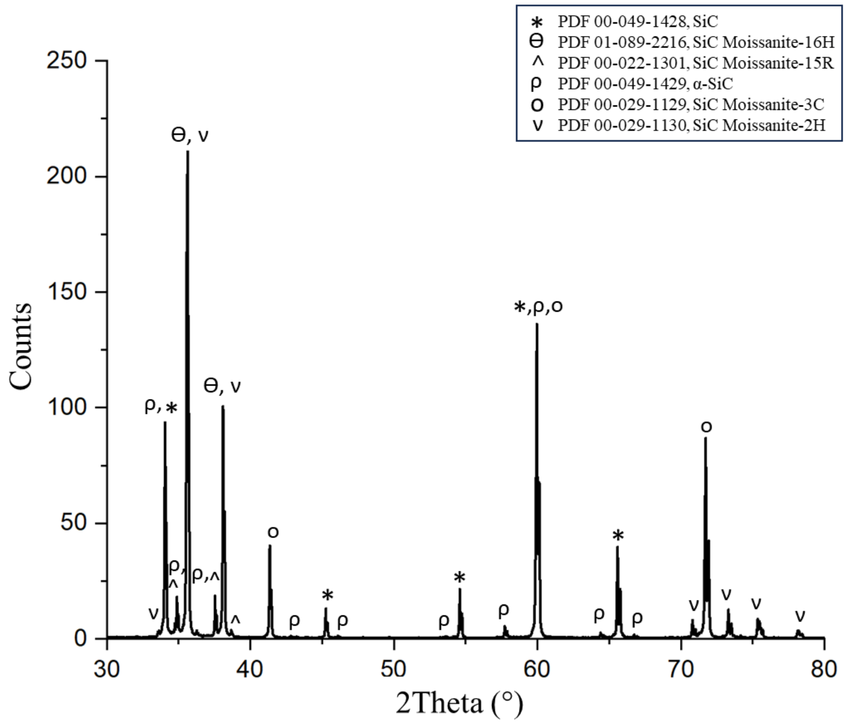

Figure 26. XRD Analysis of the raw SiC powder

SiC powders were supplied from KLA Exalon, Norway. Figure 26 shows that the structure of the SiC is α-SiC, hexagonal 16H with some rhombohedral 15R and sometimes some hexagonal 2H. The powder does not contain any contamination or other oxides. It involves only SiC particles with different crystal structures.

4.2 Characterization of the Squeeze cast SiC-Al Composites

4.2.1 Hot Preform Squeeze Casting Infiltration of 100 % SiC Compact

Hot preform infiltrated specimens were characterized by XRD, SEM, EDS, optical microscopy, and image analyzer software programs.

4.2.1.1 XRD Analysis

XRD analysis of the hot preform infiltrated specimen 1 was given below.

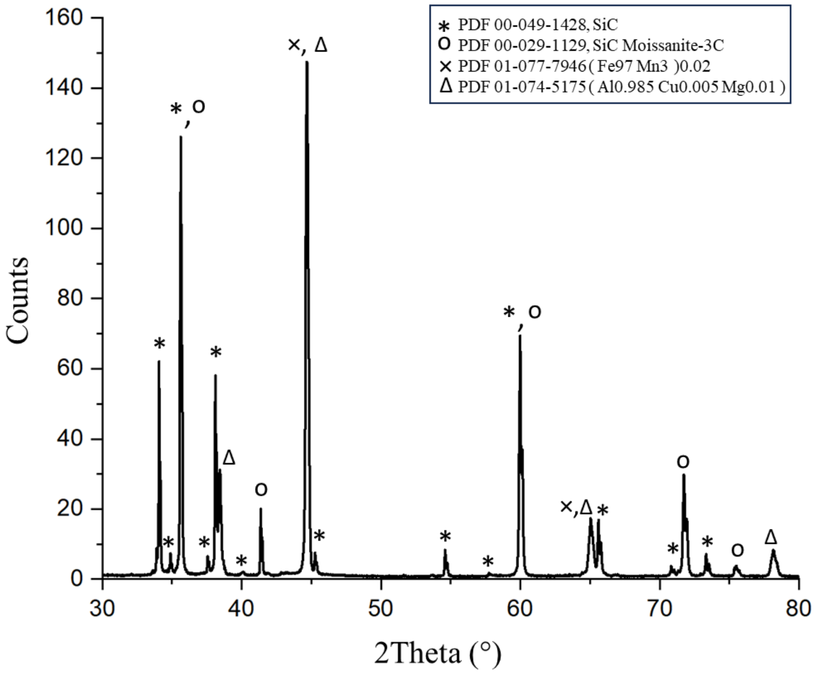

Figure 27. XRD Analysis of specimen 1.

When the XRD analysis of specimen 1 was examined, it can be seen that there are SiC peaks that come from the original SiC powder, and there are additional reflections coming from $(Fe_{97}Mn_3)_{0.02}$ and $Al_{197}CuMg_2$ intermetallics forming transient liquid phase alloying during pressure infiltration.

4.2.1.2 Microstructural Analysis

The cross-section of the hot preform squeeze infiltrated composite (specimen 1) was examined in the optical microscope. The resultant microstructure of the hot preform (1000 °C) squeeze cast infiltrated porous compact is shown in Figure 28 Figure 29. Pech-Canul et al. [24] mentioned that the Mg addition during melt infiltration improves the wetting of the Al on SiC, so in this study, during the squeeze casting, 2 wt% Mg was added to the Al melt and mixed. H. S. Lee and S. H. Hong [34] stated that to obtain complete infiltration, for a 70 vol% SiC preform with bimodal SiC particles, the required infiltration pressure was 50 MPa with the Al melt whose temperature is around 800 °C and the preheat temperature of the compact was 550 °C. For specimen 1, 1000 °C of preheat temperature and 100 MPa squeeze cast infiltration pressure were applied and when the specimens were examined all around, such as the infiltration region, center of the composite, and the outer region, it was seen that Al completely infiltrated and filled all the pores of the SiC compact. In addition, the composite has a similar microstructure in every region. It means that SiC particles are homogenously distributed to the matrix and there is not any defect like void or crack. As a result, by using these parameters and additions, hot preform squeeze casting was achieved successfully in terms of fulfilling the porosities and obtaining a defect-free structure.

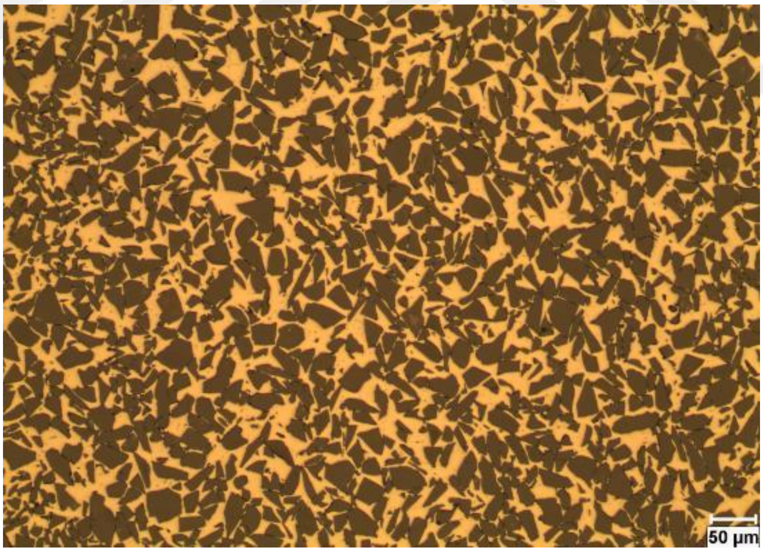

Figure 28. Microstructure of hot preform (1000 °C) squeeze cast Al-SiC composite.

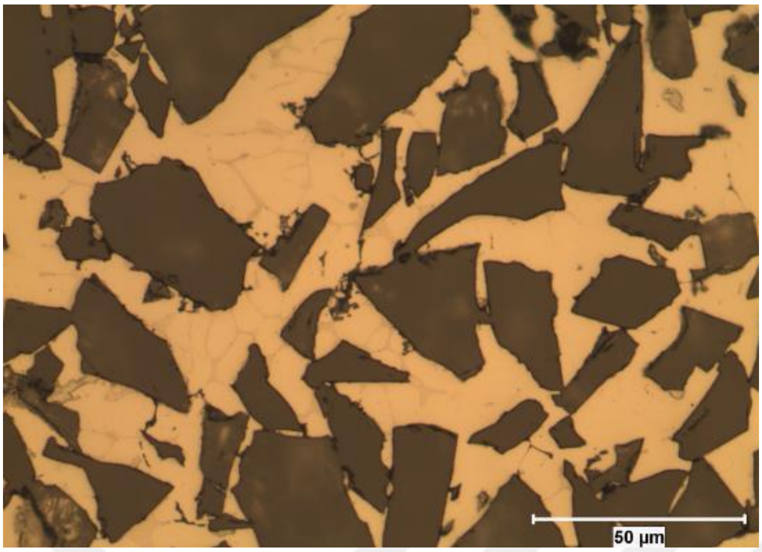

Figure 29. Microstructure of hot preform (1000 °C) squeeze cast Al-SiC composite.

4.2.1.3 Image Analyzer

Dewinter Materials Plus Image analyzer software was used and approximately the area % of the matrix and the reinforcement were determined quantitatively. The magnification used in the examination is X100. In the analysis, SiC particulates, whose color is red, have a different color from the matrix which is green as it is shown in Figure 30. This color difference is used to separate particulates and the matrix. The total area of SiC and matrix was calculated by the program and converted into vol%. The results of the image analysis are given in Table 9.

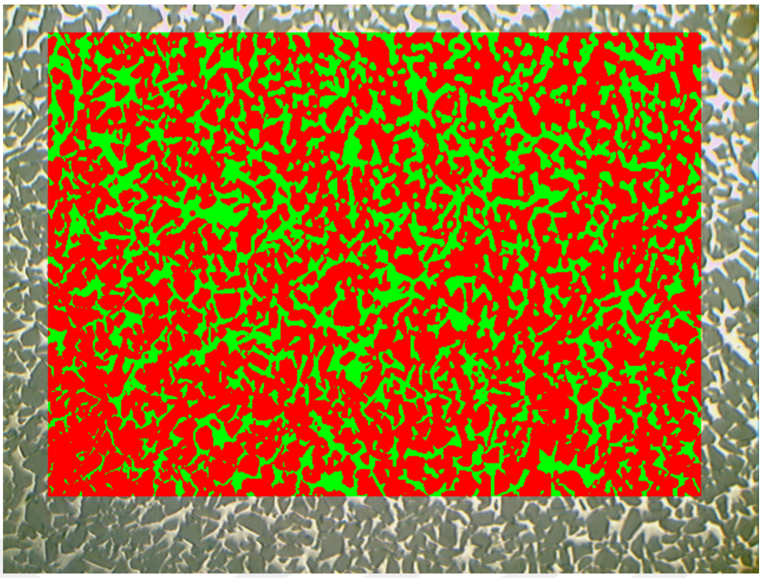

Figure 30. The image analysis of the hot preform (1000 °C) squeeze cast Al-SiC composite.

Table 9. The result of the image analysis of the hot preform (1000 °C) squeeze cast Al-SiC composite.

Phase Name	**Area (%)**
SiC	67.364
Al (Matrix)	32.636

4.2.1.4 EDS Analysis

The EDS analysis was conducted to the hot preform infiltrated specimen 1.

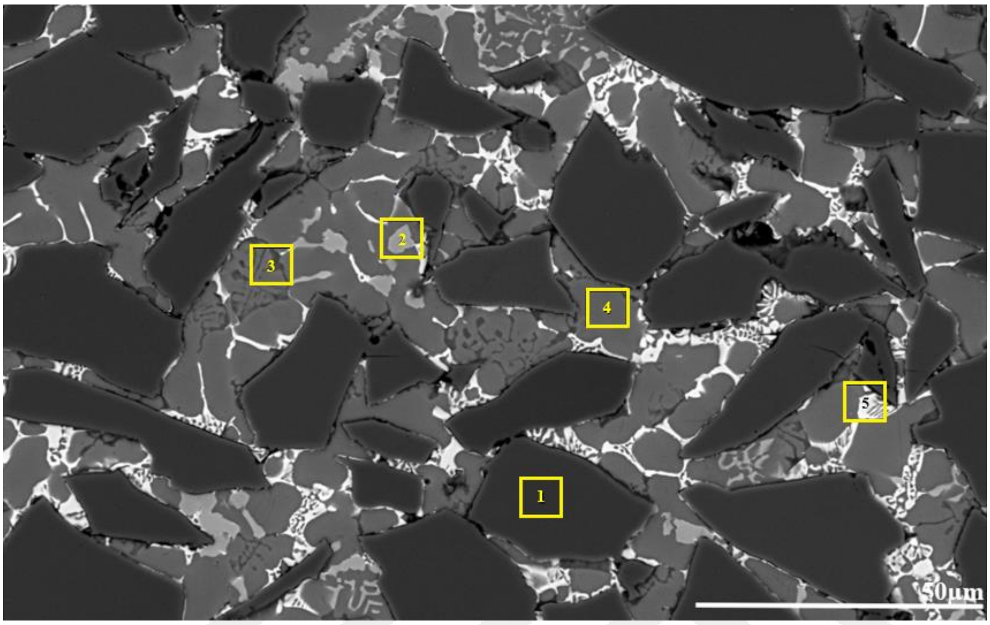

Figure 31. SEM image of the hot preform (1000 °C) squeeze cast Al-SiC composite.

The EDS point analysis of the hot preform (1000 °C) squeeze cast Al-SiC composite is shown in Figure 32Figure 33Figure 34Figure 35 Figure 36 where the points that were conducted to the EDS analysis are shown in Figure 31. Point 1 is a SiC particle whose only Si peak can be seen in Figure 32.

Point 2 was taken from the AlFeMnSi intermetallic as result of segregation. The peaks of Al, Fe, Si, and Mn can be seen in Figure 33. Al, Fe, Mn, and Si peaks have the highest intensities. According to Warmuzek [40], the formation of AlFeMnSi precipitates during finite cooling rates is determined by a competition between crystal lattice ordering and crystal growth rates. Typically, in slowly cooled alloys, faceted polyhedral of the α_c-AlFeMnSi phase forms. The transformation of the primary AlFeMnSi precipitates from polyhedral to dendritic shapes is affected by the cooling rate but also, mainly by the content of transition metals, particularly the Fe/Mn ratio. In slowly cooled liquid AlFeMnSi alloys, both primary crystals of α_H-

AlFeSi and α_c-AlFeMnSi phases form with a faceted polyhedral shape, determined by local preferences for crystallographic plane growth. Conversely, in rapidly cooled alloys, the precipitates form with a dendritic shape, showing that the morphology of the growth front changed. In Figure 31, both the Chinese script morphology and primary crystal forms of the AlFeMnSi or AlFeSi precipitates form in the structure.

Point 3 is the Mg_2Si phase (Chinese script). In the structure, there are also small globular Mg_2Si precipitates formed at the interior and the vicinity of Al grains. The peaks of Al, Mg, Si, Cu, and Zn can be seen in Figure 34. The Al, Mg, and Si peaks have the highest intensities. According to Meng et al. [41], the segregation that occurred in the Al6061 alloy is related to the cooling rate of the solidification. Slower cooling leads to the easier formation of segregations. Additionally, Mavros et al. [42] state that the elevated Mg (>3 wt%) contents in an Al-Si alloy contribute to the development of the Mg_2Si intermetallic phase within the alloy matrix. The generation of Mg_2Si phase formation involves the following steps:

(a) The initiation of solidification below the liquidus results in the formation of primary α-Al.

(b) Continuing solidification below the pseudo eutectic point leads to the emergence of primary Mg_2Si crystallites at the periphery of the primary α-Al.

(c) Solidification persists at the eutectic temperature, resulting in the formation of the eutectic microconstituent $AlMg_2Si$, characterized by Chinese script morphology.

(d) Finally, solidification is finished with the eutectic Al-Si reaction.

Since the preform temperature of 1000 °C was used before the infiltration, it resulted in a slower cooling during and after the squeeze cast infiltration and there was a time at high temperatures to form this kind of precipitation, so Mg_2Si phases formed in the structure.

Point 4 shown in Figure 35 is the α-Al which has the peaks of Al, Zn, Cu, and Mg which have been added during the melting of the Al. This α-Al is similar to the α-Al where the Nicom and Nomura [43] were found in their specimen’s structure after the pressure infiltration of porous SiC. This point analysis corresponds to the original Al6061 chemical composition.

Point 5 is the eutectic Al-Mg-Zn-Cu structure which has the clear peaks of Al, Mg, Zn, and Cu shown in Figure 36. Fan et al. [44] also find a similar eutectic structure in as cast condition. Solute redistribution during solidification results in micro segregation and the development of large intermetallic particles. Within the Al-Zn-Mg-Cu system, there is a specific composition range where a eutectic reaction takes place during solidification. This reaction involves the transformation of the liquid phase into a combination of α-Al solid solution and a eutectic phase, composed of intermetallic compounds and potentially other phases relying on the composition.

Furthermore, in squeeze casting, rapid solidification occurs because of the high applied pressure and the process is carried out under an open atmosphere. This accelerated solidification plays a vital role in favoring the formation of a refined and uniform microstructure, including the eutectic structure. By limiting the growth of primary dendrites, this rapid solidification permits the formation of a finer eutectic microstructure.

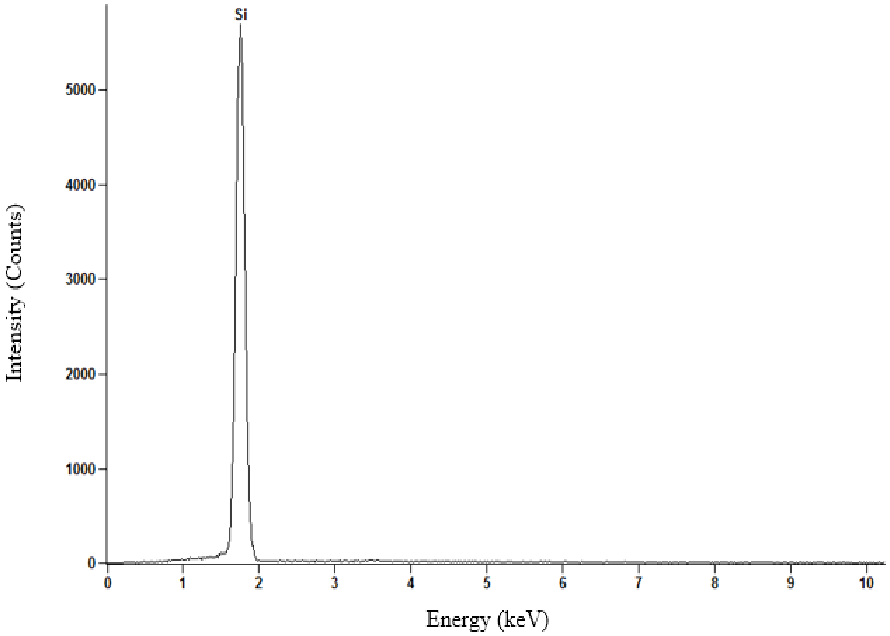

Figure 32. EDS Analysis of Point 1 is shown in Figure 31.

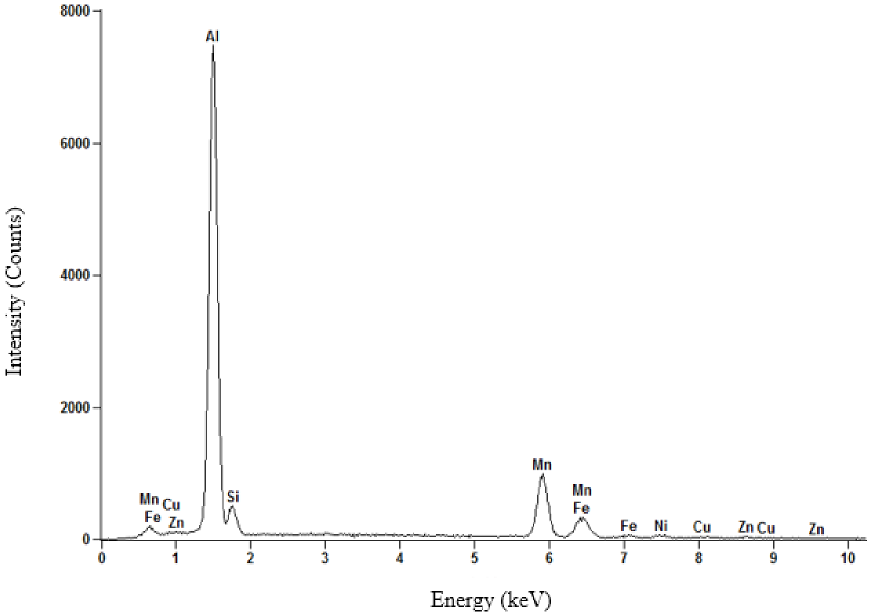

Figure 33. EDS Analysis of Point 2 is shown in Figure 31.

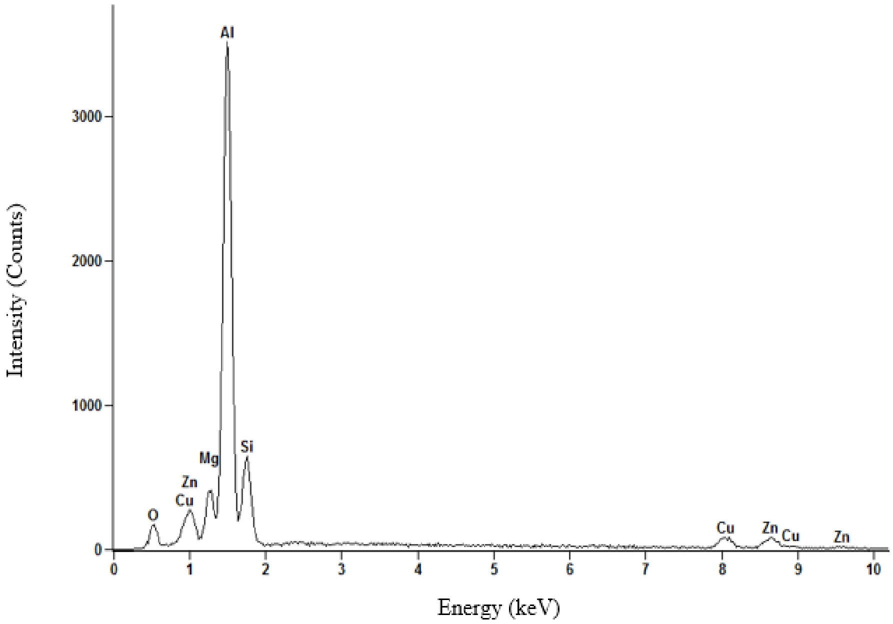

Figure 34. EDS Analysis of Point 3 is shown in Figure 31.

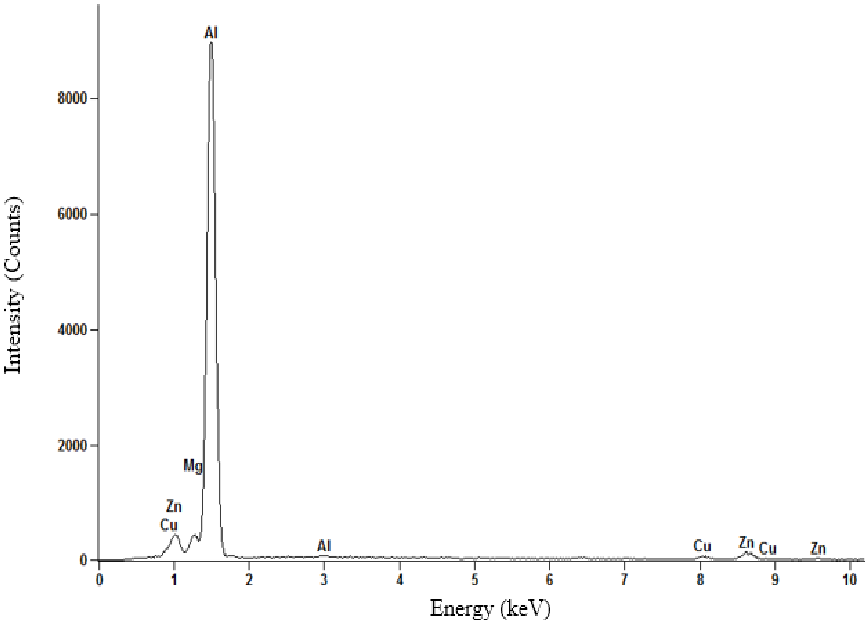

Figure 35. EDS Analysis of Point 4 is shown in Figure 31.

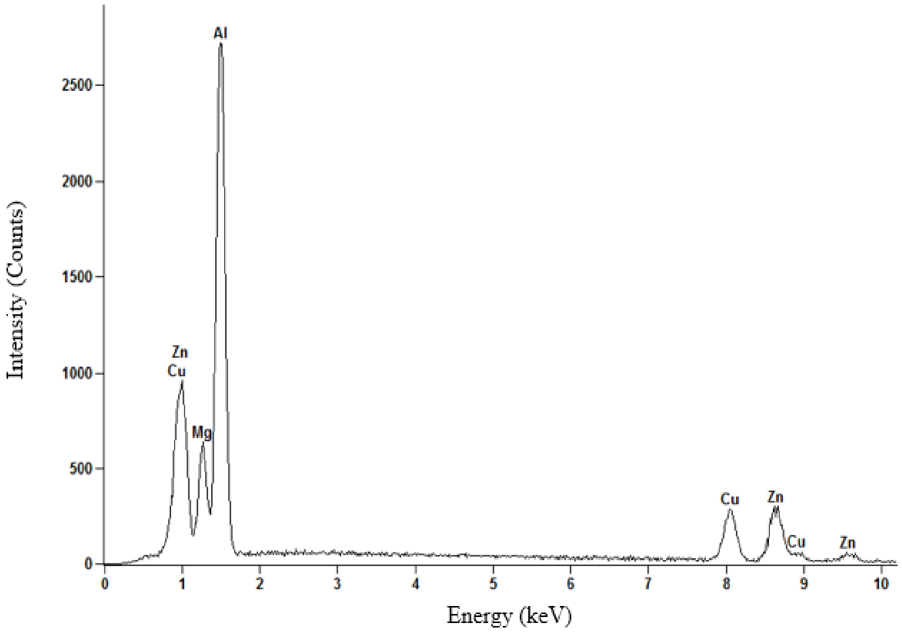

Figure 36. EDS Analysis of Point 5 is shown in Figure 31.

4.2.2 Hot Preform Squeeze Casting Infiltration of SiC – Al Compact

Hot preform infiltrated specimens were characterized by XRD, SEM, EDS, optical microscopy, and image analyzer software programs.

4.2.2.1 XRD Analysis

XRD analysis of the hot preform infiltrated specimen 2 was given below.

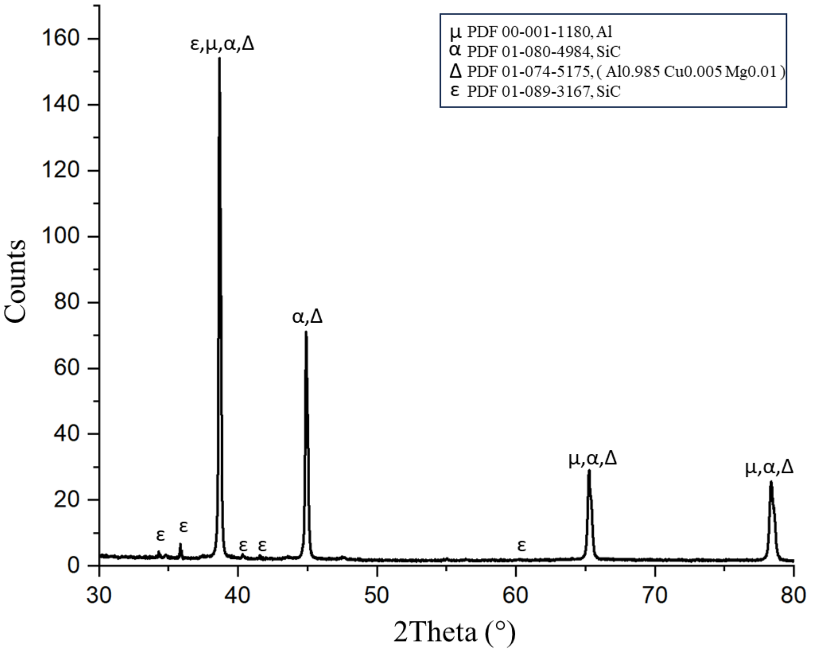

Figure 37. XRD Analysis of specimen 2.

When the XRD analysis of specimen 2 was examined, it can be seen that there are SiC peaks that come from the original SiC powder, and there are additional reflections coming from α-Al and $Al_{197}CuMg_2$ intermetallics forming transient liquid phase alloying during pressure infiltration.

4.2.2.2 Microstructural Analysis

The cross-section of the hot preform squeeze infiltrated composite (specimen 2) was examined in the optical microscope. The resultant microstructure of the hot preform (800 °C) squeeze cast infiltrated porous compact is shown in Figure 38. The same principles of specimen 1 were applied in terms of preheated die temperature and squeeze cast pressure.

When the specimens were examined by cutting specimens from various sections, such as the infiltration region, center of the composite, and the outer region, it was seen that Al completely infiltrated and filled all the pores of the SiC compact as it was expected with respect to the specimen 1. It was revealed that SiC particles are homogenously distributed in the matrix and there is not any defect like void or crack. However, most of the Al particles added to the SiC powder did not melt completely during melt infiltration, but grain shape accommodation was observed because of transient liquid under high pressure and surface transport events taking place on the surface of Al powders (Curvature coarsening of powders).

Although the melting point of the Al particles exceeded during preheating, the waiting time at 800 °C was not enough to make all the Al particles closer to the melting point. Consequently, they could not melt in the infiltrated Al since the cooling rate during and after the squeeze casting is fast. The microstructure appearance is shown in Figure 39. There are very rare regions where these Al particles are close to melting and form branches with the infiltrated Al to improve infiltration as shown in Figure 40. In this region, due to the high temperature of the pressurized liquid during infiltration, powder boundaries transformed into grain boundaries.

Before the squeeze casting, Reihani [8] initially preheated the mold and SiC preform to 300 °C and poured the molten Al6061 alloy into the mold at 800 °C. After that, 100 MPa pressure was applied to the mixture using a hydraulic press. The molten Al alloy was therefore infiltrated into the preheated reinforcement preform and solidified. A uniform distribution of the second-phase particles is revealed in the matrix phase. Furthermore, small amounts of pores were observed in the microstructure, showing that the infiltration of Al alloy was almost complete. For specimen 2, the preform was heated to 800 °C. Similar to Reihani [8]'s work, the die was preheated to 300 °C, and 100 MPa pressure was applied during squeeze casting. As a result, filled and uniformly distributed second phases were obtained in the final structure.

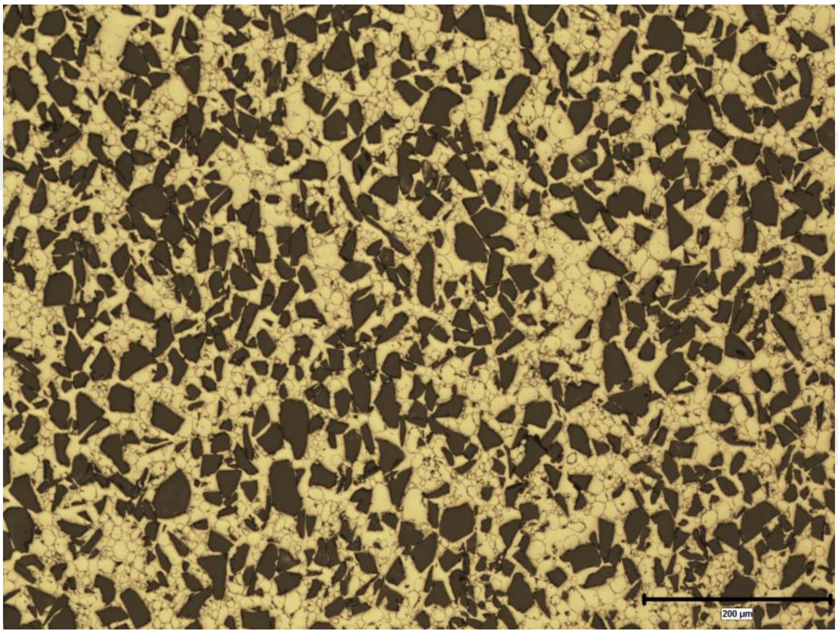

Figure 38. Microstructure of hot preform (800 °C) squeeze cast Al-SiC composite.

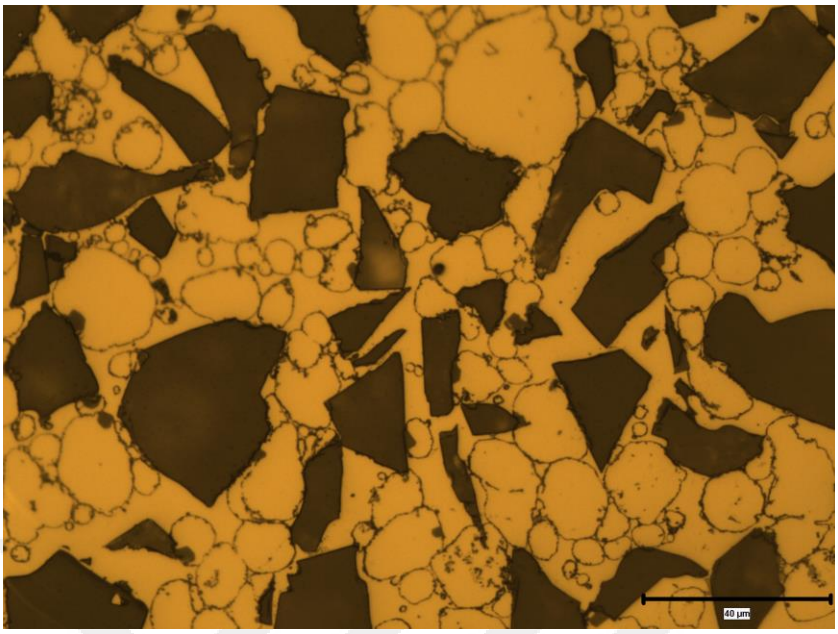

Figure 39. Microstructure of hot preform (800 °C) squeeze cast Al-SiC composite.

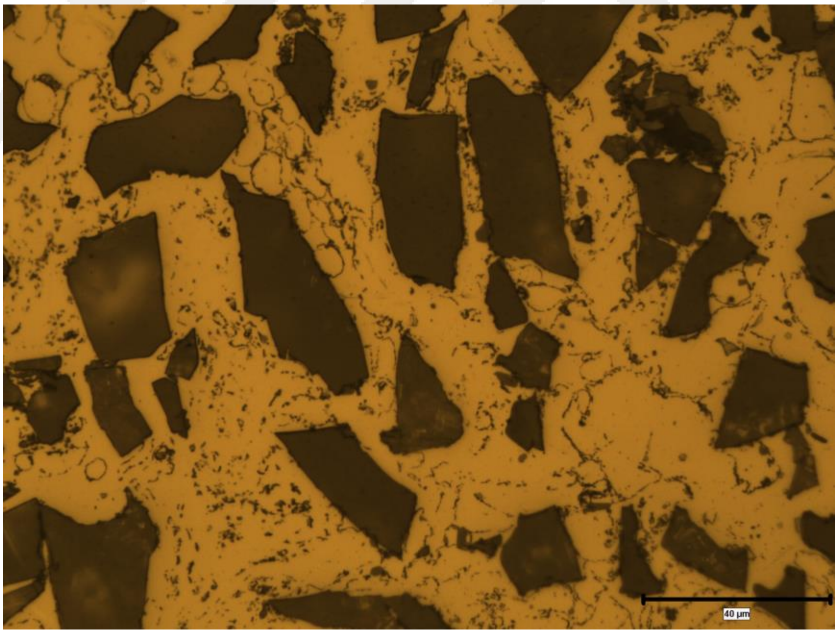

Figure 40. Microstructure of hot preform (800 °C) squeeze cast Al-SiC composite.

4.2.2.3 Image Analyzer

Dewinter Materials Plus Image analyzer software was used and approximately the area % of the matrix and the reinforcement were determined quantitatively. The magnification used in the examination is X100. In the analysis, SiC particulates, whose color is red, have a different color from the matrix which is green as it is shown in Figure 41. This color difference is used to separate particulates and the matrix. The total area of SiC and matrix was calculated by the program and converted into vol%. The results of the image analysis are given in Table 10.

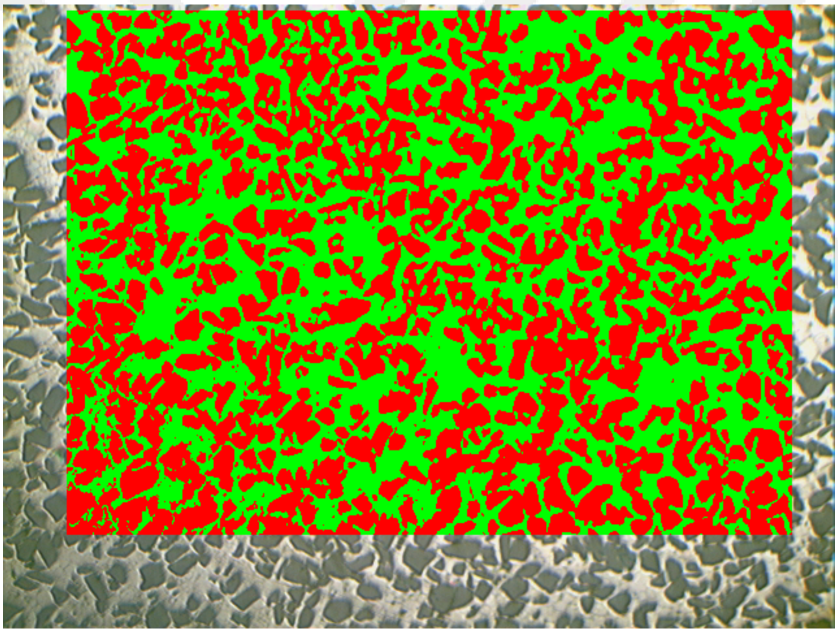

Figure 41. The image analysis of the hot preform (800 °C) squeeze cast Al-SiC composite.

Table 10. The result of the image analysis of the hot preform (800 °C) squeeze cast Al-SiC composite.

Phase Name	**Area (%)**
SiC	51.95
Al (Matrix)	48.05

4.2.2.4 EDS Analysis

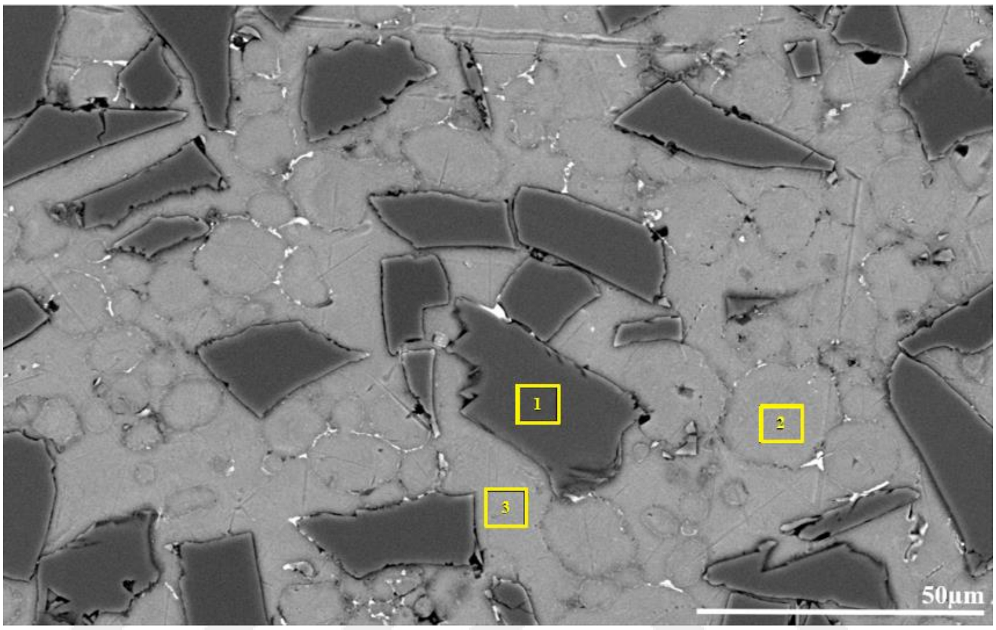

Figure 42. SEM image of the hot preform (800 °C) squeeze cast Al-SiC composite.

The EDS point analysis of the hot preform (800 °C) squeeze cast Al-SiC composite. The points that were conducted in the EDS analysis are shown in Figure 42. Point 1 is a SiC particle whose only Si peak can be seen in Figure 43. Point 2 is the pure Al particle which was added during powder preparation. The boundaries of the particle still can be seen in Figure 42 because it could not completely mix into the cast Al6061. Zn and Al peaks of the particle can be seen in Figure 44. which indicates that there was a diffusion of Zn atoms from the squeeze cast Al to the pure added Al particles during squeeze casting. However, they could not form a complete mixture since the cooling rate in squeeze casting is very high and there was not enough time to form a complete uniform mixture. Point 3 is the α-Al whose Al, Zn, and Cu peaks can be seen in Figure 45.

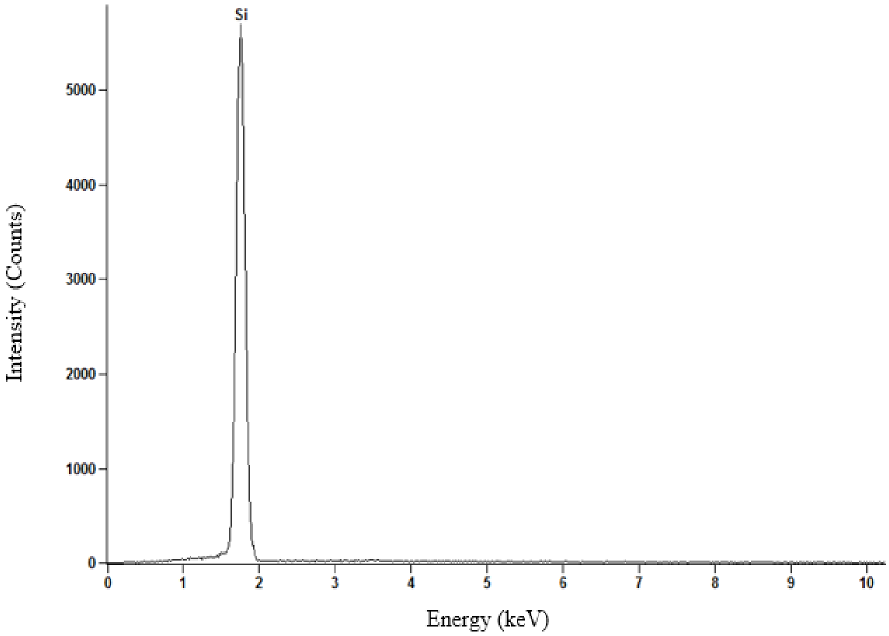

Figure 43. EDS Analysis of Point 1 is shown in Figure 42.

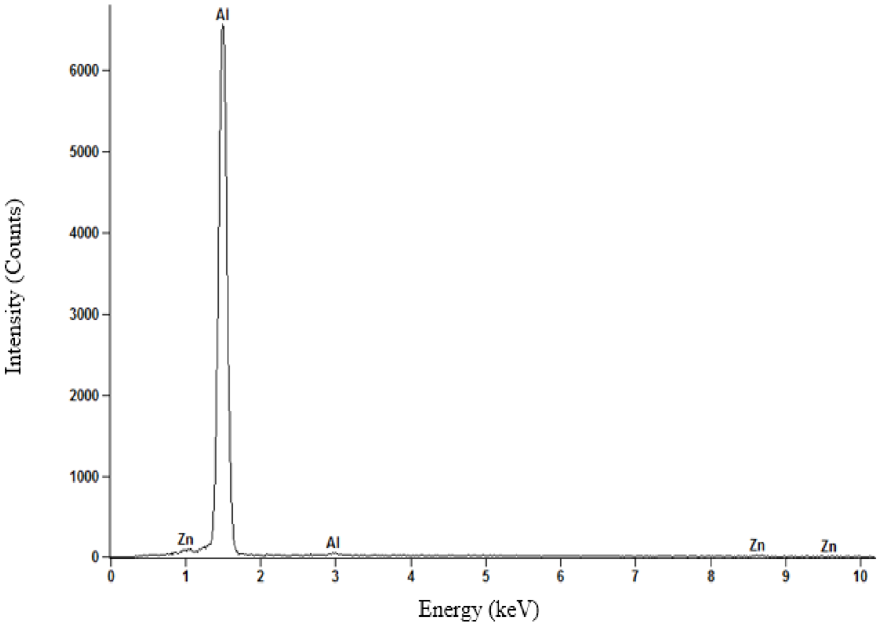

Figure 44. EDS Analysis of Point 2 is shown in Figure 42.

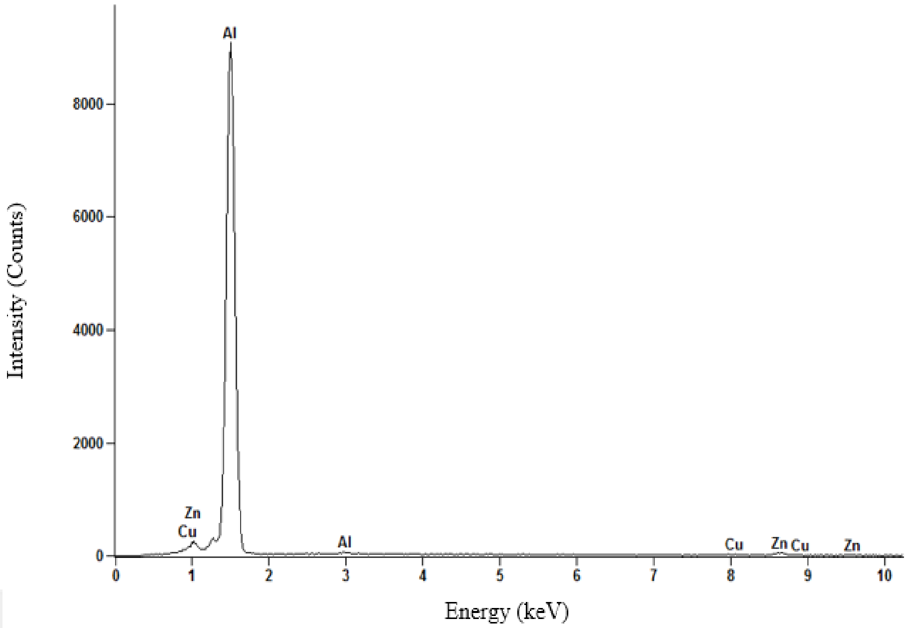

Figure 45. EDS Analysis of Point 3 is shown in Figure 42.

4.2.3 Cold Preform Squeeze Casting Infiltration of SiC- Al Compact

Cold preform infiltrated specimens were characterized by XRD, SEM, EDS, Optical microscopy, and image analyzer software programs.

4.2.3.1 XRD Analysis

XRD analysis of the cold preform infiltrated specimen 3 was given below.

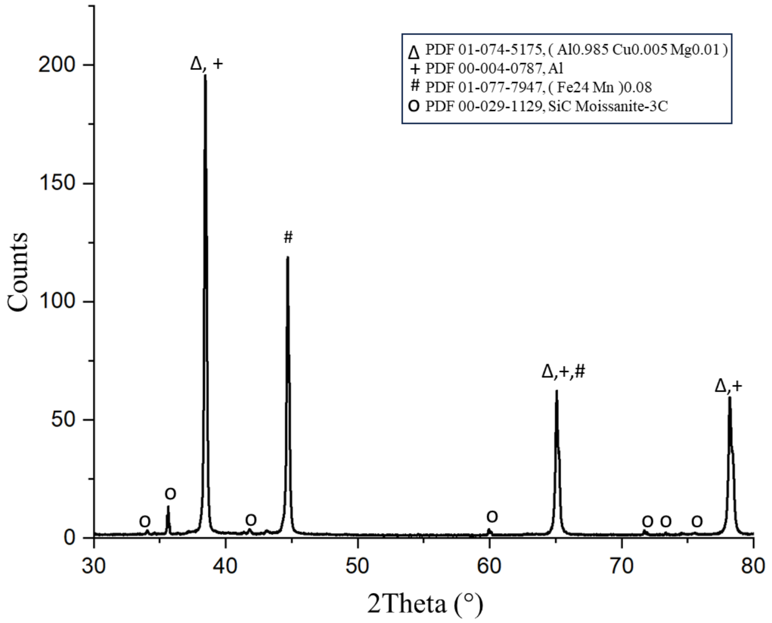

Figure 46. XRD Analysis of the specimen 3.

When the XRD analysis of specimen 1 was examined, it can be seen that there are SiC peaks that come from the original SiC powder, and there are additional reflections coming from α-Al, $(Fe_{24}Mn)_{0.08}$ and $Al_{197}CuMg_2$ intermetallics forming transient liquid phase alloying during pressure infiltration.

4.2.3.2 Microstructural Analysis

The cross-section of the composite was examined in the optical microscope. The resultant microstructure of cold preform squeeze cast infiltrated composite (specimen 3) is shown in Figure 47. When the specimens were examined all around, such as the infiltration region, center of the composite, and the outer region, it was seen that SiC particles homogenously distributed to the matrix, but Al melt could not completely infiltrate and fill all the porosities. There are remaining porosities inside the composite compact especially in the outer region of the composite. Squeeze-infiltrated Al could not completely wet the SiC particles in all the cross-section areas due to the very rapid cooling since the preform was cold.

When the infiltration region, central region, and outer region respectively shown in Figure 47Figure 48, Figure 50, and Figure 51,Figure 52 were examined individually, it shows that all the porosities in the infiltration region were filled with Al, but there are remaining pores and tears of the SiC particles in the central and the outer region of the cross-section area. The tear of the SiC particles probably occurred during the grinding and polishing because of the porosities near to these particles, since the infiltrated Al could not wet and adhere to these SiC particles. The transition zone between the area where all the porosity is filled with Al and the area where the structure has remained porosities can be seen in Figure 49.

The infiltrated Al could not fill all the porosities inside the ceramic compact. The reason is that during the squeeze casting, the molten Al starts to infiltrate with the capillary effect and the effect of the pressure of the hydraulic press, but the ceramic compact was at RT, and the Al which was infiltrating started to cool too rapidly. Consequently, the infiltrating Al could not fill all the porosities near and far from the infiltration region since it solidified rapidly.

In addition, since the composite specimen was vacuum sintered at 600 °C around 1.5 h, the majority of the pure Al particles diffuse and form branches with the infiltrated Al which leads to enhancement of the infiltration. These Al powder boundaries disappeared and transformed into grain boundaries, but small amounts of the powder started to diffuse and grow with the temperature, but their boundaries still can be seen, so they could not completely mix with the matrix.

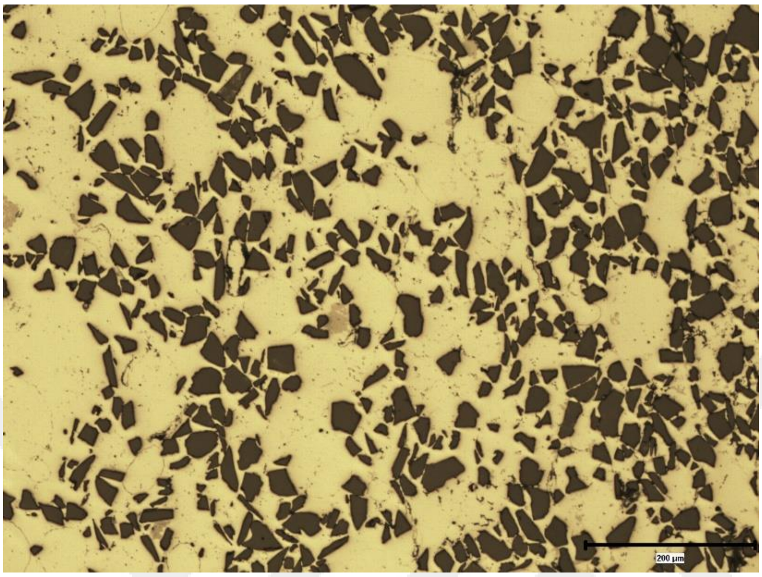

Figure 47. Infiltration region microstructure of cold preform squeeze cast Al-SiC composite.

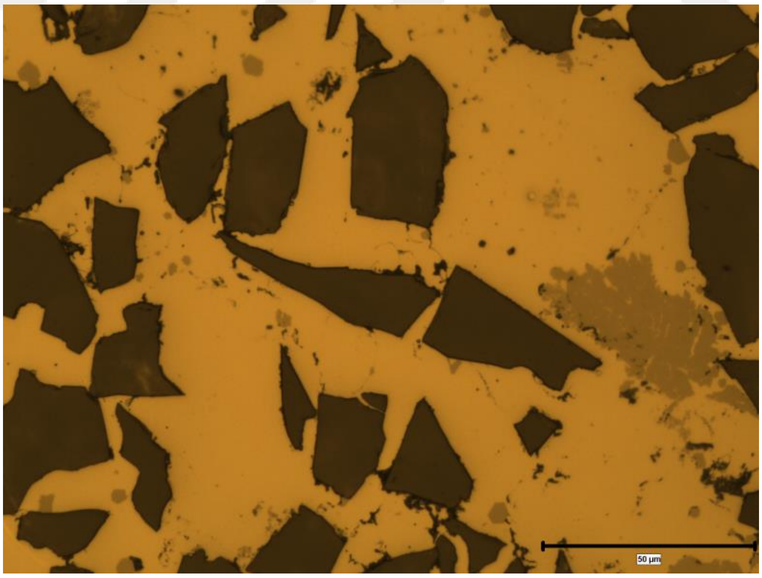

Figure 48. Infiltration region microstructure of cold preform squeeze cast Al-SiC composite.

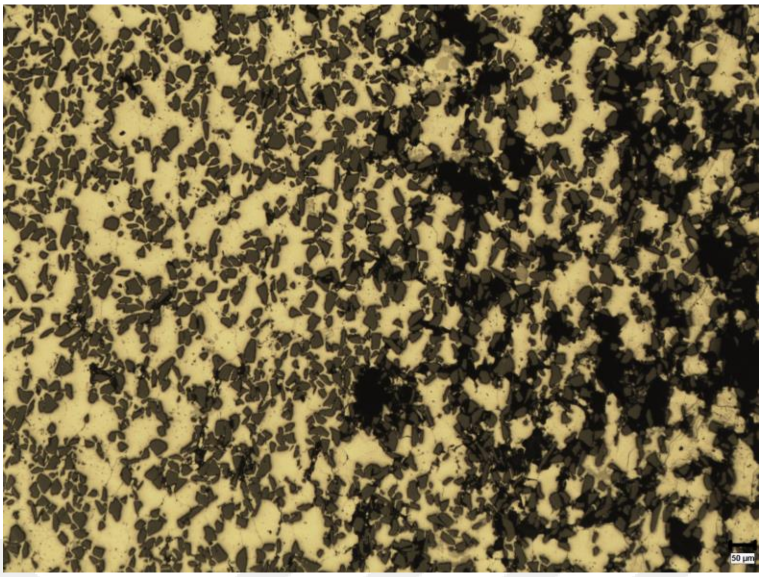

Figure 49. Microstructure of the transition zone from the infiltration region to the central region of the cold preform squeeze cast Al-SiC composite.

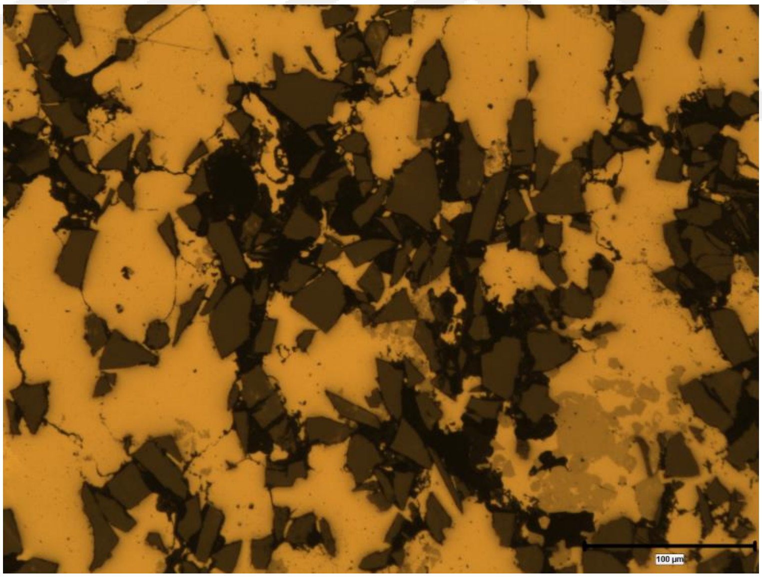

Figure 50. The central region microstructure of cold preform squeeze cast Al-SiC composite.

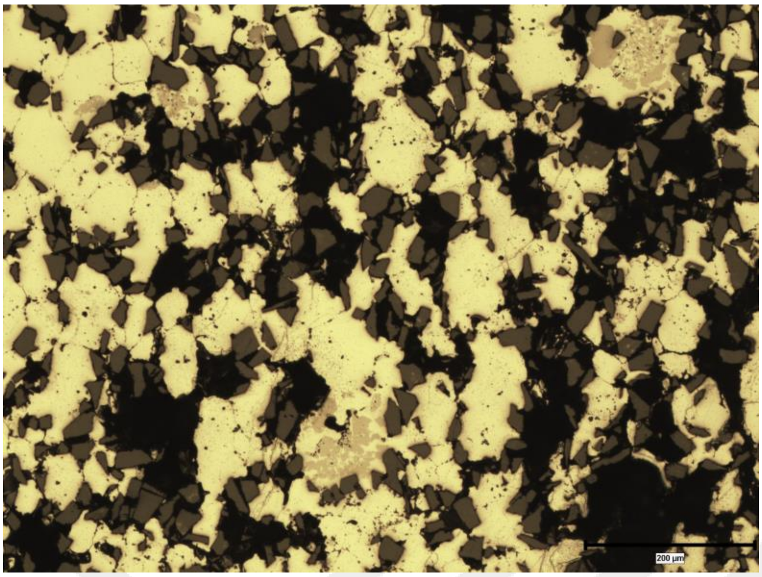

Figure 51. The outer region microstructure of cold preform squeeze cast Al-SiC composite.

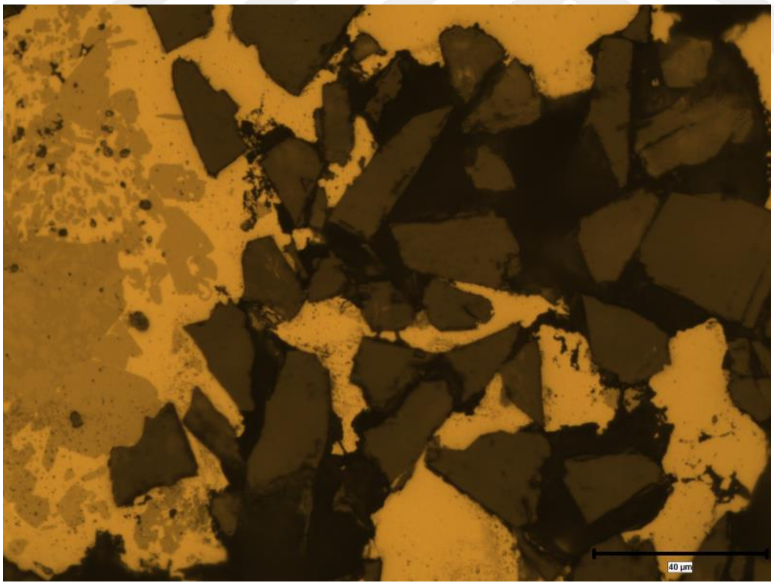

Figure 52. The outer region microstructure of cold preform squeeze cast Al-SiC composite.

4.2.3.3 Image Analyzer

Dewinter Materials Plus Image analyzer software was used and approximately the area % of the matrix and the reinforcement were determined quantitatively. The magnification used in the examination is X100. In the analysis, SiC particulates, whose color is red, have a different color from the matrix which is green as it is shown in Figure 53. This color difference is used to separate particulates and the matrix. The total area of SiC and matrix was calculated by the program and converted into vol%. The results of the image analysis are given in Table 11.

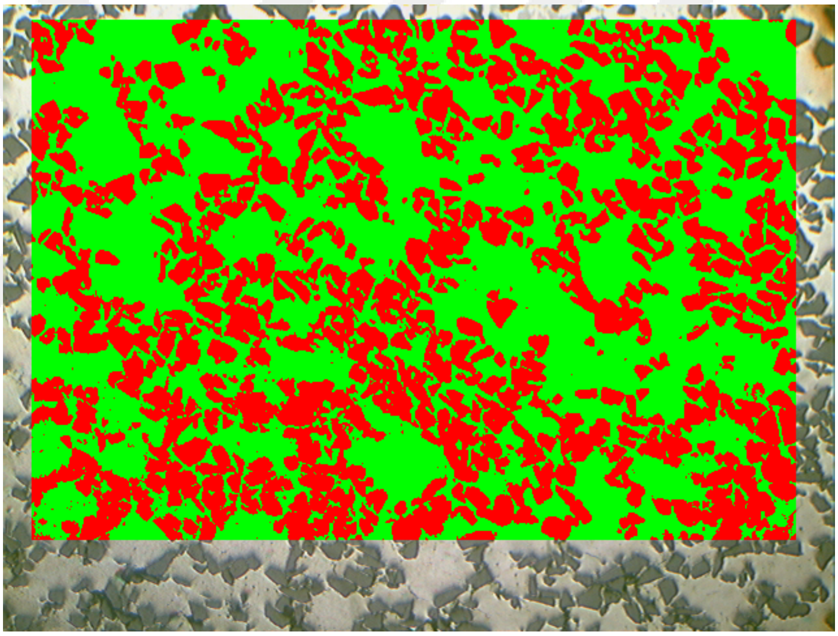

Figure 53. The image analysis of the cold preform squeeze cast Al-SiC composite.

Table 11. The result of the image analysis of the cold preform squeeze cast Al-SiC composite.

Phase Name	**Area (%)**
SiC	43.68
Al (Matrix)	56.32

4.2.3.4 EDS Analysis

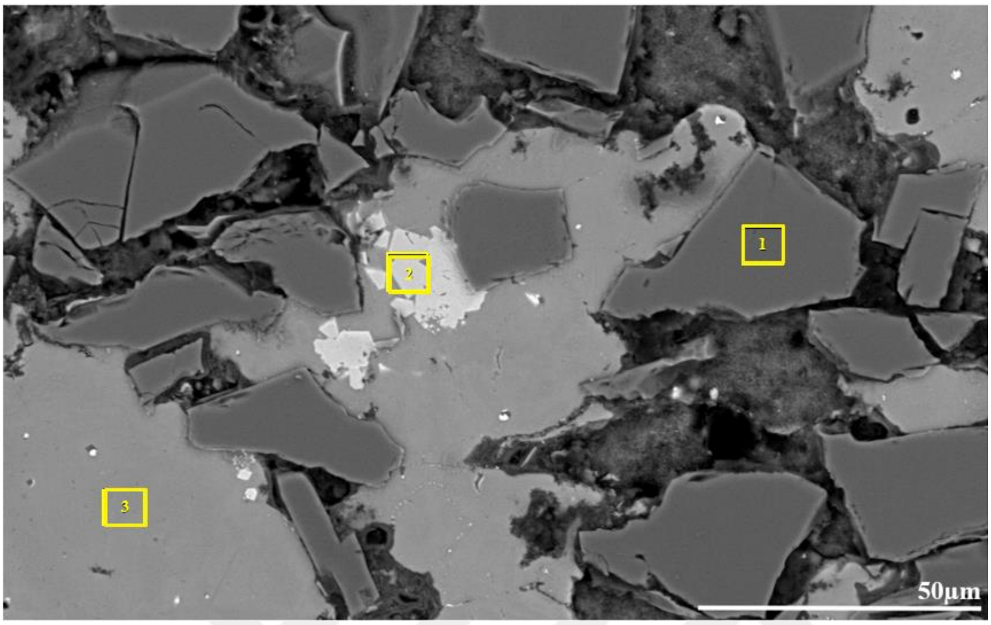

Figure 54. SEM image of cold preform squeeze cast Al-SiC composite.

The EDS point analysis of the cold preform squeeze cast Al-SiC composite is shown in Figure 55Figure 56Figure 57. The points that were conducted to the EDS analysis are shown in Figure 54. Point 1 is a SiC particle whose only Si peak can be seen in Figure 55.

Point 2 was taken from the AlFeMnSiCr intermetallic. The peaks of Al, Fe, Mn, Si, Cu, Zn, and Cr can be seen in Figure 56.

Shabestari's [44] work indicated that the segregation of these intermetallic compounds is not favorable when the levels of iron, manganese, and chromium are low. The experiments demonstrated that in an Al alloy with a content of 0.4 wt% Fe and 0.1wt% Cr, the formation of iron platelets (Beta phase) and star-like intermetallic did not happen if the manganese concentration was below 0.3 wt%. In another Al alloy containing 0.8 wt% Fe and 0.1 wt% Cr, the star-like compounds formed within the range of 0.1 to 0.3 wt% Mn and their quantity increased with higher manganese content. Star-like compounds develop at elevated manganese concentrations (Mn> 0.3 wt%) in alloys involving 0.4 wt% Fe and a segregation factor higher than 1.30. However, the study revealed that in alloys with a content of 0.8 wt% Fe, star-like intermetallic developed at lower manganese concentrations (0.1 wt% Mn) while keeping the same segregation factor (SF > 1.30).

As a result, since the Mn and Fe have the highest intensities as shown in Figure 56, the intermetallic that is present in specimen 3's microstructure is some type of star-like compound formed during the sintering stage. In addition, after the sintering process was applied to specimen 3 it was slowly cooled in the furnace, so it allowed them to grow to the larger intermetallic phases as can be seen in Figure 52.

Point 3 is taken from the α-Al region which is similar to the α-Al region seen in the final structure of Nicom and Nomura's [43] study after the pressure infiltration. The peaks of Al, Cu, and Zn can be seen in Figure 57.

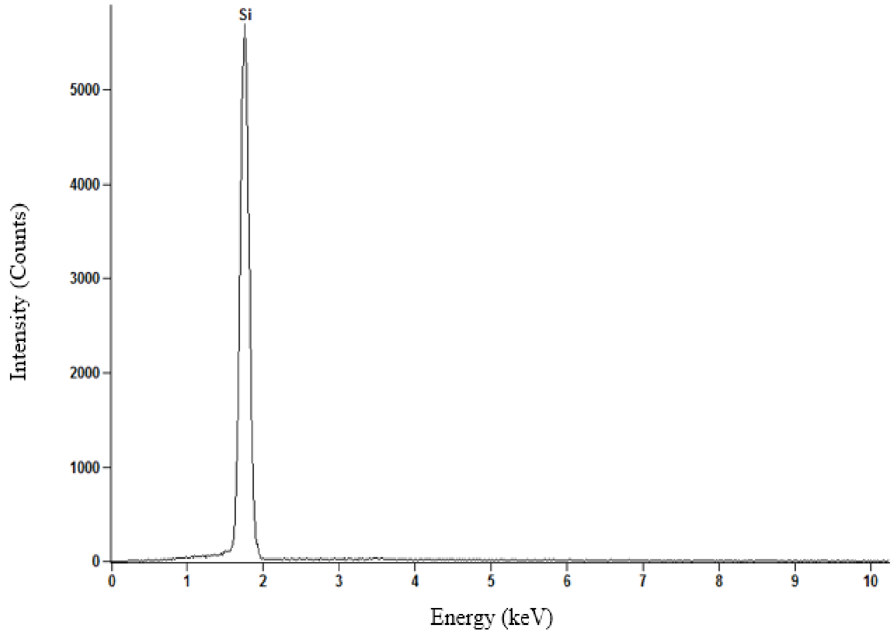

Figure 55. EDS Analysis of Point 1 is shown in Figure 54.

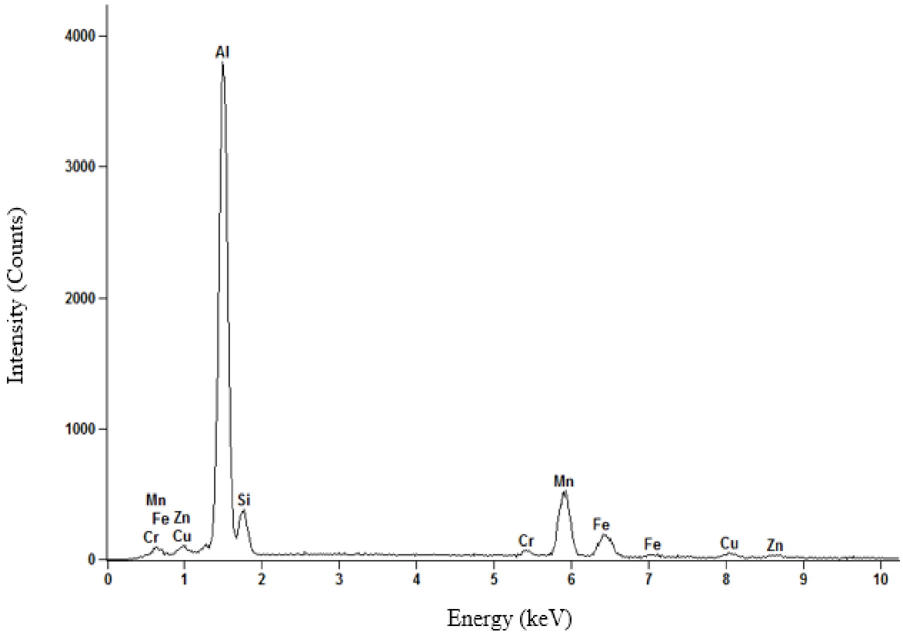

Figure 56. EDS Analysis of Point 2 is shown in Figure 54.

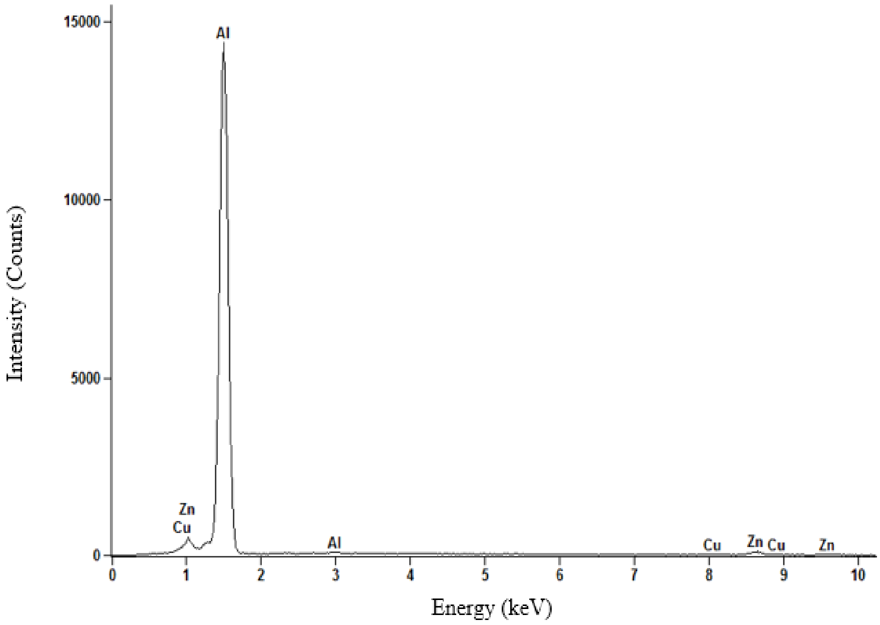

Figure 57. EDS Analysis of Point 3 is shown in Figure 54.

4.3 Mechanical Characterization of Specimens

4.3.1 Hardness Test Results

Hardness tests were conducted on specimens 1,2 and 3 according to the ASTM-E10. Eight measurements were taken from the samples and the highest-lowest values were discarded, then the results were averaged. The numerical results are given in Table 12Table 13. The hardness tests were carried out by using the HBW 2.5/62.5. The ball diameter used in the test is 2.5mm and 62.5 kgf was applied to the specimen.

Table 12. Hardness values of the squeeze cast Al and specimens 1 and 2.

Measurement No	**Hardness Values (HBW 2.5/62.5)**		
	Squeeze Cast Al	**Specimen 1**	**Specimen 2**
1	68	220	142
2	72	221	146
3	70	225	150
4	74	230	144
5	73	222	147
6	71	227	143
Average	71.33	224.17	145.33
Standard Dev.	1.97	3.53	2.69

Table 13. Hardness values of the regions of the specimen 3.

Measurement No	**Hardness Values (HBW 2.5/62.5)**		
	Specimen 3 Infiltration Region	**Specimen 3 Outer Region**	**Specimen 3 Al Region**
1	150	65	91
2	160	57	95
3	151	59	94
4	157	54	90
5	155	62	97
6	158	58	92
Average	155.17	59.17	93.17
Standard Dev.	3.62	3.53	2.41

For specimens 1 and 2, composite regions exhibit higher hardness than the squeeze cast Al region. The average hardness value of the squeeze cast Al is 71.33 and the distribution is shown in Figure 58. Specimen 1 exhibits the highest hardness values among the three specimens and the average hardness of specimen 1 is 224.17. The distribution of the hardness values is shown in Figure 59. Since specimen 1 was produced with hot preform squeeze casting which leads to uniform structure, and involves the highest vol% of SiC, it was expected to achieve the highest hardness compared to specimens 2 and 3.

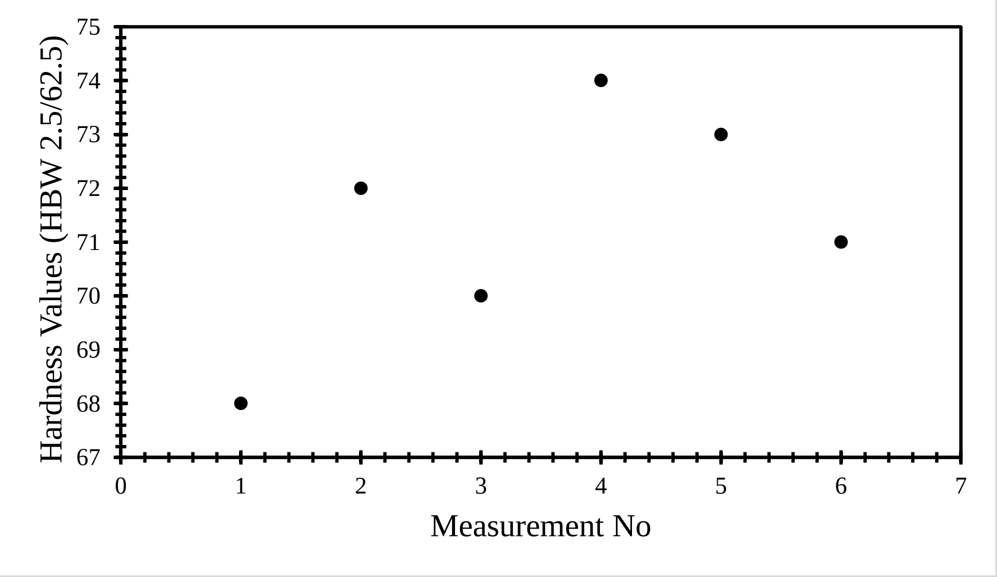

Figure 58. Hardness distribution of the squeeze cast Al.

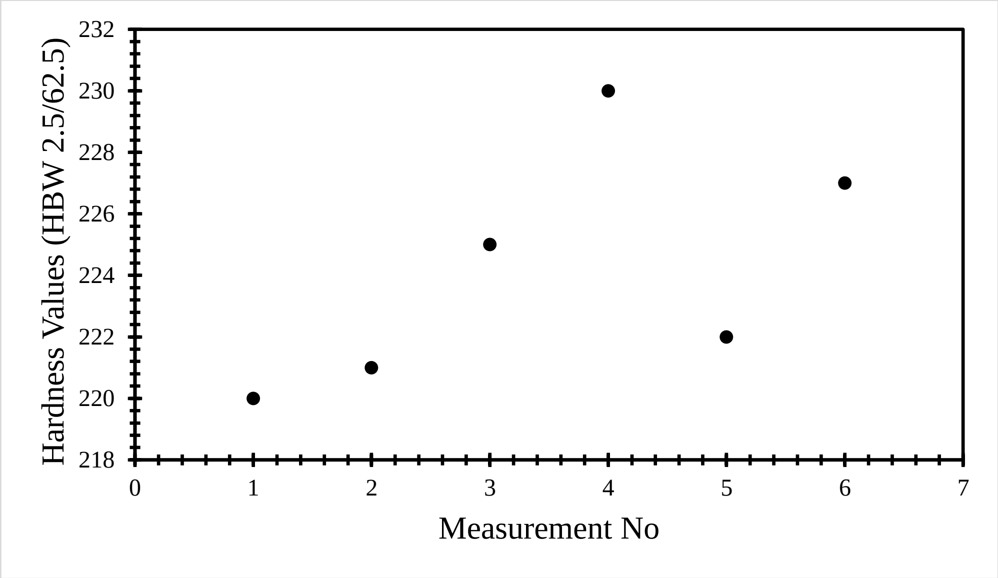

Figure 59. Hardness distribution of the specimen 1.

When specimen 2 is investigated, it could be seen that the average hardness value is around 145.33 and it is much higher than the squeeze cast Al. The distribution of the hardness values is shown in Figure 60. Although both specimens 1 and 2 were produced with hot preform squeeze casting, the vol% of SiC in specimen 2 is lower than the specimen 1, and specimen 2 involves pure Al powder in the structure which weakens the overall hardness in the Al matrix since the hardness of the Al6061 is higher than the pure Al powder, so its hardness values are less than the specimen 1 which was expected.

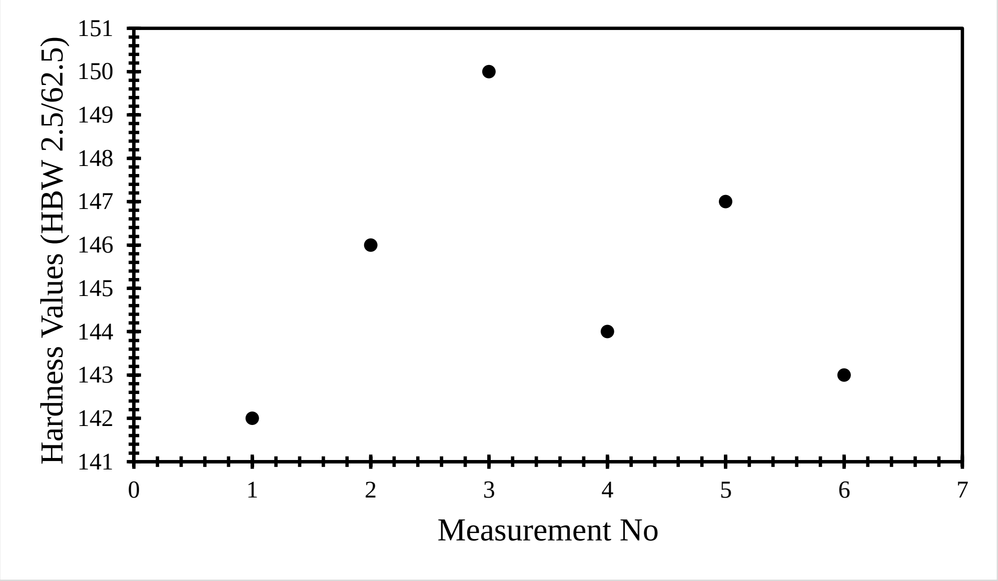

Figure 60. Hardness distribution of specimen 2.

When specimen 3 is investigated, it shows different hardness values in different regions since it is produced with cold preform squeeze casting, then sintering process, and the resultant microstructure of the specimen is not uniform. The distribution of the hardness values is shown in Figure 61, Figure 62Figure 63.

The hardness values of the squeeze cast Al of specimen 3 are higher than specimens 1 and 2 because of the after-sintering process applied to specimen 3. The average hardness value squeezed cast Al of specimen 3 is 93.17. In the infiltration region of specimen 3, the average hardness value is around 155 which is higher than specimen 2 even though the vol% of SiC in specimen 3 is less than specimen 2. The reason is that specimen 3 was exposed to the sintering process after infiltration which improves the hardness of the Al matrix by around 30%, so the support of the Al matrix is much more than specimen 2. Also, specimen 2 involves soft pure Al particles inside the matrix.

Consequently, the infiltration region of specimen 3 exhibits a higher average hardness value than specimen 2. However, in the outer region of specimen 3, the infiltration could not be achieved properly and there are porosities inside the structure. As a result, the average hardness value of the outer region of specimen 3 is 59.17 which is the lowest highest hardness value among all the measurements.

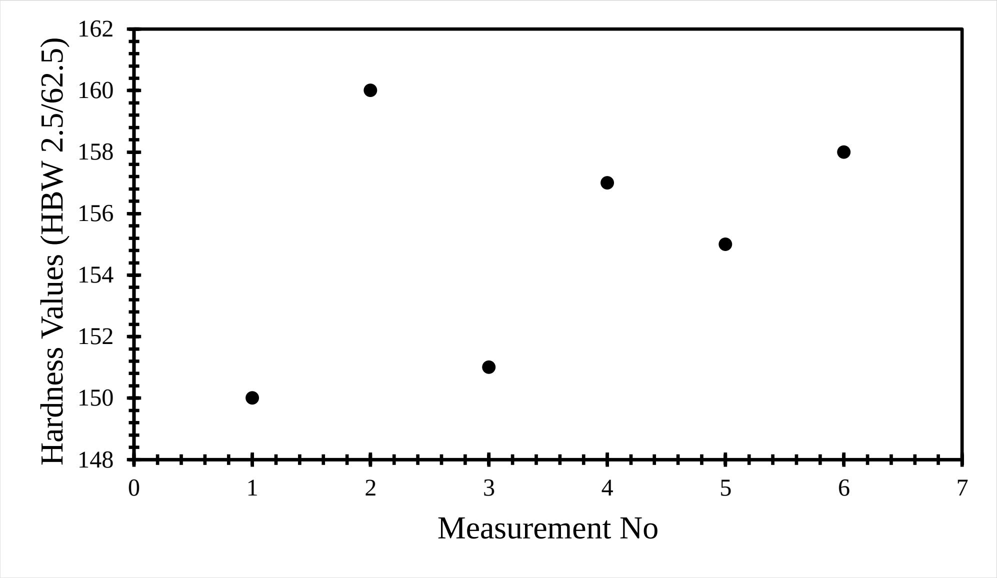

Figure 61. Hardness distribution of specimen 3 in the infiltration region.

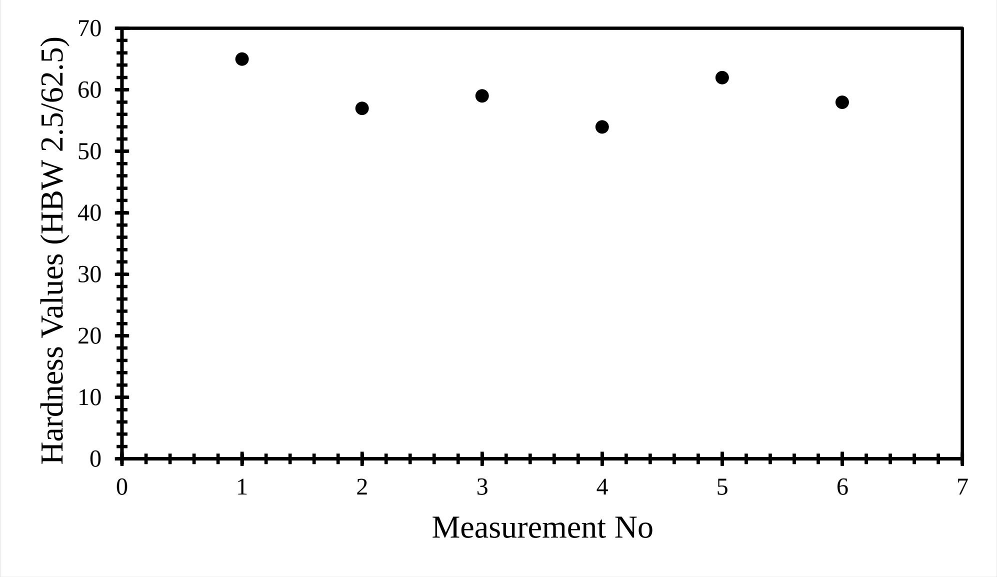

Figure 62. Hardness distribution of specimen 3 in the outer region.

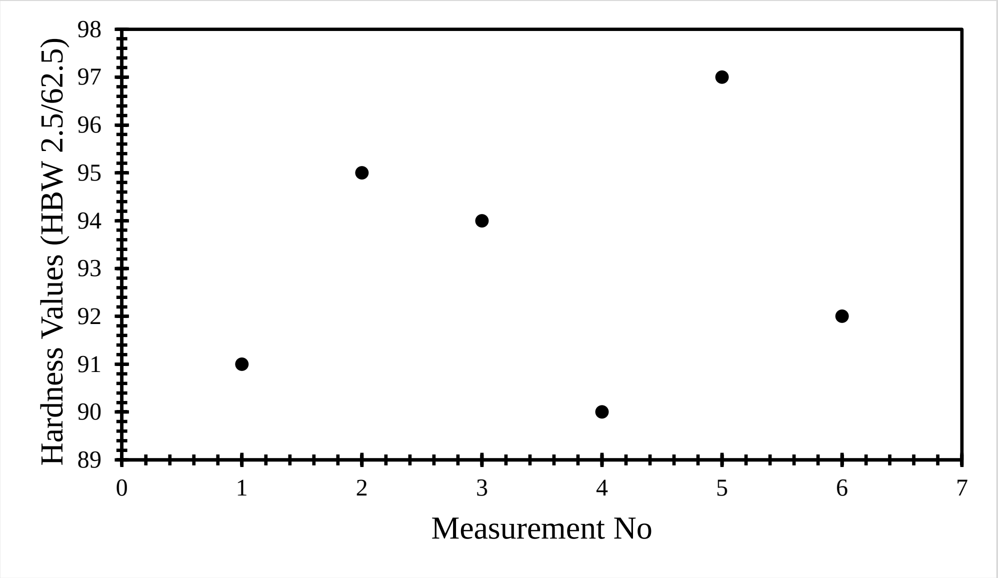

Figure 63. Hardness distribution of specimen 3 in the squeeze cast Al region.

Manu et al. [2] carried out a study where the direct squeeze infiltration of Al6061 alloy on SiC preform was successfully carried out with the controlled process parameters. All the porosities filled up with the Al6061. The volume fraction of the SiC in the preform was %50 and after the hot preform squeeze cast infiltration was applied to the green body, Brinell hardness tests were carried out on the final structure. The average hardness of the final specimen was found to be 147 BHN. When Manu et al. [2]'s hardness results are compared with the hardness results of specimens 1 and 2, and specimen 3's infiltration region, it can be seen that specimen 1 has much higher hardness (224.17) than the 147 BHN since vol% of SiC in the specimen 1 is averagely 67.36%. Specimen 2 has a very close average hardness value with Manu et al.'s [2] composite which is 145.33 and the vol% of SiC in specimen 2 was 51.95%. Both specimens have very close vol% of SiC, but there are differences between the production methodology, like the pure soft Al powder used in specimen 2, so it can be assumed as an expected outcome. Specimen 3 has a higher average hardness value which is an average of 155.17. Although the vol% the SiC in the composite was 43.68%, the after-sintering process was applied to the specimen and by doing that, the hardness of the Al matrix improved, so the Al matrix could support the SiC particles more efficiently during hardness tests, and the overall hardness increased in the final structure which leads to the higher hardness values of the specimen 3.

4.3.2 Wear Test Results

Specimens 1,2 and 3 were subjected to dry sliding wear tests according to the ASTM-G133. The tests were carried out under the normal loads of 10, 15, and 20 N, a sliding distance of 100 m, and a stroke distance of 5 mm. The effects of the volume fraction of the SiC and production method on the wear behavior of specimens 1,2 and 3 were investigated.

As it was shown in Figure 11 Figure 12, Mishra and Srivastava [39] reported that the volumetric wear rate of the SiC MMCs increases, and the coefficient of friction decreases with increasing the applied load from 10 to 30 N. Also, the study shows that increasing the SiC wt% improves the wear-resistant properties of the composite to a certain point.

Table 14 shows the numerical values of the specific wear rates of the specimens under the specific loads. Table 15 shows the numerical values of the wear volumes under the specific loads. Table 16 shows the mean friction coefficients of the specimens under the specific loads.

Table 14. Specific wear rate values of the specimens under different applied loads.

Applied Load (N)	**Specific Wear Ratex10^3 (mm^3/Nm)**		
	1	**2**	**3**
10	0.008	0.535	0.832
15	0.007	0.5	0.621
20	0.006	0.474	0.499

Table 15. Wear volumes of the specimens under different applied loads.

Applied Load (N)	**Wear volume (mm^3)**		
	1	**2**	**3**
10	0.008	0.535	0.832
15	0.01	0.75	0.932
20	0.012	0.948	0.998

Table 16. Mean friction coefficient values of the specimens under different applied loads.

Applied Load (N)	**Mean Friction Coefficient**		
	1	**2**	**3**
10	0.48	0.63	0.66
15	0.43	0.55	0.61
20	0.41	0.54	0.57

When specimen 1 is examined, the distribution of the specific wear rate, wear volume, and mean friction coefficient are shown in Figure 64Figure 67 Figure 68. Since it has the highest vol% of SiC, it has the highest wear strength as can be seen in Table 14Table 15. When specimens 2 and 3 are examined, the distribution of the specific wear rate, wear volume, and mean friction coefficient are shown in Figure 64Figure 66 Figure 68. Results indicate that specimen 2 has slightly higher wear resistance than specimen 3. The reason is that specimen 2 has a uniform structure, and it involves a higher vol% of SiC. Although there is pure Al powder inside the structure and the powder is not sintered contrary to specimen 3, specimen 3 was produced with cold preform squeeze casting and then sintering, and with this process, optimum infiltration could not be achieved and there are remaining porosities inside the structure. The Al matrix in specimen 3 has a higher average hardness than specimen 2 because of the sintering process applied to specimen 3, but it is not enough to tolerate the weakness coming from the porosities. The results indicate that as the applied load increases, the difference between the specific wear rate and wear volume of specimens 2 and 3 decreases. Polat et al. reported that the increase in the amount of porosity leads to the formation of recesses on the composite surfaces and this makes it more difficult for the surfaces to glide over each other as the load increases. Consequently, specimen 3 showed more wear resistance as the load increases and its performance nearly reached specimen 2.

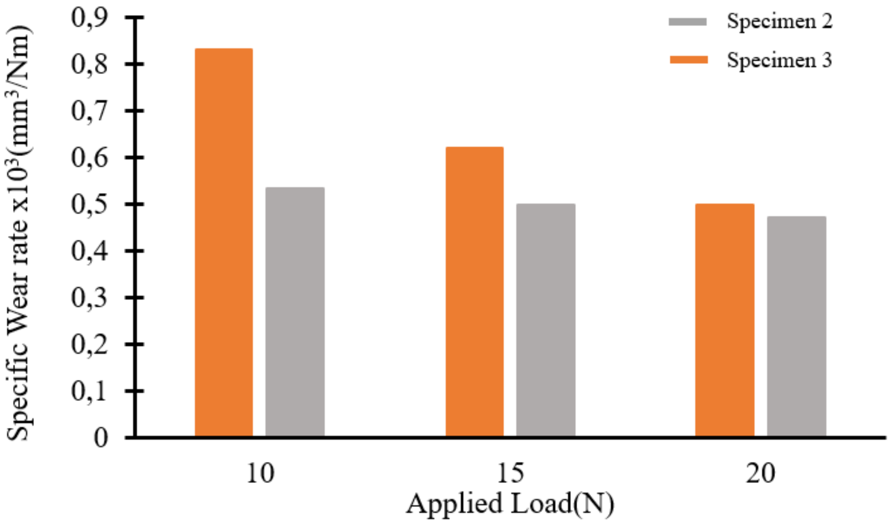

Figure 64. Specific wear rate values of specimens 2 and 3 under different applied loads.

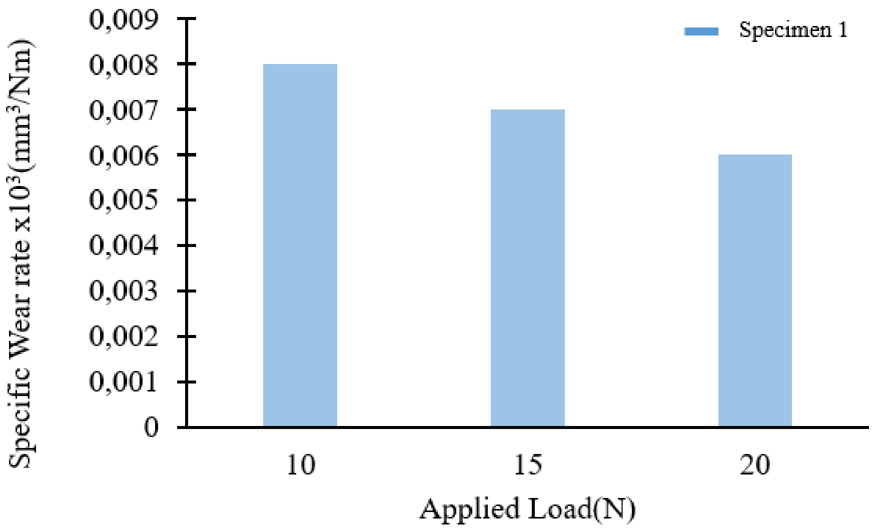

Figure 65. Specific wear rate values of specimen 1 under different applied loads.

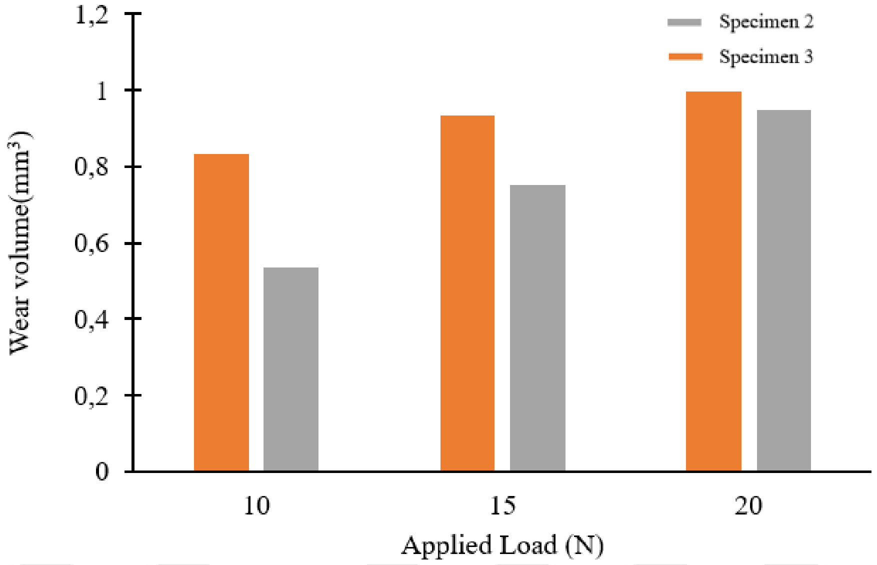

Figure 66. Wear volumes of specimens 2 and 3 under different applied loads.

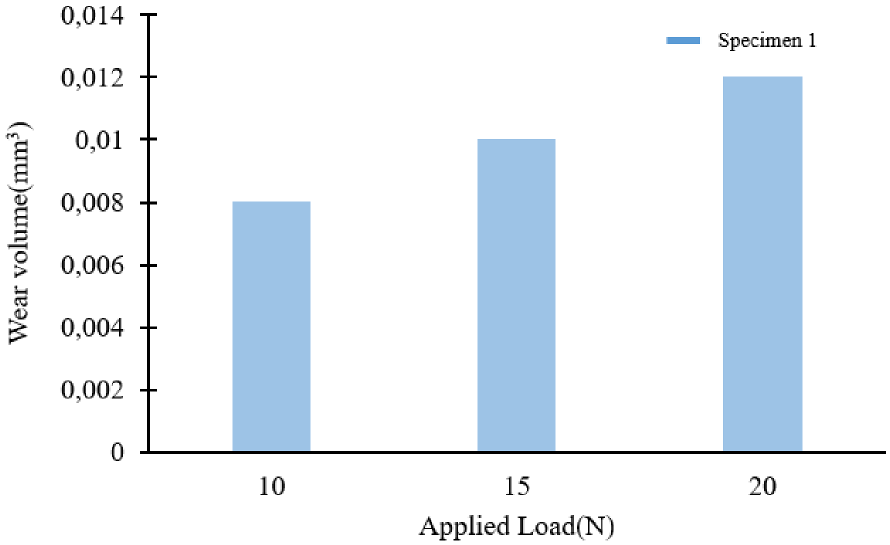

Figure 67. Wear volumes of specimen 1 under different applied loads.

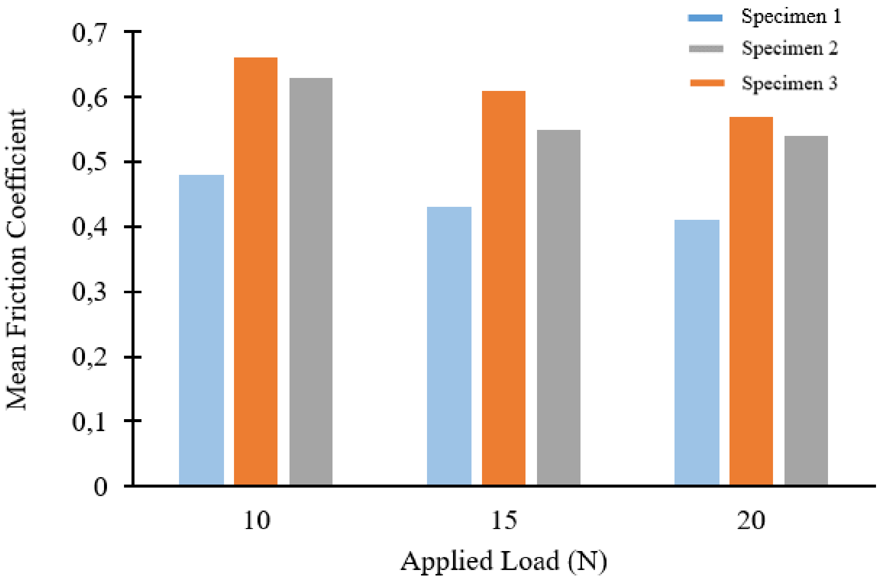

Figure 68. The mean friction coefficient of specimens 1,2 and 3 under different applied loads.

CHAPTER 5

CONCLUSIONS

Squeeze cast infiltrated specimens characterized by XRD, SEM, EDS, image analysis, particle size analysis, wear test, and hardness test. In terms of microstructural characterization, specimens 1 and 2 which were produced by hot preform squeeze casting showed a uniform structure with the homogenous distribution of SiC particles, and all the porosities were fulfilled with the infiltrated Al, so squeeze casting infiltration was successful. However, specimen 3 which was produced by cold preform squeeze casting did not achieve the uniform structure and there were remaining porosities inside the structure, so the squeeze casting infiltration could not be achieved properly due to the incomplete penetration of the liquid metal. In addition, Al_4C_3 was not observed in the specimens which is one the primary advantage of the squeeze casting due to the lower process temperature requirements. In terms of the mechanical characterization, experimental results revealed that the highest performance was obtained by the hot preform squeeze casting technique with 100% SiC porous compact. The average hardness value of specimen 1 was measured as 224 HBW (2.5/62.5). In addition, wear test results indicate that the specific wear rate of this specimen 1 gives the lowest specific wear rate which is 0.008, 0.007, and 0.006 mm^3/Nm under the 10, 15, and, 20 N applied loads.

Lastly, by increasing Mg content in the Al6061 about 2 wt%, more Mg2Si formation and Mg containing intermetallics are expected from JMatPro curves display a small arrest at 580 °C on the curve given at the Appendix.

Suggestions for future work:

As a feature work, TEM analysis and heat treatment procedures can be applied to the specimen and more experiments with different SiC contents can be tried with the hot and cold preform squeeze cast infiltration for full-density metal matrix composite production.

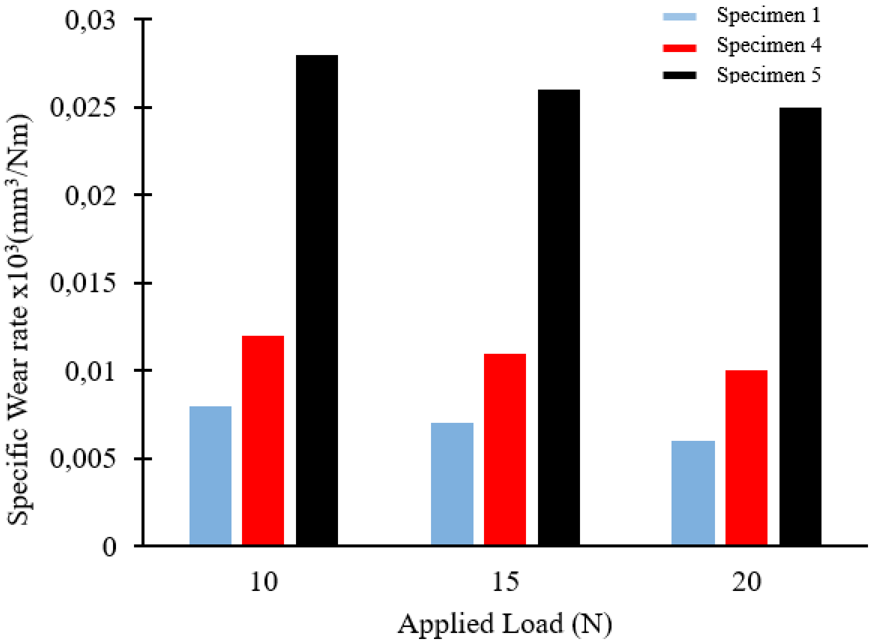

Figure 69. Specific wear rate values of the specimens under different applied loads. The green bodies were composed of 100 wt% SiC (specimens 1 and 4) and 50 wt% SiC (specimen 5).

The continuing research showed that when specimen 5 was subjected to the cold preform squeeze infiltration and vacuum sintering process, which is similar to specimen 3, it showed very close results with specimens 1 and 4. In the future, results can be examined in detail by using SEM, XRD, and EDS analysis.

REFERENCES

[1] G. Sala, “Technology-driven design of MMC squeeze cast connecting-rods,” *Sci Technol Adv Mater*, vol. 3, no. 1, pp. 45–57, Mar. 2002, doi: 10.1016/S1468-6996(01)00147-4.

[2] K. M. Sree Manu *et al.*, “Synthesis of Porous SiC Preform and Squeeze Infiltration Processing of Aluminium-SiC Metal Ceramic Composites,” *Materials Science Forum*, vol. 710, pp. 371–376, 2012, doi: 10.4028/WWW.SCIENTIFIC.NET/MSF.710.371.

[3] Q. Wang, Z. Chen, and Z. Chen, “Design and characteristics of hybrid composite armor subjected to projectile impact,” *Mater Des*, vol. 46, pp. 634–639, 2013, doi: 10.1016/J.MATDES.2012.10.052.

[4] J. López-Puente, A. Arias, R. Zaera, and C. Navarro, “The effect of the thickness of the adhesive layer on the ballistic limit of ceramic/metal armours. An experimental and numerical study,” *Int J Impact Eng*, vol. 32, no. 1–4, pp. 321–336, Dec. 2005, doi: 10.1016/J.IJIMPENG.2005.07.014.

[5] K. Krishnan, S. Sockalingam, S. Bansal, and S. D. Rajan, “Numerical simulation of ceramic composite armor subjected to ballistic impact,” *Compos B Eng*, vol. 41, no. 8, pp. 583–593, Dec. 2010, doi: 10.1016/J.COMPOSITESB.2010.10.001.

[6] A. H. Monazzah, R. Bagheri, S. S. Reihani, and H. Pouraliakbar, “Toughness enhancement in architecturally modified Al6061-5 vol.% SiCp laminated composites,” *http://dx.doi.org/10.1177/1056789514529984*, vol. 24, no. 2, pp. 245–262, Apr. 2014, doi: 10.1177/1056789514529984.

[7] A. Kalkanli, T. Durmaz, A. Kalemtas, and G. Arslan, “Melt Infiltration Casting of Alumina Silicon Carbide and Boron Carbide Reinforced Aluminum Matrix Composites,” *Journal of Material Science & Engineering*, vol. 06, no. 04, 2017, doi: 10.4172/2169-0022.1000357.

[8] S. M. S. Reihani, “Processing of squeeze cast Al6061–30vol% SiC composites and their characterization,” *Mater Des*, vol. 27, no. 3, pp. 216–222, Jan. 2006, doi: 10.1016/J.MATDES.2004.10.016.

[9] M. Nosonovsky and P. K. Rohatgi, “Biomimetics in materials science: Self-healing, self-lubricating, and self-cleaning materials,” *Springer Series in Materials Science*, vol. 152, no. 1, pp. 1–409, 2012, doi: 10.1007/978-1-4614-0926-7/COVER.

[10] P. K. Rohatgi, M. Tabandeh-Khorshid, E. Omrani, M. R. Lovell, and P. L. Menezes, “Tribology of metal matrix composites,” *Tribology for Scientists and Engineers: From Basics to Advanced Concepts*, vol. 9781461419457, pp. 233–268, Jul. 2013, doi: 10.1007/978-1-4614-1945-7_8.

[11] M. Kozma, “FRICTION AND WEAR OF ALUMINUM MATRIX COMPOSITES,” 2014. [Online]. Available: https://www.researchgate.net/publication/237833437

[12] R. Etemadi, B. Wang, K. M. Pillai, B. Niroumand, E. Omrani, and P. Rohatgi, “Pressure infiltration processes to synthesize metal matrix composites–A review of metal matrix composites, the technology and process simulation,” *Materials and Manufacturing Processes*, vol. 33, no. 12, pp. 1261–1290, Sep. 2018, doi: 10.1080/10426914.2017.1328122.

[13] S. C. Sharma, B. M. Girish, R. Kamath, and B. M. Satish, “Fractography, fluidity, and tensile properties of aluminum/hematite particulate composites,” *J Mater Eng Perform*, vol. 8, no. 3, pp. 309–314, Jun. 1999, doi: 10.1361/105994999770346855/METRICS.

[14] C. S. Lee, Y. H. Kim, K. S. Han, and T. Lim, “Wear behaviour of aluminium matrix composite materials,” *J Mater Sci*, vol. 27, no. 3, pp. 793–800, 1992, doi: 10.1007/BF02403898/METRICS.

[15] N. Natarajan, S. Vijayarangan, and I. Rajendran, “Wear behaviour of A356/25SiCp aluminium matrix composites sliding against automobile

friction material," *Wear*, vol. 261, no. 7–8, pp. 812–822, Oct. 2006, doi: 10.1016/J.WEAR.2006.01.011.

[16] A. B. Dresch, J. Venturini, S. Arcaro, O. R. K. Montedo, and C. P. Bergmann, "Ballistic ceramics and analysis of their mechanical properties for armour applications: A review," *Ceram Int*, vol. 47, no. 7, pp. 8743–8761, Apr. 2021, doi: 10.1016/J.CERAMINT.2020.12.095.

[17] T. Ma, H. Du, Z. Yan, Z. Li, and J. Zhang, "Mechanical Property and Ballistic Performance of Silicon Carbide," *Key Eng Mater*, vol. 434–435, pp. 72–75, 2010, doi: 10.4028/WWW.SCIENTIFIC.NET/KEM.434-435.72.

[18] A. Evans, C. San Marchi, and A. Mortensen, "Metal Matrix Composites in Industry," *Metal Matrix Composites in Industry*, 2003, doi: 10.1007/978-1-4615-0405-4.

[19] S. V. Prasad and R. Asthana, "Aluminum metal-matrix composites for automotive applications: Tribological considerations," *Tribol Lett*, vol. 17, no. 3, pp. 445–453, Oct. 2004, doi: 10.1023/B:TRIL.0000044492.91991.F3/METRICS.

[20] S. C. Tjong, S. Q. Wu, and H. C. Liao, "Wear behaviour of an Al–12% Si alloy reinforced with a low volume fraction of SiC particles," *Compos Sci Technol*, vol. 57, no. 12, pp. 1551–1558, Jan. 1998, doi: 10.1016/S0266-3538(97)00074-2.

[21] A. M. Zahedi, H. R. Rezaie, J. Javadpour, M. Mazaheri, and M. G. Haghighi, "Processing and impact behavior of Al/SiCp composites fabricated by the pressureless melt infiltration method," *Ceram Int*, vol. 35, no. 5, pp. 1919–1926, Jul. 2009, doi: 10.1016/J.CERAMINT.2008.10.024.

[22] İ. Bilici, M. GÜRÜ, and S. Tekeli, "Production of Ti-Fe Based MgAl2O4 Composite Material by Pressureless Infiltration Method," *Gazi University Journal of Science*, vol. 28, no. 2, pp. 295–299, Jun. 2015, Accessed: Jan.

12, 2024. [Online]. Available: https://dergipark.org.tr/en/pub/gujs/issue/7435/97834

[23] M. I. Pech-Canul and M. M. Makhlouf, “Processing of Al-SiCp metal matrix composites by pressureless infiltration of SiCp preforms,” *Journal of Materials Synthesis and Processing*, vol. 8, no. 1, pp. 35–53, Jan. 2000, doi: 10.1023/A:1009421727757/METRICS.

[24] M. I. Pech-Canul, R. N. Katz, and M. M. Makhlouf, “Optimum conditions for pressureless infiltration of SiCp preforms by aluminum alloys,” *J Mater Process Technol*, vol. 108, no. 1, pp. 68–77, Dec. 2000, doi: 10.1016/S0924-0136(00)00664-6.

[25] J. P. K, G. M. Shankar, A. Kini, and R. Shetty, “Review on Effect of Silicon Carbide (SiC) on Stir Cast Aluminium Metal Matrix Composites,” 2013. [Online]. Available: http://inpressco.com/category/ijcet

[26] J. Leng, G. Wu, Q. Zhou, Z. Dou, and X. L. Huang, “Mechanical properties of SiC/Gr/Al composites fabricated by squeeze casting technology,” *Scr Mater*, vol. 59, no. 6, pp. 619–622, Sep. 2008, doi: 10.1016/J.SCRIPTAMAT.2008.05.018.

[27] J. J. Sobczak, L. Drenchev, and R. Asthana, “Effect of pressure on solidification of metallic materials,” *International Journal of Cast Metals Research*, vol. 25, no. 1. pp. 1–14, Jan. 2012. doi: 10.1179/1743133611Y.0000000016.

[28] T. R. Vijayaram, S. Sulaiman, A. M. S. Hamouda, and M. H. M. Ahmad, “Fabrication of fiber reinforced metal matrix composites by squeeze casting technology,” *J Mater Process Technol*, vol. 178, no. 1–3, pp. 34–38, Sep. 2006, doi: 10.1016/J.JMATPROTEC.2005.09.026.

[29] M. Dhanashekar and V. S. Senthil Kumar, “Squeeze Casting of Aluminium Metal Matrix Composites-An Overview,” *Procedia Eng*, vol. 97, pp. 412–420, Jan. 2014, doi: 10.1016/J.PROENG.2014.12.265.

[30] G. Arslan and A. Kalemtas, “Processing of silicon carbide–boron carbide–aluminium composites,” *J Eur Ceram Soc*, vol. 29, no. 3, pp. 473–480, Feb. 2009, doi: 10.1016/J.JEURCERAMSOC.2008.06.007.

[31] L. J. Yang, “The effect of casting temperature on the properties of squeeze cast aluminium and zinc alloys,” *J Mater Process Technol*, vol. 140, no. 1–3, pp. 391–396, Sep. 2003, doi: 10.1016/S0924-0136(03)00763-5.

[32] P. Garg, A. Jamwal, D. Kumar, K. K. Sadasivuni, C. M. Hussain, and P. Gupta, “Advance research progresses in aluminium matrix composites: manufacturing & applications,” *Journal of Materials Research and Technology*, vol. 8, no. 5, pp. 4924–4939, Sep. 2019, doi: 10.1016/J.JMRT.2019.06.028.

[33] M. H. Sarfraz, M. Jahanzaib, W. Ahmed, and S. Hussain, “Multi-response parametric optimization of squeeze casting process for fabricating Al 6061-SiC composite,” *International Journal of Advanced Manufacturing Technology*, vol. 102, no. 1–4, pp. 759–773, May 2019, doi: 10.1007/S00170-018-03278-6/METRICS.

[34] H. S. Lee and S. H. Hong, “Pressure infiltration casting process and thermophysical properties of high volume fraction SiCp/Al metal matrix composites,” *Materials Science and Technology*, vol. 19, no. 8, pp. 1057–1064, Aug. 2003, doi: 10.1179/026708303225004396.

[35] Jianxin Liu, “Processes for sintering aluminum and aluminum alloy components,” US7517492, Apr. 14, 2009

[36] U. Avci and A. Güleç, “Effect of Different Sintering Temperatures on Microstructure and Mechanical Properties for Pure Al Material Produced by Powder Metallurgy,” *El-Cezeri*, vol. 8, no. 1, pp. 462–470, Jan. 2021, doi: 10.31202/ECJSE.789587.

[37] M. N. Mohammed, M. Z. Omar, M. S. Salleh, K. S. Alhawari, and P. Kapranos, “Semisolid metal processing techniques for nondendritic

feedstock production," *The Scientific World Journal*, vol. 2013, 2013, doi: 10.1155/2013/752175.

[38] P. K. Rohatgi, M. Tabandeh-Khorshid, E. Omrani, M. R. Lovell, and P. L. Menezes, "Tribology of metal matrix composites," *Tribology for Scientists and Engineers: From Basics to Advanced Concepts*, vol. 9781461419457, pp. 233–268, Jul. 2013, doi: 10.1007/978-1-4614-1945-7_8.

[39] A. K. Mishra and R. K. Srivastava, "Wear Behaviour of Al-6061/SiC Metal Matrix Composites," *Journal of The Institution of Engineers (India): Series C*, vol. 98, no. 2, pp. 97–103, Apr. 2017, doi: 10.1007/S40032-016-0284-3.

[40] M. Warmuzek, "Primary crystals of AlfeMnSi intermetallics in the cast AlSi alloys," *Archives of Metallurgy and Materials*, vol. 62, no. 3, pp. 1659–1664, Sep. 2017, doi: 10.1515/AMM-2017-0254.

[41] F. bo Meng, H. jun Huang, X. guang Yuan, X. jian Lin, Z. wen Cui, and X. lei Hu, "Segregation in squeeze casting 6061 aluminum alloy wheel spokes and its formation mechanism," *China Foundry*, vol. 18, no. 1, pp. 45–51, Jan. 2021, doi: 10.1007/S41230-021-0079-X.

[42] H. Mavros, A. E. Karantzalis, and A. Lekatou, "Solidification observations and sliding wear behavior of cast TiC particulate-reinforced AlMgSi matrix composites," *http://dx.doi.org/10.1177/0021998312454901*, vol. 47, no. 17, pp. 2149–2162, Aug. 2012, doi: 10.1177/0021998312454901.

[43] N. Nicom and H. Nomura, "Melt infiltration of SiCp reinforced Al matrix composite by newly designed pressure infiltration technique," *Materials Science and Engineering: A*, vol. 441, no. 1–2, pp. 97–105, Dec. 2006, doi: 10.1016/J.MSEA.2006.08.100.

[44] Fan Xi-gang, Jiang Da-ming, and MENG Qing-chang, "Evolution of eutectic structures in Al-Zn-Mg-Cu alloys during heat treatment," 2006. [Online]. Available: www.sciencedirect.com

A. Mg effect on solidification properties are given by JMatpro Analysis and curves

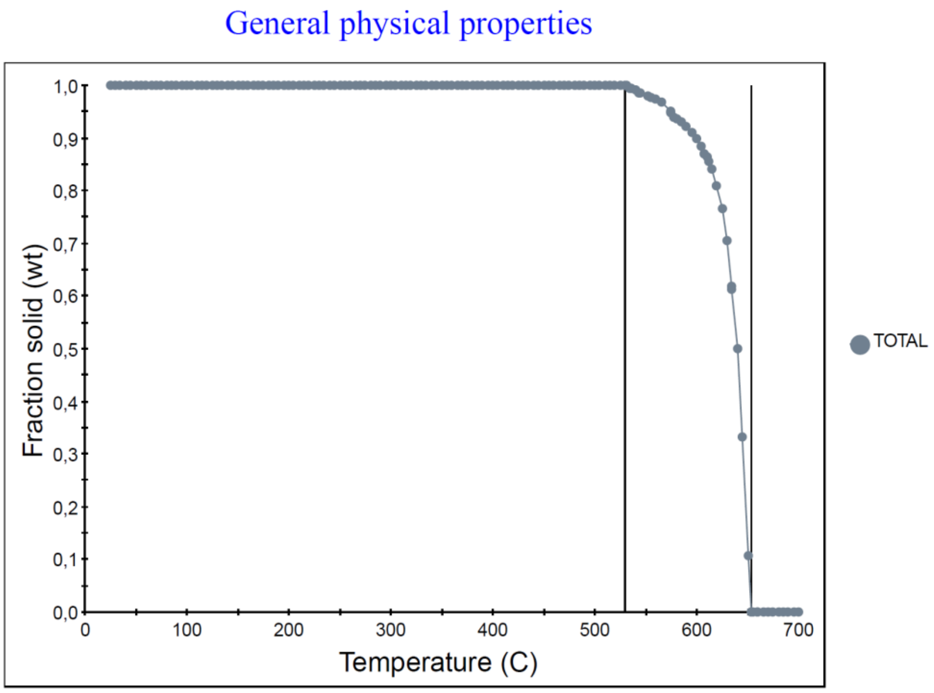

Figure 70 Fraction of solid wt% vs temperature curve for Al6061.

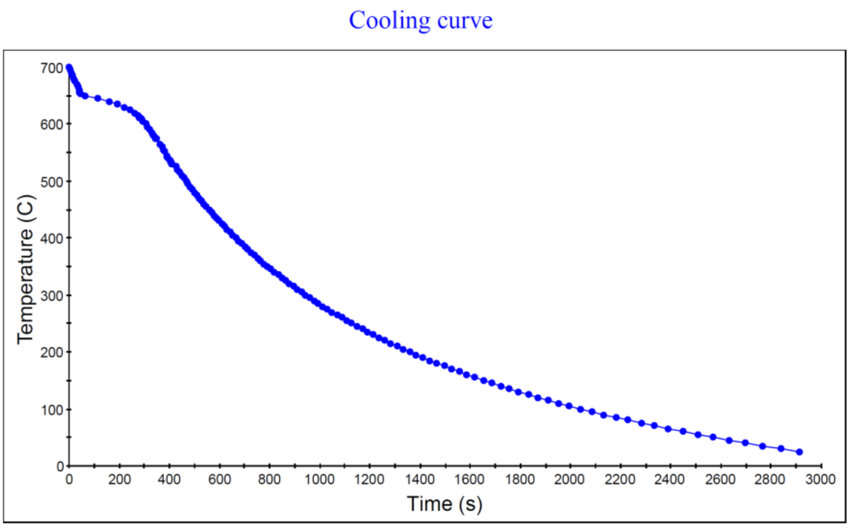

Figure 71 Cooling curve for Al6061.

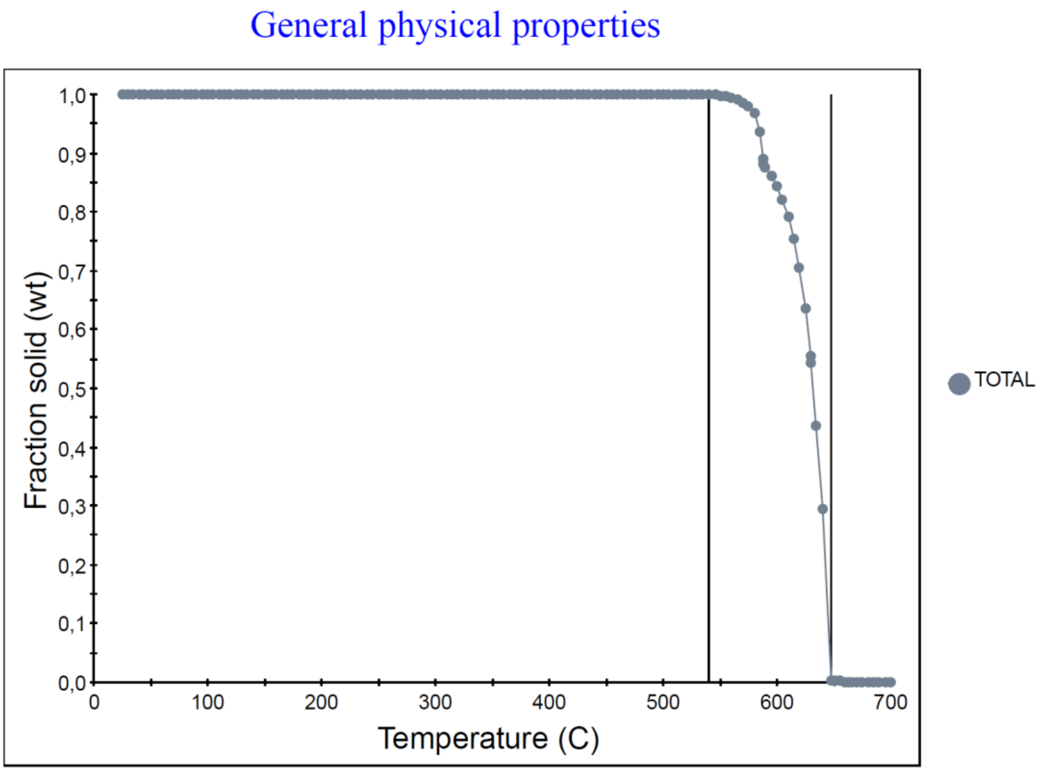

Figure 72 Fraction of solid wt% vs temperature curve for 2 wt% Mg added Al6061.

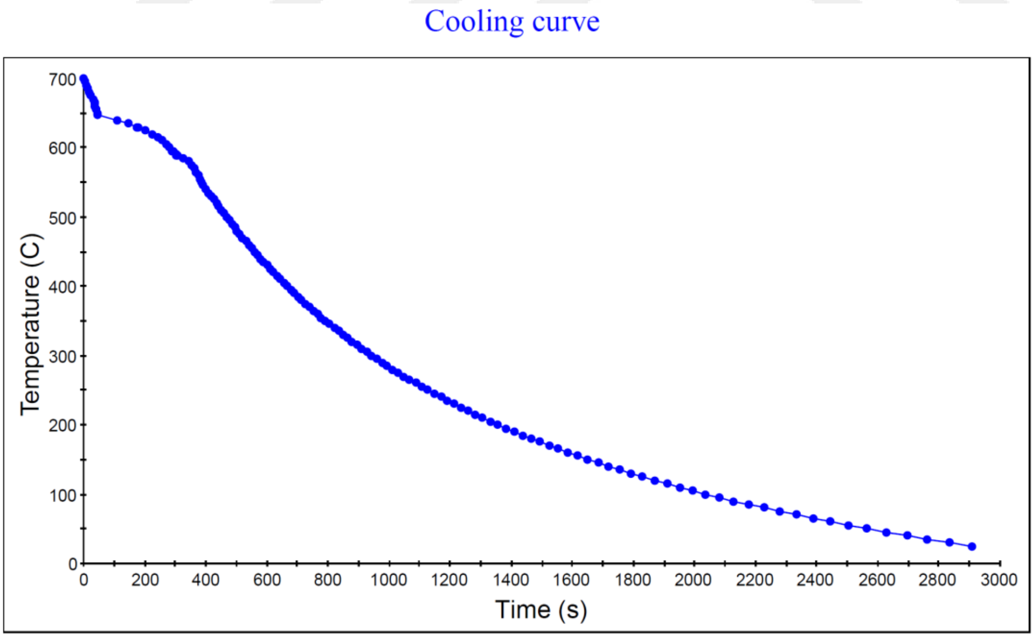

Figure 73 Cooling curve for 2 wt% Mg added Al6061.